UNCERTAINTY ANALYSIS AND VISUALIZATION OF DIFFUSION TENSOR IMAGES

by

Fangxiang Jiao

A dissertation submitted to the faculty of
The University of Utah
in partial fulfillment of the requirements for the degree of

Doctor of Philosophy

in

Physics

Department of Physics and Astronomy

The University of Utah

December 2012

The University of Utah Graduate School

STATEMENT OF DISSERTATION APPROVAL

The dissertation of **Fangxiang Jiao**

has been approved by the following supervisory committee members:

Benjamin Bromley	, Chair	**5/8/2012** Date Approved
Christopher R. Johnson	, Member	**5/8/2012** Date Approved
Xavier Tricoche	, Member	Date Approved
Yong-Shi Wu	, Member	**5/8/2012** Date Approved
Carleton DeTar	, Member	**5/14/2012** Date Approved

and by **David Kieda**, Chair of the Department of **Physics and Astronomy**

and by Charles A. Wight, Dean of The Graduate School.

ABSTRACT

Diffusion magnetic resonance imaging (dMRI) has become a popular technique to detect brain white matter structure. However, imaging noise, imaging artifacts, and modeling techniques, etc., create many uncertainties, which may generate misleading information for further analysis or applications, such as surgical planning. Therefore, how to analyze, effectively visualize, and reduce these uncertainties become very important research questions. In this dissertation, we present both rank-k decomposition and direct decomposition approaches based on spherical deconvolution to decompose the fiber directions more accurately for high angular resolution diffusion imaging (HARDI) data, which will reduce the uncertainties of the fiber directions. By applying volume rendering techniques to an ensemble of 3D orientation distribution function (ODF) glyphs, which we call *SIP functions* of *diffusion shapes*, one can elucidate the complex heteroscedastic structural variation in these local diffusion shapes. Furthermore, we quantify the extent of this variation by measuring the fraction of the volume of these shapes, which is consistent across all noise levels, the *certain volume ratio*. To better understand the uncertainties in white matter fiber tracks, we propose three metrics to quantify the differences between the results of diffusion tensor magnetic resonance imaging (DT-MRI) fiber tracking algorithms: the area between corresponding fibers of each bundle, the Earth Mover's Distance (EMD) between two fiber bundle volumes, and the current distance between two fiber bundle volumes. Based on these metrics, we discuss an interactive fiber track comparison visualization toolkit we have developed to visualize these uncertainties more efficiently. Physical phantoms, with high repeatability and reproducibility, are also designed with the hope of validating the dMRI techniques. In summary, this dissertation provides a better understanding about uncertainties in diffusion magnetic resonance imaging: where and how much are the uncertainties? How do we reduce these uncertainties? How can we possibly validate our algorithms?

CONTENTS

ACKNOWLEDGMENTS

I want to express my gratitude to my advisor, Chris Johnson, for his guidance, patience, and generous support. Without his inspiration and assistance, this thesis may not have been completed. I also want to thank him for making me a member of the Scientific Computing and Imaging (SCI) Institute, where insightful discussions and interesting talks helped me reshape my ideas, broaden my vision, and overcome numerous difficulties in my study. I would like to thank Ben Bromley for taking the effort to chair my Ph.D. committee and thank Xavier Tricoche, Yongshi Wu, and Carleton DeTar for serving as my committee members.

I want to thank my collaborator, Yaniv Gur. His mathematical expertise and his unique perspective contributed a lot to my research. I also want to thank him for reviewing this dissertation. I am very grateful to Jeff Phillips for his advice and assistance. I want to thank him for contributing valuable ideas to this work, and spending time with me during late-nights to catch up the conference deadlines.

My research was performed smoothly with the help of many people. Particularly, Edward Hsu provided valuable advice on my research and most of the data needed. I want to thank J. Davison de St. Germain for debugging my code whenever needed, especially during my early years in SCI. Also, I want to thank Tom Fogal, Jeroen Stinstra, and Ayla Khan for their help on software issues. Many thanks give to Tammy Kolda, Rob MacLeod, P. Thomas Fletcher, Sarang Joshi, Guido Gerig, Guoning Chen, Yongsheng Pan, Antonio Paiva, James Bigler, Yarden Livnat, and Jens Krger for their helpful discussions. And I am very thankful to my fellow students: Dafang Wang, Ran Tao, Jianrong Shu, Bo Wang, Xiang Hao, Wei Liu, Nikhil Singh, and Liang Zhou. Also, I want to thank my collaborators on the phantom fabrication project: Bruce Gale, Raheel Samuel, and Himanshu Sant.

Last, but not least, I want to thank my parents, Niansheng Jiao and Guilan Ma. They realized the importance of education, which completely changed my life. Finally, and most importantly, I want to thank my wife Ying and my son Dudu for their love and support.

CHAPTER 1

INTRODUCTION

1.1 Motivation

Diffusion magnetic resonance imaging (dMRI) is an important noninvasive technique for evaluating the three-dimensional white matter structure within the brain. By obtaining diffusion-weighted magnetic resonance images from multiple locations, a diffusion tensor can be reconstructed which is believed to delineate the local diffusion properties of water molecules in tissue [13]. David Tuch developed the method, high angular resolution diffusion imaging (HARDI) [149], which removes Gaussian assumption of the diffusion probability needed in the diffusion tensor model and models the local diffusion with an orientation distribution function (ODF). By applying HARDI technique, the well-known limitations of diffusion tensor in the areas of complex fiber heterogeneity (fiber crossing, fiber branching, and fiber kissing, etc.) can be resolved. Different fiber directions extraction algorithms [26, 2, 135] can be applied to HARDI models to figure out more accurate fiber directions. Finally, fiber tractography algorithms [15, 158, 98, 116, 33, 56] will be employed to form the three-dimensional connections of the brain.

However, dMRI techniques are affected by many sources of uncertainty, such as imaging noise, imaging artifacts, model fitting accuracy, fiber direction extraction accuracy, fiber tracking accuracy, uncertainties in fiber orientation(s), diffusion model fitting, and fiber track(s), which may produce heavily biased results for any further analysis. Thus, questions of how to accurately analyze and effectively visualize these uncertainties are important research questions with direct clinical applications in neurological diagnosis and treatment.

In this dissertation, I present two high-order tensor decomposition algorithms, a framework for three-dimensional uncertainty visualization and analysis of high-order tensors, a system for uncertainty quantification and visualization of neuro fiber tracks, and several possible designs of a MRI physical phantom.

1.2 Thesis Statement

Thesis goal 1 : Develop new methods to calculate dominant fiber direction(s) more accurately, which will reduce the uncertainties of the fiber direction(s) obtained from each voxel. Demonstrate the effectiveness of the new methods.

Explanation: The accuracy of existing algorithms to find the dominant fiber direction(s) are limited by the orientation distribution function (ODF) reconstruction quality, its reconstruction order (i.e., the spherical harmonics truncation order), and decompositions methods. Different modalities and estimation techniques associated with HARDI have been proposed over the years. Issues like how to guarantee the estimated higher order tensor (HOT) or orientation distribution function (ODF) are symmetric positive definite, how to decompose the HOT/ODF in a more rigorous way rather than using ad hoc approaches, and how to reduce the number of diffusion weighted images needed for HARDI, need to be studied.

Validation: Completion of the proposed goal will result in 1) a written comparison of several existing methods in higher order tensor estimation and decomposition, demonstrating the problems with these methods and how to improve them, and 2) a new algorithm that will estimate HOT/ODF more rigorously, with symmetric positive definite constraints, may reduce the number of diffusion weighted images needed but obtain similar or better levels of accuracy.

Thesis goal 2: Develop new methods to visualize the uncertainties of the higher order tensor field.

Explanation: Uncertainty visualization is crucial for answering the location and the degree of uncertainty. Three-dimensional uncertainty visualization of the higher-order tensor field is a very challenging problem, due to the complexity of the HOT shapes. Existing approaches can only show variations on mean shapes, or only show mean shape plus and minus one standard deviation of the shape distribution. More details about the uncertainty are not visible.

Validation: Completion of the proposed goal will result in 1) a new uncertainty visualization method to visualize the uncertainties of a collection of higher order tensors, and 2) a tool may be extended to any DTI or other HARDI models to study the uncertainties of the data, algorithm, etc.

Thesis goal 3: Develop new methods to quantify the fiber track differences and to interactively visualize these differences.

Explanation: Existing methods of fiber similarity quantification are based on Euclidean distances between predefined correspondences. The predefined correspondences may not

be easy to define, and miscorrespondences will completely disrupt the similarity measure. Also, existing methods cannot interactively visualize fiber track differences, which makes the study of brain fiber structure extremely difficult for non-DTI experts.

Validation: Completion of the proposed goals will result in 1) a new definition of fiber correspondence or a new robust measure to quantify the fiber similarity, and 2) a toolkit that can be easily used by any researcher to study the brain white matter structure.

Thesis goal 4: Fabricate a white matter phantom that can be used to validate the fiber tracking algorithms. The phantoms should be easy to reproduce.

Explanation: So far, there does not exist a physical "gold standard" by which to compare algorithms. Phantom fabrication is one possible way to achieve this goal. Existing techniques use silk, hemp, linen, or rayon to generate a phantom, which is not easily reproducible.

Validation: Completion of the proposed goal will result in 1) a new physical phantom for validation of fiber tracking algorithms.

1.3 Thesis Organization

The dissertation is organized in the following way:

Chapter 2 introduces the basic principles of magnetic resonance imaging (MRI). It covers magnetization, RF excitations, relaxation, signal localization and signal detection. The derivation of Stejskal-Tanner equation is also presented.

Chapter 3 reviews the basics of diffusion magnetic resonance imaging (dMRI). It provides the background knowledge about diffusion tensor imaging (DTI), high angular resolution diffusion imaging (HARDI), and fiber tractography.

Chapter 4 discusses a novel framework that combines an ODF estimation method with a parameter extraction technique for estimation of fiber directions and fiber fractions. For the estimation method, we have used a specific form of spherical deconvolution [143] where the ODF is represented by a homogeneous polynomial induced by a high-order tensor. The ODF was constrained to be non-negative by adding a set of linear constraints to the objective function that represents the spherical deconvolution. Then, a Candecomp/Parafac (CP) decomposition is applied to the ODF and decomposes it into a sum of rank-1 tensors which represent single white matter fibers. These rank-1 tensors provide information on the fiber orientations and the volume fractions.

Chapter 5 shows a technique to extract white matter fiber orientations and weights directly from diffusion-weighted imaging (DWI) measurements. It is based on a spherical deconvolution technique and decomposition of a homogeneous polynomial into a sum of

powers of linear forms, known as a *symmetric tensor decomposition*. The fiber-ODF (fODF), described by a homogeneous polynomial, is approximated here as a discrete sum of even-order linear-forms representing single-fibers. This polynomial expansion is convolved to a single-fiber response function, and the result is optimized against the DWI measurements to assess the fiber parameters. This formulation leads to a nonlinear optimization problem that we solve here by means of the Levenberg-Marquart technique.

Chapter 6 presents a new and accurate technique for uncertainty analysis and uncertainty visualization based on fiber orientation distribution function (ODF) glyphs, associated with high angular resolution diffusion imaging (HARDI). Our visualization applies volume rendering techniques to an ensemble of 3D ODF glyphs which we call *SIP functions* of *diffusion shapes*, to capture their variability due to underlying uncertainty. This rendering elucidates the complex heteroscedastic structural variation in these shapes. Furthermore, we quantify the extent of this variation by measuring the fraction of the volume of these shapes, which is consistent across all noise levels, the *certain volume ratio*.

Chapter 7 proposes three metrics to quantify the differences between the results of diffusion tensor magnetic resonance imaging (DT-MRI) fiber tracking algorithms: the area between corresponding fibers of each bundle, the Earth Mover's Distance (EMD) between two fiber bundle volumes, and the current distance between two fiber bundle volumes. We also discussed an interactive fiber track comparison visualization toolkit we have developed based on the three proposed fiber difference metrics and have tested on six widely-used fiber tracking algorithms.

Chapter 8 reports the initial results of fabrication of a DT-MRI phantom created by stacking of multiple thin polydimethylsiloxane (PDMS) layers.

1.4 Contributions

The major contributions of this dissertation are:

- A novel framework that combines an ODF estimation method with a parameter extraction technique for estimation of fiber directions and fiber fractions (Chapter 4).
- A new technique to extract white matter fiber orientations and weights directly from diffusion-weighted imaging (DWI) measurements (Chapter 5).
- A new and accurate technique for uncertainty analysis and three-dimensional uncertainty visualization based on fiber orientation distribution function (ODF) glyphs (Chapter 6).

- Three metrics to quantify the differences between the results of fiber tractography, and an interactive fiber track comparison visualization toolkit have been developed based on the three proposed fiber difference metrics (Chapter 7).
- A novel approach in HARDI fabrication of a DT-MRI phantom (Chapter 8).

CHAPTER 2

INTRODUCTION TO MAGNETIC RESONANCE IMAGING

Magnetic Resonance Imaging (MRI) is based on the nuclear magnetic resonance (NMR) phenomenon observed in bulk matter independently by Felix Bloch and Edward Purcell in 1946. Spacial information encoding principles, developed by Paul Lauterbur in 1972, make the image formation possible. Later, diffusion magnetic resonance imaging (dMRI) and functional magnetic resonance imaging (fMRI) were introduced in the 90s. Table 2.1 shows the major developments in the field of MRI/NMR.

Because of spacial information encoding, MRI can generate two-dimensional sectional images at any orientation, three-dimensional volumetric images, which represent the spatial distribution of some measured physical quantity. It operates in the radio-frequency(RF) range, as shown in Figure 2.1. Therefore, the imaging process does not involve the use of ionizing radiation and does not have the associated potential harmful effects.

Table 2.1: Milestones of MRI

Time	Event
1946	MR phenomenon-Bloch and Purcell
1952	Nobel Prize-Bloch and Purcell
1973	Backprojection MRI-Lauterbur
1975	Fourier Imaging
1977	Echo-planar imaging (EPI)-Mansfield
1980	FT MRI demonstrated-Edelstein
1986	Gradient Echo Imaging
1986	NMR Microscope
1987	MR Angiography-Dumoulin
1991	Nobel Prize-Ernst
1992	Functional MRI
1994	Diffusion Tensor Imaging-Basser
1994	Hyperpolarized ^{129}Xe Imaging
2003	Nobel Prize-Lauterbur and Mansfield

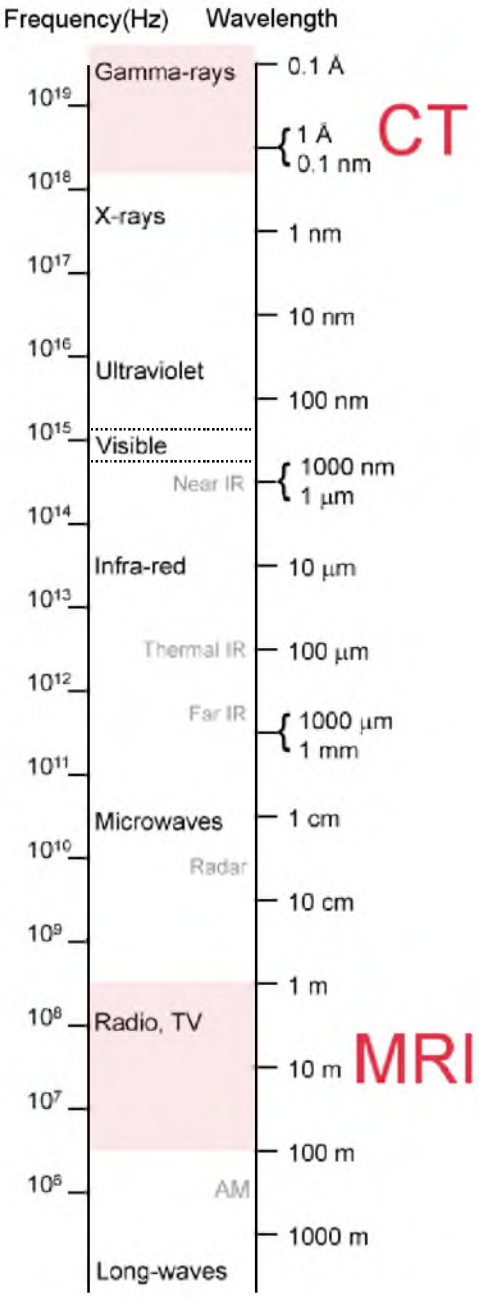

Figure 2.1: Electromagnetic spectrum. Image adapted from http://kingfish.coastal.edu

The most important aspect of MRI is that the images are extremely rich in information content. The image voxel values are dependent on several intrinsic parameters, including the nuclear spin density ρ, the spin-lattice relaxation time T_1, the spin-spin relaxation time T_2, molecular motions (i.e., diffusion or perfusion), susceptibility effects, and chemical shift effects. Moreover, the imaging effects of these parameters can be suppressed or enhanced in a specific experiment by another set of operator-selectable parameters, such as repetition time (T_R), echo time (T_E), and flip angle (α). Therefore, an MRI image obtained from the same subject can look drastically different with different data acquisition protocols. In this chapter, we will explain how MRI works.

2.1 MRI Scanner Hardware

As shown in Figure 2.2, a typical MRI scanner system contains three main hardware components: a main magnet, a magnetic field gradient system, and an RF system. Generally, the main magnet is a superconducting magnet, which will generate a strong static magnetic field, i.e., the B_0 field. For clinical applications, the common strength of the B_0 magnetic field is $1.5T$, $3T$, or $4T$. High fields have better signal-to-noise ratio and spectral resolution, but may cause RF penetration problems and more imaging artifacts. Gradient coils are responsible for generating time-varying magnetic fields for signal spatial localization, which is the key component of MRI. The RF system consists of a transmitter coil that is capable of generating a rotating magnetic field, i.e., the B_1 field, for excitation of a spin system, and a receiver coil that converts a processing magnetization into electrical signal. Sometimes, a single coil can be used as both a transmitter and receiver coils, thus the name transceiver coil. The bottom image of Figure 2.2 shows a detailed structure of the X, Y, Z gradient coil and transceiver.

2.2 Magnetization

It is the procession of the proton that generates the MRI/NMR signal. We will explain how in this chapter. One thing that needs to be clear is that, for protons, precession is the change in the orientation of the spinning axis of the proton, not proton intrinsic spin itself. The intrinsic proton spin can be thought of as leading to a circulating electric current, hence, an associated magnetic moment. The relationship between the magnetic moment and the spin angular momentum vector is:

$$\vec{\mu} = \gamma \vec{J} \tag{2.1}$$

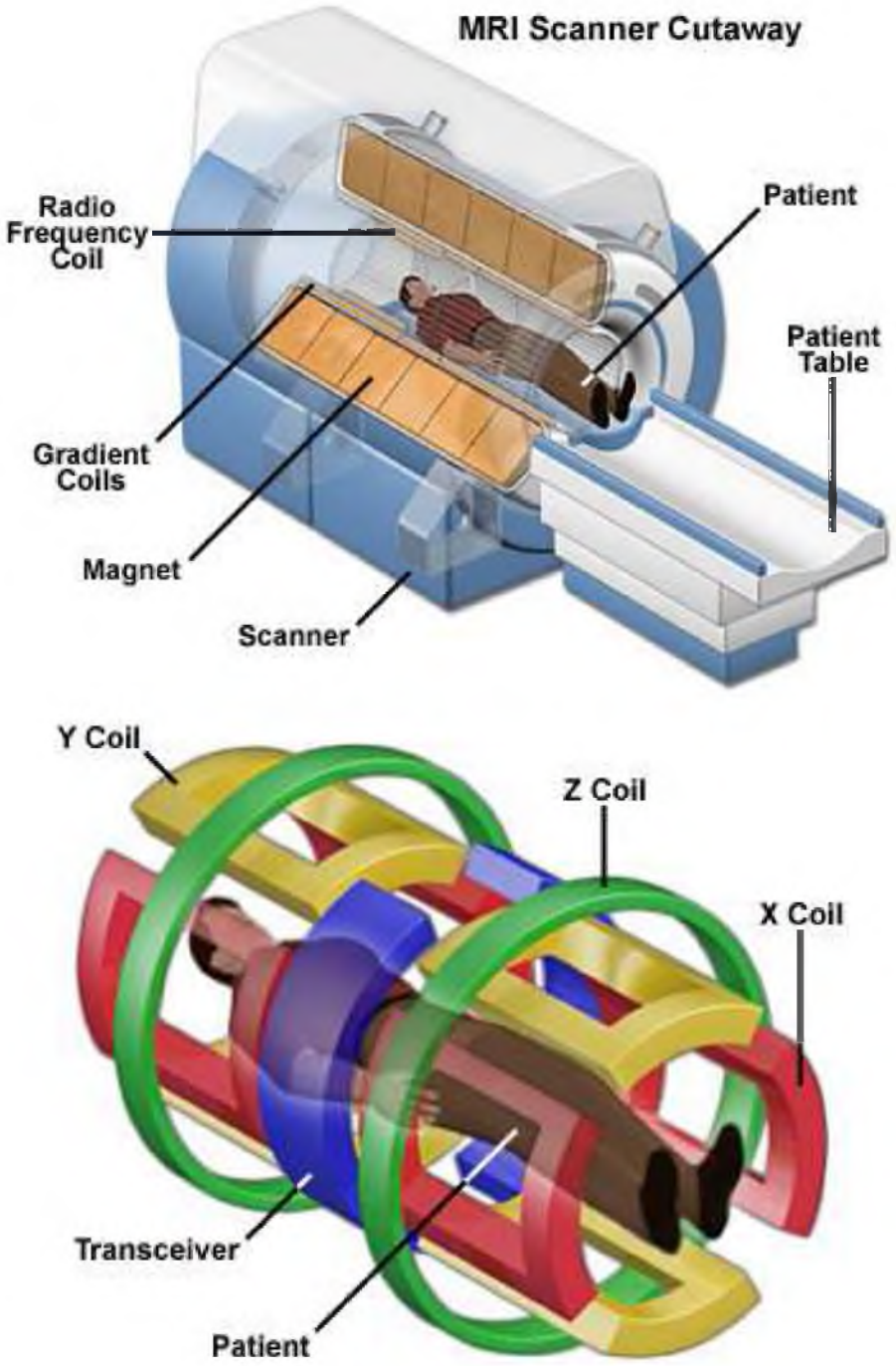

Figure 2.2: A typical clinical MRI scanner, and Gradient coils and Transceiver. Images adapted from http://www.magnet.fsu.edu/education/tutorials/magnetacademy/mri/.

The constant, γ, is called the gyromagnetic ratio and depends on the particle or nucleus. Table 2.2 shows the natural abundance, spin number, gyromagnetic ratio, and the abundance in the body of all of the nuclei that can generate MRI signal. Particularly, the gyromagnetic ratio for water is

$$\gamma = 2.675 \times 10^8 rad/s/T \tag{2.2}$$

or, 'gamma-bar' as,

$$\bar{\gamma} = \frac{\gamma}{2\pi} = 42.58 MHz/T \tag{2.3}$$

where T is the Tesla unit of the magnetic field and is equal to 10000 Gauss (G). The frequency at which the nucleus precesses about the static magnetic field B_0 is known as the Larmor frequency, ω_L

$$\omega_L = \gamma B_0 \tag{2.4}$$

To describe the collective behavior of a spin system, a macroscopic magnetization vector $\vec{M}$ is introduced, which is the sum of all the microscopic magnetic moments per unit volume.

$$\vec{M} = \frac{1}{V} \sum_V \vec{\mu_i} \tag{2.5}$$

The transverse components of magnetization M is perpendicular to static magnetic field B0 and precesses at the Larmor frequency. This produces an oscillating magnetic field that can be detected with an RF receiver coil. At equilibrium, nuclei precess with random phases, which cause the transverse components of magnetic moments to cancel out. On the other hand, a small net magnetization along the longitudinal direction does exist. However, since it is parallel with the longitudinal direction of the receiver coil, no induced signal will be generated.

Table 2.2: List of nuclei found in the human body with natural abundance

Nucleus	Symbol	Natural Abundance (%)	Spin ($\hbar$)	Gyromagnetic ratio $\bar{\gamma}$ (MHz/T)	Abundance in body (%)
Hydrogen	^1H	99.985	1/2	42.58	63
Hydrogen	^2H	0.015	1	6.54	63
Phosphorus	^{31}P	100	1/2	17.25	0.24
Sodium	^{23}Na	100	3/2	11.27	0.041
Nitrogen	^{14}N	99.63	1	3.08	1.5
Carbon	^{13}C	1.11	1/2	10.71	9.4
Fluorine	^{19}F	100	1/2	40.08	0
Oxygen	^{17}O	0.037	5/2	-5.77	26

However, when an external magnetic field, i.e., B_0 field, is applied, the nuclei spins will be aligned with the B_0 field. Spins in different orientation have different energy of interaction with the external magnetic field. According to quantum theory,

$$E = -\vec{\mu} \cdot \vec{B_0} = -\mu_z B_0 = -\gamma \hbar m_I B_0 \tag{2.6}$$

where $\hbar$ is called the Plank constant, and $m_I = \pm\frac{1}{2}$. For pointing-up spin ($m_I = \frac{1}{2}$),

$$E_\uparrow = -\frac{1}{2}\gamma \hbar B_0 \tag{2.7}$$

For pointing-down spin ($m_I = -\frac{1}{2}$),

$$E_\downarrow = \frac{1}{2}\gamma \hbar B_0 \tag{2.8}$$

which means spin-up state is the lower energy state, and spin down is the higher energy state. The energy difference between two spin states is,

$$\Delta E = E_\downarrow - E_\uparrow = \gamma \hbar B_0 = \gamma \omega_0 \tag{2.9}$$

This is the so called *Zeeman splitting* phenomenon, as illustrated in Figure 2.3. The spin population difference in the two energy states obeys the Boltzmann distribution,

$$\frac{N_\uparrow}{N_\downarrow} = \exp(\frac{\Delta E}{K T_s}) \tag{2.10}$$

where $N_\uparrow$ is the number of pointing-up spins, $N_\downarrow$ is the number of pointing-down spins, T_s is the absolute temperature of the spin system, and K is the Boltzmann constant. In practice,

$$\Delta E \ll K T_s \tag{2.11}$$

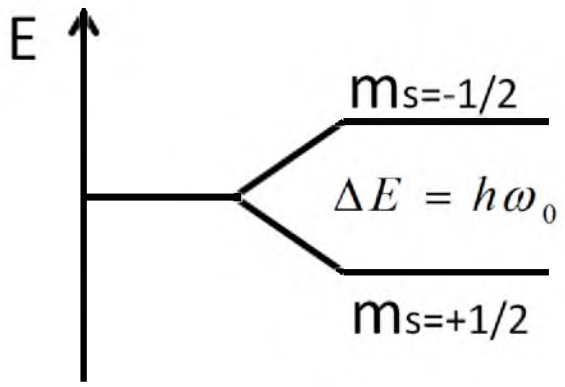

Figure 2.3: Zeeman splitting for a spin-$\frac{1}{2}$ system

By first-order approximation,

$$\frac{N_{\uparrow}}{N_{\downarrow}} \approx 1 + \frac{\gamma \hbar B_0}{KT_s} \tag{2.12}$$

Equation 2.12 shows that there is an excess of a very small fraction $\frac{\gamma \hbar B_0}{KT_s}$ of spins in the lower energy state. This uneven spin distribution between the two spin states occurs because a lower energy state level is preferred. It is exactly this small spin population distribution difference that generates the observable macroscopic magnetization. After the RF excitations, this oscillating macroscopic magnetization can generate measurable MR signal.

2.3 RF Excitations

RF pulse is a synonym of the B_1 field, which is short-lived and oscillates in the radio-frequency range in the transverse plane. It is generally turned on for a few microseconds or milliseconds, and the magnitude ($\sim$ 50mT) is small compared with the static magnetic field B_0. A typical B_1 takes the following form:

$$\vec{B_1}(t) = 2B_1^e(t)\cos(\omega_{rf}t + \varphi)\vec{i} \tag{2.13}$$

where $B_1^e(t)$ is the pulse envelope function, ω_{rf} is the excitation carrier frequency, and φ is the initial phase angle. It is linear polarized and can be decomposed into two circularly polarized fields rotating in opposite directions,

$$\begin{aligned} \vec{B_1}(t) = {} & B_1^e(t)\left[\cos(\omega_{rf}t + \varphi)\vec{i} - \sin(\omega_{rf}t + \varphi)\vec{j}\right] \\ & + B_1^e(t)\left[\cos(\omega_{rf}t + \varphi)\vec{i} + \sin(\omega_{rf}t + \varphi)\vec{j}\right] \end{aligned} \tag{2.14}$$

where the first term rotates clockwise and the second term rotates counterclockwise. Since the counterclockwise term rotates in the opposite direction of the precessing spins, it exerts negligible effects on a spin system if ω_{rf} is near the Larmor frequency. Therefore, only the first term is effective and causes the resonance on the precessing spins. From quantum mechanics, the electromagnetic radiation of frequency ω_{rf} carry energy:

$$E_{rf} = \hbar\omega_{rf} \tag{2.15}$$

If E_{rf} is equal to the energy difference between the adjacent spin states, a coherent transition of spins from one energy state to another will be induced. That is,

$$\hbar\omega_{rf} = \Delta E = \gamma \hbar B_0 \tag{2.16}$$

or

$$\omega_{rf} = \omega_0 \tag{2.17}$$

this is the resonance condition. By applying a transverse oscillating magnetic field at exactly this resonance frequency, the nuclear magnetization can be tipped away from the longitudinal axis, which generates components in the transverse plane. The detectable MR signal can be produced.

2.4 Relaxation

The MRI signal decays the subject to T_1 and T_2 relaxation decay mechanism. T_1 relaxation is also called longitudinal relaxation time, which represents the spin-environment interaction. T_2 relaxation is called transverse relaxation time, which represents the spin-spin interaction. Both T_1 and T_2 are physical properties related with the tissue type, and T_2 is generally shorter than T_1. Table 2.3 shows the approximate T_1 and T_2 for human soft tissues under 1.5 Tesla.

2.4.1 T_1 Relaxation

T_1 is a measure of the time required for a substance in an applied magnetic field to remain longitudinally magnetized following an RF pulse. It is the time constant to release the energy absorbed due to the RF pulse into the environment. The process can be described by the following equation,

$$\frac{dM_z}{dt} = \frac{-(M_z - M_0)}{T_1} \tag{2.18}$$

with the solution

$$M_z(t) = M_z(0)\exp(-t/T_1) + M_0\left(1 - \exp(-t/T_1)\right) \tag{2.19}$$

The process involves an exchange of energy between the spin system and the surrounding thermal reservoir, also known as the 'lattice', with which it is in equilibrium. The equilib-

Table 2.3: T_1 and T_2 relaxation time of different tissues

Tissue Type	Approximate T_1(ms)	Approximate T_2(ms)
Adipose tissues	240 ∽ 250	60 ∽ 80
Whole blood (deoxygenated)	1350	50
Whole blood (oxygenated)	1350	200
Cerebrospinal fluid	4200 ∽ 4500	2100 ∽ 2300
Gray matter of cerebrum	920	100
White matter of cerebrum	780	90
Liver	490	40
Kidneys	650	60 ∽ 75
Muscles	860 ∽ 900	50

rium is characterized by a state of polarization with magnetization M_0 directed along the longitudinal magnetic field B_0.

2.4.2 T_2 Relaxation

The T_2 relaxation can be described as,

$$\frac{dM_{x,y}}{dt} = \frac{-M_{x,y}}{T_2} \tag{2.20}$$

with solution

$$M_{x,y}(t) = M_{x,y}(0)\exp(-t/T_2) \tag{2.21}$$

This is the regime of the Bloembergen, Purcell, and Pound (BPP) theory [25], and the detailed explanation will be given in Section 2.4.4. It works very well for spins residing in liquid state molecules.

One intuitive but incorrect idea is that: The longitudinal component and transverse component of magnetization M_0 are orthogonal. If one returns to its maximum, the other one should return to 0 position. Therefore, both T_1 and T_2 should be the same. In fact, transverse relaxation T_2 is the process whereby nuclear spins come to thermal equilibrium among themselves. While indirect energy exchange via the lattice may play a role, additional direct processes were also involved. This led to $T_2 \leq T_1$.

2.4.3 Bloch Equation

By equating the torque to the rate of change of angular momentum, we obtain

$$\frac{d\mathbf{M}}{dt} = \gamma\mathbf{M} \times \mathbf{B} \tag{2.22}$$

Combining Equation 2.22, 2.18, and 2.20 in the rotating frame yields Bloch equations.

$$\begin{aligned}
\frac{dM_x}{dt} &= \gamma M_y(B_0 - \omega/\gamma) - \frac{M_x}{T_2} \\
\frac{dM_y}{dt} &= \gamma M_z B_1 - \gamma M_x(B_0 - \omega/\gamma) - \frac{M_y}{T_2} \\
\frac{dM_z}{dt} &= -\gamma M_y B_1 - \frac{(M_z - M_0)}{T_1}
\end{aligned} \tag{2.23}$$

These are the most fundamental equations to explain many phenomena important in MRI.

2.4.4 Quantum Description of Relaxation

For two closely spaced Dipoles with moments μ_1 and μ_2, the total energy is

$$E = \frac{\vec{\mu_1} \cdot \vec{\mu_2}}{r^3} - \frac{3(\vec{\mu_1} \cdot \vec{r})(\vec{\mu_2} \cdot \vec{r})}{r^5} \tag{2.24}$$

where

$$\vec{\mu_1} = \gamma_1 \hbar \vec{I_1} \tag{2.25}$$

$$\vec{\mu_2} = \gamma_2 \hbar \vec{I_2} \tag{2.26}$$

The Hamiltonian of this system can be rewritten as

$$H = \frac{\gamma_1 \gamma_2 \hbar^2}{r^3}(A + B + C + D + E + F) \tag{2.27}$$

where

$$\begin{aligned} A &= I_{1z} I_{2z}(1 - 3\cos^2\theta) \\ B &= -1/4(I_1^+ I_2^- + I_1^- I_2^+)(1 - 3\cos^2\theta) \\ C &= -3/2(I_1^+ I_{2z} + I_{1z} I_2^+)\sin\theta\cos\theta e^{-i\phi} \\ D &= -3/2(I_1^- I_{2z} + I_{1z} I_2^-)\sin\theta\cos\theta e^{i\phi} \\ E &= -3/4 I_1^+ I_2^+ \sin^2\theta e^{-2i\phi} \\ F &= -3/4 I_1^- I_2^- \sin^2\theta e^{2i\phi} \end{aligned} \tag{2.28}$$

For a spin-$\frac{1}{2}$ system, states are given by four levels, $|+\frac{1}{2}, +\frac{1}{2}>$, $|+\frac{1}{2}, -\frac{1}{2}>$, $|-\frac{1}{2}, +\frac{1}{2}>$, and $|-\frac{1}{2}, -\frac{1}{2}>$. Term A is proportional to $I_{1z}I_{2z}$, so it connects to the same state. Term B contains both a raising and lowering operator, so it simultaneously flips both spins, raising one spin state and lowering the other. Therefore, it only connects the zero energy state to the other degenerate zero energy state. In other words, both term A and term B connect states of the same energy, which may be the same state or states that are degenerate in energy. This allows for interactions between dipoles that do not emit energy, which account for the T_2 relaxation time decay (spin-spin).

Term C and Term D both include a single raising or lowering operator, and Term E and Term F both have two raising or lowering operators. Therefore, C, D, E, and F connects with different energy states, which allow energy absorptions. These four terms are the cause of T_1 relaxation time decay (spin-lattice).

2.5 Signal Localization

So far, the MRI signal can be generated through magnetization, RF excitations, and relaxations from a subject. However, this signal does not contain any spacial information.

The techniques introduced in this section can solve the dilemma, which is another key component of MRI, called spacial encoding. It includes slice selection, frequency encoding, and phase encoding.

2.5.1 Slice Selection

Slice selection is realized by a combination of gradient fields and a spatially selective RF pulse. Generally the thin slice is parallel with the transverse plane and the normal direction of the thin slice is the longitudinal direction. The slice select gradient is applied in the longitudinal direction, also called the z direction. Then the magnetic field is linearly changing along the z direction, so the Larmor frequency at different locations along the z axis is different. This one to one correspondence of a given distance along the gradient direction to a particular Larmor frequency leads to the possibility of tuning the RF pulse frequency to excite a slice at a desired spatial location.

The slice select gradient causes the frequency of precession to be a linear function of position along the slice select axis, such as the z axis. The frequency at position z is

$$f(z) = f_0 + \frac{\gamma}{2\pi} G_z z \tag{2.29}$$

where $f_0 = \gamma/2\pi B_0$ is the Larmor precession frequency at $z = 0$. The linear relation between $f(z)$ and z is illustrated in Figure 2.4.

The goal is to excite uniformly a slice such that all spins in the slice have identical phase and flip angle after slice selection. To excite an infinitesimal slice through z_0, the RF pulse must be tuned to the frequency given by Equation 2.29. Since the frequency spread of a realistic RF pulse is bounded, a region of finite thickness along the z direction within the object would have its spins tipped, while spins outside this region would ideally remain with B_0.

If we excite a slice of finite thickness extending from $z_0 - \Delta/2$ to $z_0 + \Delta/2$, the RF pulse should have a frequency profile, in the rotating frame, which is unity over the range Δf of frequencies from $[(\gamma/2\pi)G_z z_0 - (\gamma/2\pi)G_z \Delta z/2]$ to $[(\gamma/2\pi)G_z z_0 + (\gamma/2\pi)G_z \Delta z/2]$ and zero outside, as shown in Figure 2.5. The bandwidth BW_{rf} of the RF pulse, i.e., the width Δf of its region-of-support in the frequency domain, is given by

$$\begin{aligned} BW_{rf} &\equiv \Delta f \\ &= [(\gamma/2\pi)G_z z_0 + (\gamma/2\pi)G_z \Delta z/2] - [(\gamma/2\pi)G_z z_0 - (\gamma/2\pi)G_z \Delta z/2] \\ &= (\gamma/2\pi)G_z \Delta z \end{aligned} \tag{2.30}$$

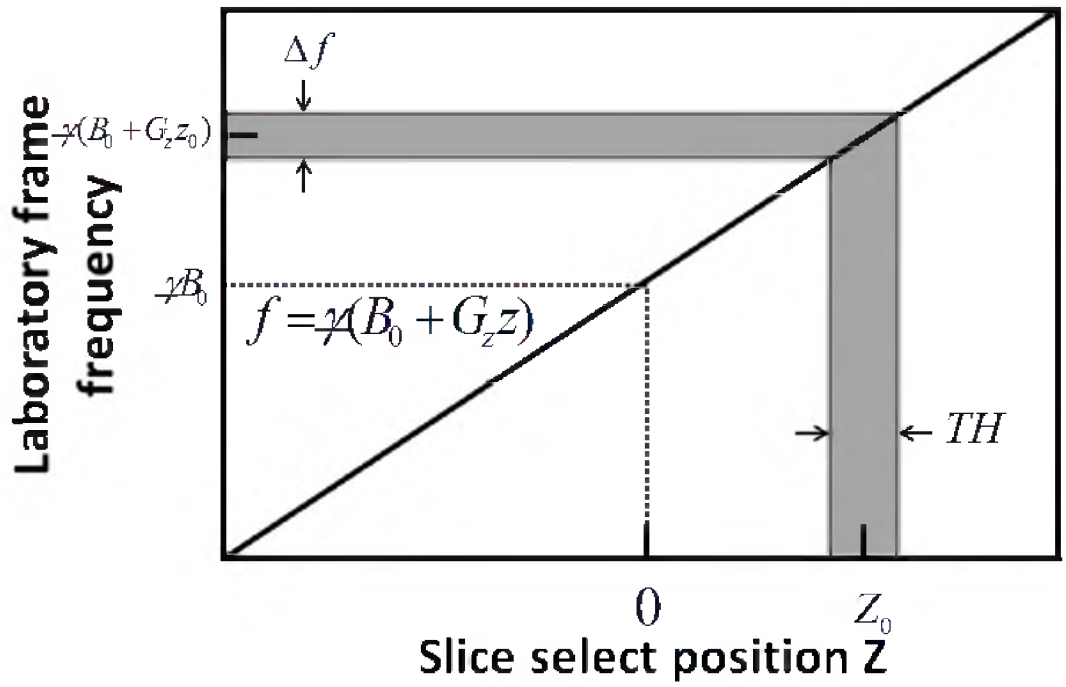

Figure 2.4: The linear relation between the precession frequency $f(z)$ and position z in the laboratory frame along the slice select axis when gradient G_z is applied. Images adapted from [66].

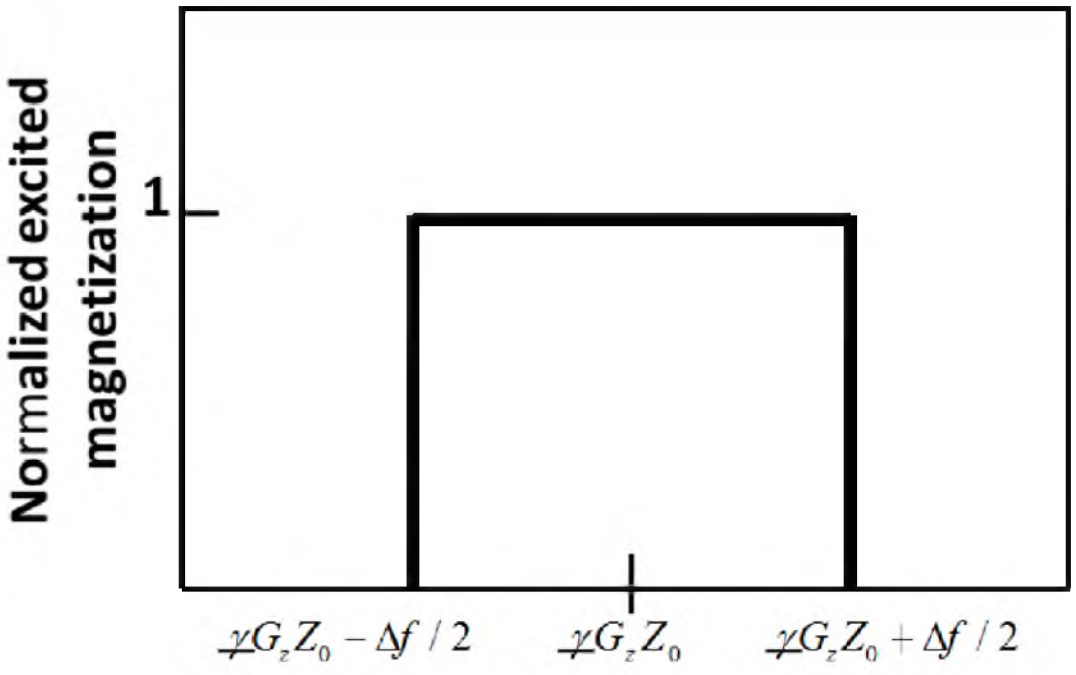

Figure 2.5: Excited magnetization (normalized) boxcar frequency profile in the Larmor rotating frame. Its temporal profile is that of an ideal (infinitely long) sinc pulse. Images adapted from [66].

The slice thickness is a function of the bandwidth BW_{rf} of the rf pulse and the applied gradient:

$$\Delta z \equiv TH \frac{BW_{rf}}{(\gamma/2\pi)G_z} \tag{2.31}$$

In order to get a uniform flip angle across the slice, the analytic form of the RF excitation profile, as a function of frequency, must be proportional to a boxcar function, $rect(f/\Delta f)$ of bandwidth Δf. This means that the temporal envelope of the RF pulse $B_1(t)$, which is the inverse Fourier transform of the boxcar frequency profile, is a sinc function.

$$B_1(t) \propto sinc(\pi \Delta f t) \tag{2.32}$$

However, the RF pulses are at the very least finite in their time duration, which the sinc RF needs to be truncated

$$B_1(t) = B_{1,ideal}(t) \cdot rect(\frac{t}{\tau_{rf}}) \tag{2.33}$$

Truncation leads to a frequency response, which is the convolution of the ideal response with a sinc function

$$B_1(f) = B_{1,ideal}(f) * (\tau_{rf} sinc(\pi f \tau_{rf})) \tag{2.34}$$

When the duration of the RF pulse increases, the function $\tau_{rf} sinc(\pi f \tau_{rf})$ approaches a δ-function. But the truncation artifacts, i.e., Gibbs ringing, will occur near sharp boundaries.

In practice, an additional apodizing function is used to bring $B_{1,ideal}(t)$ smoothly to zero and reduce truncation effects. Therefore, the more general expression for the time dependence of the field is

$$B_1(t) = B_{1,ideal}(t) \cdot a(t) \cdot rect(\frac{t}{\tau_{rf}}) \tag{2.35}$$

where $a(t)$ is an apodizing function and the frequency response of the pulse becomes

$$B_1(f) = B_{1,ideal}(f) * A(f) * rect(\frac{f}{\tau_{rf}}) \tag{2.36}$$

Figure 2.6 shows an example of the effects of truncation and apodization on an ideal field profile as a function of time and frequency. In Figure 2.6a, a truncated sinc function is shown, and the associated flip angle profile is show in Figure 2.6b. Figure 2.6c shows the same sinc function after apodization with a Hanning filter, while Figure 2.6d demonstrates the smoothing effect that apodization introduces.

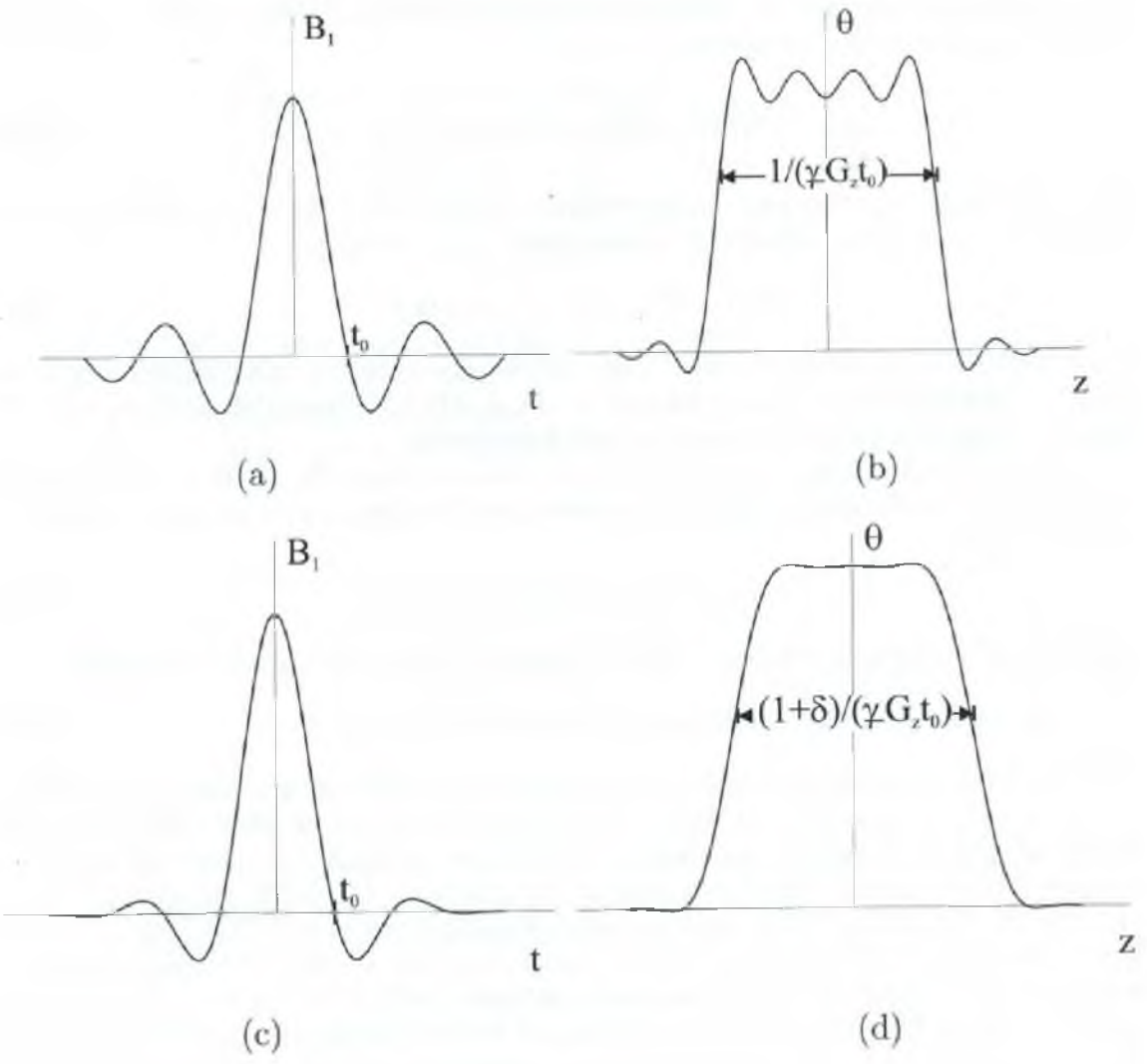

Figure 2.6: The effects of truncation and apodization on an ideal field profile as a function of time and frequency. Images adapted from [66].

2.5.2 Frequency Encoding

Frequency encoding allows the oscillation frequency of an activated magnetic resonance signal linearly dependent on its spatial origin along the readout direction, generally, the x direction. If the external static magnetic field is homogeneous, the Larmor frequency at position x is

$$\omega(x) = \omega_0 + G_x x \tag{2.37}$$

Without considering the transverse relaxation effect, the signal generated in an infinitesimal interval dx at point x takes the form,

$$dS(x,t) \propto \rho(x) dx e^{-i\gamma(B_0+G_x x)t} \tag{2.38}$$

where the coefficient of the equality is determined by the flip angle, static magnetic field (B_0), etc. If we ignore this coefficient, this equation can be rewritten as,

$$dS(x,t) = \rho(x) dx e^{-i\gamma(B_0+G_x x)t} \tag{2.39}$$

Now, because the oscillation frequency term is

$$\omega(x) = \gamma(B_0 + G_x x)t \tag{2.40}$$

which is a linear function of spatial location x, the signal is encoded with the position information along the readout direction. The signal received from the entire subject due to frequency encoding is

$$\begin{aligned} S(t) &= \int_{subject} dS(x,t) \\ &= \int_{-\infty}^{\infty} \rho(x) e^{-i\gamma(B_0+G_x x)t} dx \\ &= \left[\int_{-\infty}^{\infty} \rho(x) e^{-i\gamma G_x x t} dx \right] e^{-i\omega_0 t} \end{aligned} \tag{2.41}$$

After the demodulation, we have

$$S(t) = \int_{-\infty}^{\infty} \rho(x) e^{-i\gamma G_x x t} dx \tag{2.42}$$

The effect of frequency encoding of local MR signal can be illustrated in Figure 2.7.

2.5.3 Phase Encoding

Phase encoding uses a pulsed gradient to move the magnetization to a particular location in k-space. We will explain it through an one-dimensional example. After a RF pulse, the

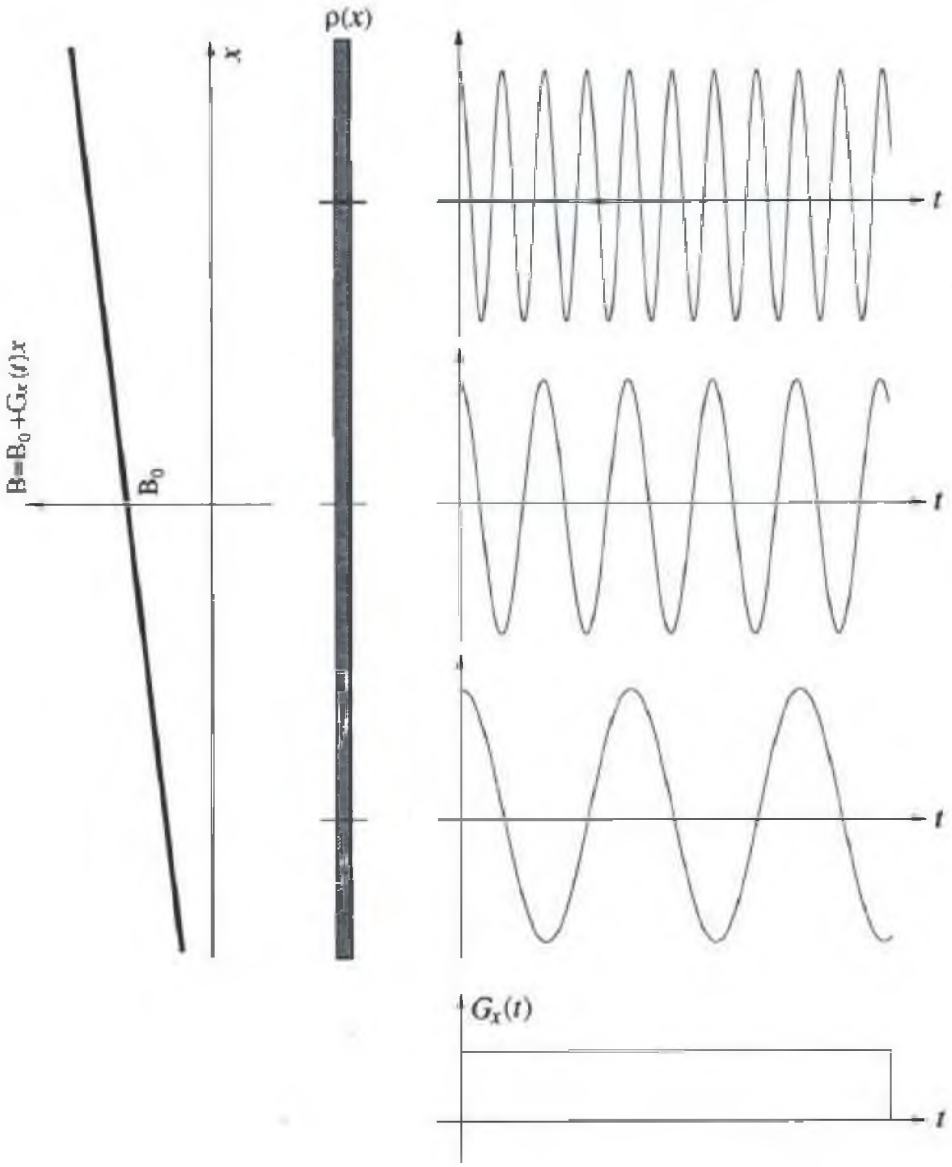

Figure 2.7: Localized signals from a hypothetical one-dimensional object in the presence of a frequency encoding gradient. Images adapted from [101]

gradient G_x is turned on for a short interval τ_{pe}, and then turned off. The local signal due to this gradient takes the form,

$$dS(x,t) = \begin{cases} \rho(x)e^{-i\gamma(B_0+G_x x)t} & 0 \le t \le \tau_{pe} \\ \rho(x)e^{-i\gamma G_x x \tau_{pe}} e^{-i\gamma B_0 t} & \tau_{pe} \le t \end{cases} \tag{2.43}$$

During time interval $0 \le t \le \tau_{pe}$, the local signal is frequency encoded. As shown in Figure 2.8, the signals from different x positions accumulate different phase angles after a time interval τ_{pe}. If we use τ_{pe} as a preparatory period, the signal collected aferward will carry an initial phase angle

$$\phi(x) = -\gamma G_x x \tau_{pe} \tag{2.44}$$

Now that $\phi(x)$ is linearly changed along the phase encoding direction, the signal is phase encoded. This gradient is also called the phase encoding gradient. Although an arbitrary phase encoding can be chosen, it generally is along the the y direction. So far, through the combination of slice selection, frequency encoding, and phase encoding, we can localize the signal in three-dimensional space, which makes it possible to generate three-dimensional images of a subject. Of course, these techniques still need to combined with the K-space sampling to generate the MRI signal. However, how we collect these signals is still a question.

2.6 How the MR Signal Gets Recorded

Faraday law of induction states that time varing magnetic flux through a conducting loop will induce an electromagnetic force, i.e., voltage, which is equal to the rate at which the magnetic flux though the coil is changing. In MRI, the magnetization is precessing at a radio frequency and any conducting loop resonating at the frequency can be used as a receiver coil. According to reciprocity principle, the inductive coupling of the receive coil to the magnetization may be described as equivalent to a constant flux, produced by a unit current flowing around the receive coil, which penetrates the precessing magnetization of the subject. Then the magnetic flux through the coil by $\vec{M}(r,t)$ is given by

$$\phi(t) = \int_{subject} \vec{B_r}(r) \cdot \vec{M}(r,t) dr \tag{2.45}$$

According to Faraday law of induction, the voltage $V(t)$ induced in the coil is

$$\begin{aligned} V(t) &= -\frac{\partial \phi(t)}{\partial t} \\ &= -\frac{\partial}{\partial t} \int_{subject} \vec{B_r}(r) \cdot \vec{M}(r,t) dr \end{aligned} \tag{2.46}$$

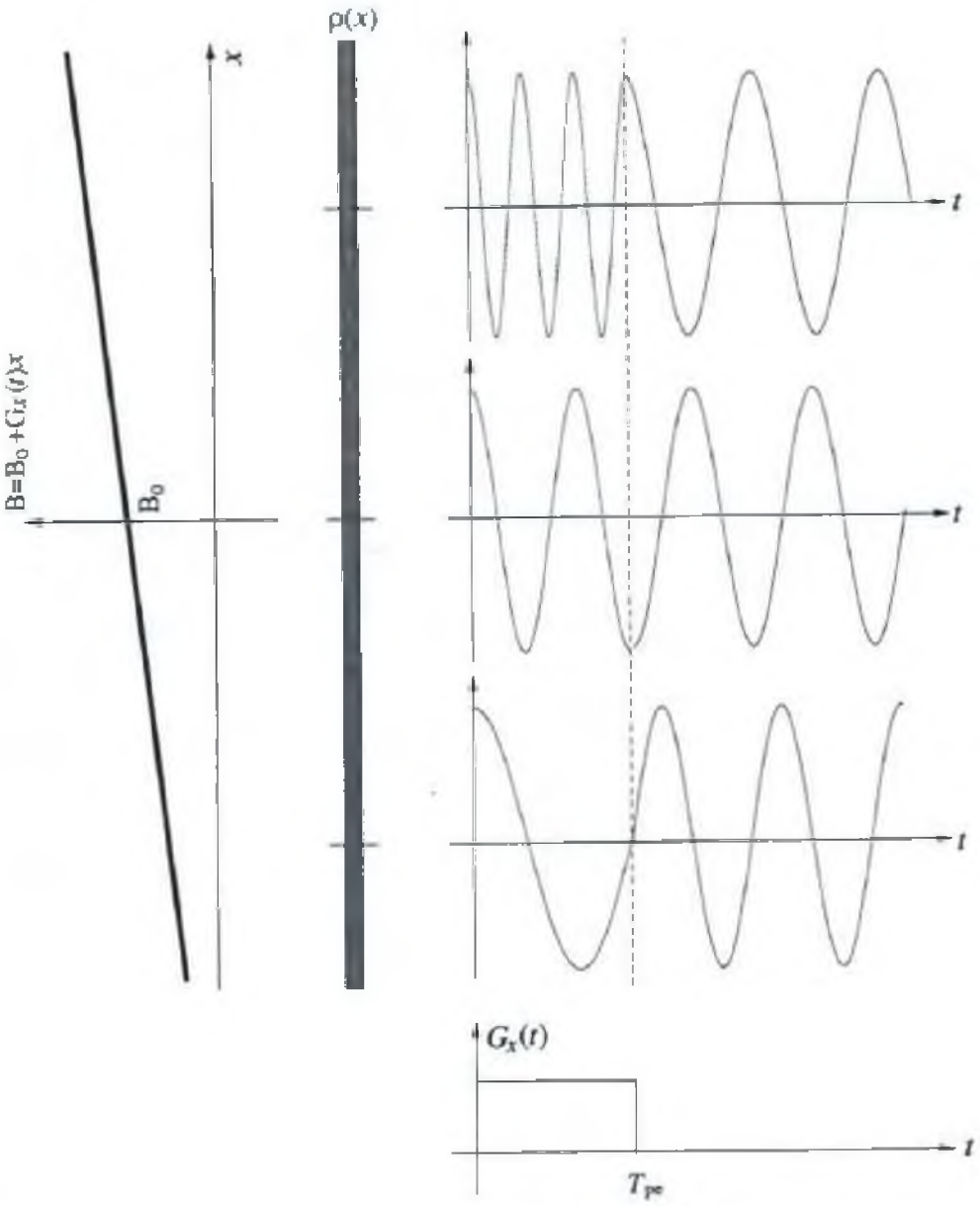

Figure 2.8: Phase encoded signals from a one-dimensional object. Images adapted from [101]

The voltage $V(t)$ induced in the receiver coil is often regarded as the raw NMR signal. If we rewrite the term $\vec{B_r}$ in the follwing format,

$$\vec{B_r} = B_{r,x}\vec{i} + B_{r,y}\vec{j} + B_{r,z}\vec{k} \tag{2.47}$$

Equation 2.46 changes to

$$V(t) = -\frac{\partial}{\partial t}\int_{subject} [B_{r,x}(r)M_x(r,t) + B_{r,y}(r)M_y(r,t) + B_{r,z}(r)M_z(r,t)]\, dr \tag{2.48}$$

Since the $M_z(r,t)$ is a slowly varing function compared to free precession of the M_x and M_y components, the last term can be ignored, yielding

$$\begin{aligned} V(t) &= -\frac{\partial}{\partial t}\int_{subject} [B_{r,x}(r)M_x(r,t) + B_{r,y}(r)M_y(r,t)]\, dr \\ &= -\int_{subject} \left[B_{r,x}(r)\frac{\partial M_x(r,t)}{\partial t} + B_{r,y}(r)\frac{\partial M_y(r,t)}{\partial t}\right] dr \end{aligned} \tag{2.49}$$

Equation 2.49 shows that the induced signal is a function of only the M_x and M_y term, i.e., transverse magnetization.

In order to achieve M_x and M_y, the Bloch equation (Equation 2.23) needs to be solved for the free precession case. The solution take the form,

$$M_{xy}(t) = M_{xy}(0)e^{-t/T_2}e^{-i\omega t} \tag{2.50}$$

where

$$M_{xy} = M_x + iM_y \tag{2.51}$$

and $M_{xy}(0)$ is referred to as the transverse magnetization immediately after RF pulse. Substituting Equation 2.50 into Equation 2.49, with necessary simplifications, we obtain

$$\begin{aligned} V(t) = -\int_{subject} &\omega(r)|B_{r,xy}(r)||M_{xy}(r,0)|e^{-t/T_2(r)} \\ &\cos\left[-\omega(r)t + \phi_e(r) - \phi_r(r) + \frac{\pi}{2}\right] dr \end{aligned} \tag{2.52}$$

Since this detected signal with high frequency can create problems for an electronic device, the technique, known as phase sensitive detection (PSD), is applied to move $V(t)$ to a low-frequency band. Then the signal is

$$V_{psd}^{1}(t) = \omega_0 \int_{subject} |B_{r,xy}(r)||M_{xy}(r,0)|e^{-t/T_2(r)} \cos\left[-\Delta\omega(r)t + \phi_e(r) - \phi_r(r) + \frac{\pi}{2}\right] dr \tag{2.53}$$

To determine whether the isochromat is precessing clockwise or counterclockwise, a second PSD system is used with reference signal $2\sin\omega_0 t$, which has a 90^o phase shift relative to the first PSD.

$$V_{psd}^{2}(t) = \omega_0 \int_{subject} |B_{r,xy}(r)||M_{xy}(r,0)|e^{-t/T_2(r)} \sin\left[-\Delta\omega(r)t + \phi_e(r) - \phi_r(r) + \frac{\pi}{2}\right] dr \tag{2.54}$$

By combining these two equations, the following equation is obtained,

$$\begin{aligned} S(t) &= V_{psd}^{1}(t) + iV_{psd}^{2}(t) \\ &= \omega_0 e^{i\pi/2} \int B_{r,xy}^{*}(r) M_{xy}(r,0) e^{-i\Delta\omega(r)t} dr \end{aligned} \tag{2.55}$$

where $B_{r,xy}^{*}r = |B_{r,xy}r|e^{-i\phi t}$, and $\omega = \omega_0 + \Delta\omega$. One can notice that this induced signal is proportional to $\omega_0 M_0$. Since $\omega_0 = \gamma B_0$ and $M_0 \propto (\gamma\hbar B_0)/(KT)$, then

$$signal \propto \frac{\gamma^3 B_0^2 \rho_0}{T} \tag{2.56}$$

which means the signal is proportional to the square of the external magnetic field B_0. This explains why researchers are interested in higher magnetic fields. Of course, higher magnetic fields have some other issues that need to be addressed carefully.

2.7 The Influence of Diffusion on the MRI Signal

Diffusion leads to random fluctuations in Larmor frequency and hence to a distribution of residual phase shifts at the echo center. The influence of self-diffusion on spin echo amplitudes was first discovered by Hahn [68], then the multiple echo scheme of Carr and Purcell [31] was proposed as a way of minimizing such effects. The effect of these modulations on the echo amplitude can provide a contrast mechanism which may be possible to image the molecular displacement, so as to image local structure information. This is exactly the idea of diffusion Magnetic Resonance Imaging (dMRI), which we will discuss in more details in Chapter 3.

The effect of molecular self-diffusion can be described by introducing an additional term in Bloch equations (Equation 2.23),

$$\frac{dM_x}{dt} = \gamma M_y(B_0 - \omega/\gamma) - M_x/T_2 + \nabla \cdot D \cdot \nabla M_x \tag{2.57}$$

which is the Bloch-Torrey equation about diffusion. Where γ is the gyromagnetic ratio of the hydrogen atom, G is the diffusion weighted gradient magnitude, and D is the self-diffusion coefficient. Here diffusion weighted gradient means a linearly changing magnetic field along a certainty direction, which will weight the local Brownian motion of the water molecule based on the direction and the strength of the diffusion. Therefore, G means how much the changing rate is with respect to the spacial position of this diffusion weighted gradient. In rotating frame, it can be written as

$$\frac{dM_+}{dt} = -i\gamma r \cdot GM_+ - M_+/T_2 + D\nabla^2 M_+ \tag{2.58}$$

Clearly, M_+ is a function of both r and t, so this equation can be solved by making the substitution,

$$M_+(r,t) = A(t)\exp\left[-i\gamma r \cdot \int_0^t G(t')dt'\right]\exp(-t/T_2) \tag{2.59}$$

Then,

$$\frac{\partial A(t)}{\partial t} = -D\gamma^2\left(\int_0^t G^*(t')dt'\right)^2 A(t) \tag{2.60}$$

The solution takes the form,

$$A(t) = \exp\left[-D\gamma^2\int_0^t\left(\int_0^t G^*(t'')dt''\right)^2 dt'\right] \tag{2.61}$$

The integrals are,

$$\begin{aligned}\int_0^t\int_0^t G^*(t'')dt''dt' &= -\int_d^{d+\delta} G(t'-d) - -\int_{d+\delta}^{d+\Delta} G\delta dt' \\ &+ \int_{d+\delta}^{d+\Delta+\delta}\left[-G\delta + G(t'-d-\Delta)\right]dt' \\ &+ \int_{d+\Delta+\delta}^{2\tau}\left[-G\delta + G\delta\right]dt' \\ &= -G\delta\Delta\end{aligned} \tag{2.62}$$

and

$$\begin{aligned}\int_0^t (\int_0^t G^*(t'')dt'')^2 dt' &= -\int_d^{d+\delta} G^2(t'-d)^2 - -\int_{d+\delta}^{d+\Delta} G^2\delta^2 dt' \\ &+ \int_{d+\delta}^{d+\Delta+\delta} \left[-G^2\delta^2 + 2G^2(t'-d-\Delta) + G^2(t'-d-\Delta)^2\right] dt' \\ &+ \int_{d+\Delta+\delta}^{2\tau} [-G\delta + G\delta]dt' \\ &= G^2\delta^2(\Delta - \delta/3)\end{aligned} \tag{2.63}$$

where Δ is the diffusion time, and δ is the diffusion gradient pulse duration. Both Δ and δ are shown in Figure 2.9, and d is the time duration between the $\frac{\pi}{2}$ RF pulse and the start of the first diffusion weighted gradient pulse in Figure 2.9. Now the attenuation takes the form,

$$\exp\left[-D\gamma^2G^2\delta^2(\Delta - \delta/3)\right] = \exp[-bD] \tag{2.64}$$

where

$$b = \gamma^2G^2\delta^2(\Delta - \delta/3) \tag{2.65}$$

which is the so called b-value in diffusion Magnetic Resonance Imaging. Figure 2.9 shows a standard 'Stejskal-Tanner' spin echo pulse sequence with slice selective and diffusion selective gradients applied along one physical dimension (shaded). The reader needs to notice that the gradient pulse cannot be a perfect short square wave in practice. Figure 2.10 shows an extreme case of how the gradient pulse looks, and the ramp-up and ramp-down times of the gradient cannot be ignored. In such cases, the derivation shown in this section is not valid. In other words, The result is an approximation when $\delta \to 0$.

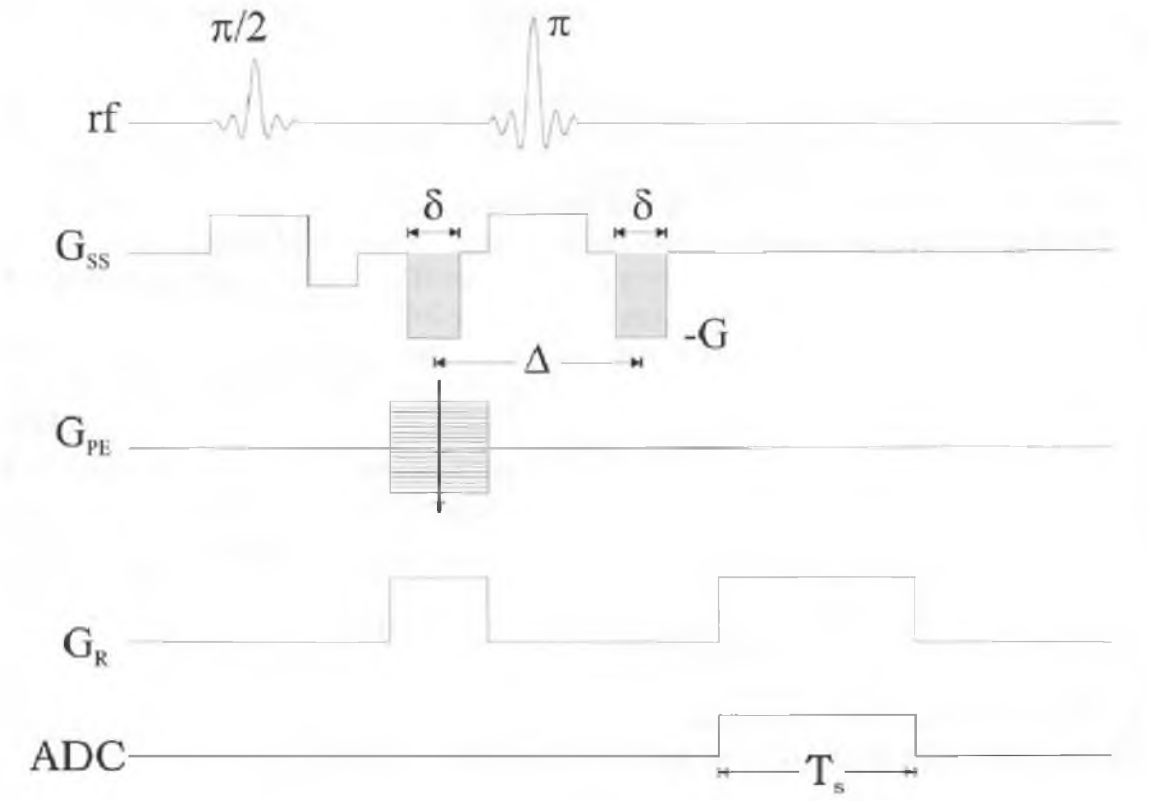

Figure 2.9: standard 'Stejskal-Tanner' spin echo pulse sequence with slice selective and diffusion selective gradients applied along one physical dimension (shaded). Images adapted from [66]

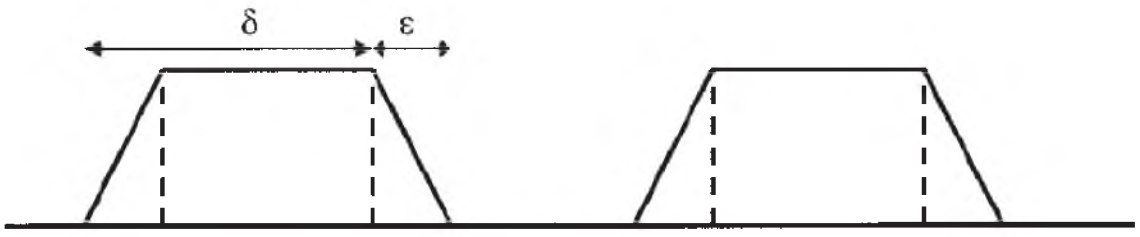

Figure 2.10: A diffusion sensitizing gradient pulse.

CHAPTER 3

THE BASICS OF DIFFUSION TENSOR IMAGING (DTI), HIGH ANGULAR RESOLUTION DIFFUSION IMAGING (HARDI)

In this chapter, we will give a brief introduction about diffusion tensor imaging (DTI), high angular resolution diffusion imaging (HARDI), and fiber tractography algorithms. Section 2.1 introduces the basics of diffusion tensor imaging and its limitations, and a short introduction about fiber tractography algorithms. Section 2.2 presents a more recent technique: high angular resolution diffusion imaging (HARDI).

3.1 Overview of Diffusion Tensor Imaging (DTI)

Diffusion tensor imaging (DTI), invented by Basser et al. in the early 1990s [13], is a noninvasive technique to delineate the three-dimensional structure of brain white matter *in vivo*. By applying appropriate magnetic field gradients, diffusion weighted magnetic resonance images were obtained. Then a diffusion tensor at each voxel can be solved according to the Stejskal-Tanner equation.

$$S_i = S_0 e^{-b g_i^T D g_i} \tag{3.1}$$

where b is b value (Equation 2.65), g_i is diffusion weighted gradient direction (the direction along which the diffusion weighted gradient was applied; please refer to Section 2.7 for more details.), S_i are diffusion weighted images, S_0 is the baseline image without applying the diffusion gradient, and D is a second-order symmetric diffusion tensor. Since D has six independent components, which are the unknown variables, at least six S_is and one B0 are needed to solve Equation 3.1. The widely used method to solve this linear system is linear least squares [13]; also the weighted least squares shows the optimal properties (minimum variance) [130]. Although some other approaches are applicable [51], the least squares techniques are generally faster and more robust.

Human brain white matter contains neuros, but mainly axons. For the human brain, the voxel size is in the range of 1 mm $\sim$ 2 mm cube, while the diameter of each single axon is around 10 microns. Therefore, diffusion tensor actually measures the ensemble average of the restricted (limited by axon boundaries) diffusion properties of a water molecule within the imaging voxel. Through the study of this diffusion tensor, more local structure information of human brain white matter can be obtained.

After solving each tensor component, we now have the the symmetric second-order tensor $\mathbf{D}$ at each voxel.

$$D = \begin{pmatrix} D_{xx} & D_{xy} & D_{xz} \\ D_{xy} & D_{yy} & D_{yz} \\ D_{xz} & D_{yz} & D_{zz} \end{pmatrix}$$

The diffusion tensor can be decomposed into the eigen system

$$D = R\lambda R^T \tag{3.2}$$

where $\mathbf{R} = (\mathbf{e_1}, \mathbf{e_2}, \mathbf{e_3},)$ is a column matrix of the eigenvector e_v, and $\lambda = diag(\lambda_1, \lambda_2, \lambda_3)$ is a diagonal matrix of the eigenvalues λ_v, with $\lambda_1 \geq \lambda_2 \geq \lambda_3$. Each eigenvalue represents the apparent diffusivity along each corresponding eigenvector direction. The diffusion tensor may be easily visualized as an ellipsoid whose diameter in any direction estimates the diffusivity in that direction and whose major principle axis is oriented in the direction of maximum eigenvalue. Figure 3.1 shows the ellipsoid visualization in the region of interest in human brain white matter.

Different scalar measures can be defined to measure the degree of anisotropy and the properties of diffusion: fractional anisotropy (FA), linear anisotropy(C_l), and mean diffusivity(MD), etc. Fractional anisotropy, which can give a clear contrast between brain white matter and gray matter, is the most widely adopted scalar measure. In pure water (Cerebrospinal Fluid), the diffusion is characterized as *isotropic*, meaning that its diffusion magnitude is equal in all directions and the FA value will be zero or very low. In fibrous tissue (White Matter), however, the diffusion becomes restricted and shows a more or less distinct *anisotropy*, meaning that the diffusion magnitude depends on direction [18] and the FA value will be higher.

$$FA = \frac{\sqrt{(\lambda_1 - \lambda_2)^2 + (\lambda_2 - \lambda_3)^2 + (\lambda_3 - \lambda_1)^2}}{\sqrt{2(\lambda_1^2 + \lambda_2^2 + \lambda_3^2)}} \tag{3.3}$$

$$C_l = \frac{(\lambda_1 - \lambda_2)}{(\lambda_1 + \lambda_2 + \lambda_3)} \tag{3.4}$$

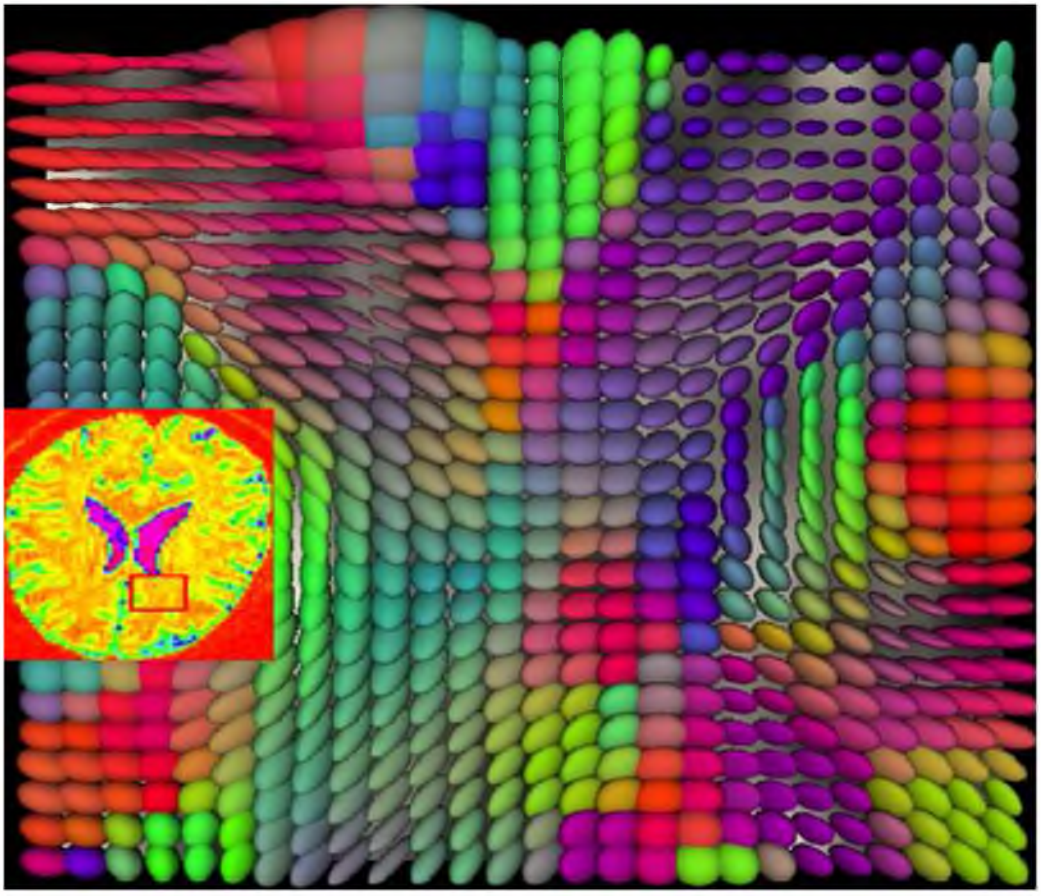

Figure 3.1: Ellipsoid visualization of region of interest in human brain white matter. The enlarged image shows ellipsoid at each voxel in ROI, and the ROI was shown as an embedded image. The color was coded based on the major direction of the diffusion tensor. If the the major direction is aligned with left-right direction, the color of the ellipsoid will be red. If the the major direction is aligned with up-low direction, the color of the ellipsoid will be green. If the the major direction is aligned with in-out plane direction, the color of the ellipsoid will be blue. If the the major direction is somewhere in between, the color of the ellipsoid will be interpolated. For the embedded image, the color was coded based on the intensity value using HSV colormap defined in MATLAB.

$$MD = tr(D)/3 = (\lambda_1 + \lambda_2 + \lambda_3)/3 \tag{3.5}$$

It has been shown that the direction of the largest eigenvalue coincides with the white matter fiber tract orientations [110]. Fiber tractography algorithms [15, 158, 98, 116, 33, 56], which integrate along the major eigenvector field to form the architectural connections of white matter structure, have been proposed. These tracking algorithms fall into two main categories: deterministic tractography [15, 158, 98, 116, 33] or probabilistic tractography [56]. Figure 3.2 shows the fiber tracking results on a human brain data based on the streamline algorithm. Compared with the human brain anatomy (bottom right corner), the fiber tractography can generate similar trends as with real anatomy.

Deterministic tracking algorithms are based on the assumption that the largest eigenvector direction of a diffusion tensor aligns with the dominant fiber orientation(s) in each voxel, while the probabilistic algorithms calculate the probability of a connection between

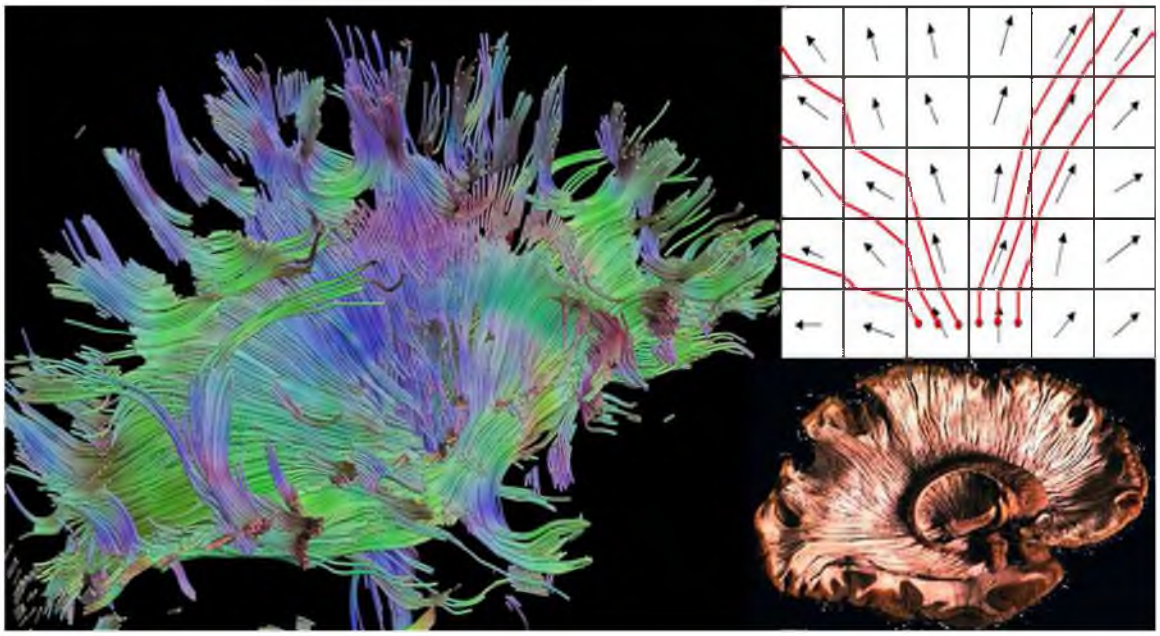

Figure 3.2: Fiber tractography on human brain based on streamline algorithm. The color was coded based on the local fiber direction of each fiber track. If the the fiber direction is aligned with left-right direction, the color of the local fiber segment will be red. If the the local fiber direction is aligned with up-low direction, the color of the local fiber segment will be green. If the the local fiber direction is aligned with in-out plane direction, the color of the local fiber segment will be blue. If the the local fiber direction is somewhere in between, the color of the local fiber segment will be interpolated. Top right corner shows how the algorithm works in the 2D setting. Bottom right corner shows a human brain anatomy. Courtesy of G. Kindlmann and P. Mukherjee (top right corner).

two anatomical regions. Fiber tractography is a noninvasive way to infer the white matter connectivity of the brain, which starts to be used in clinical applications. It can also be used in surgical planning [21, 23], in pediatric subjects [60, 117, 24, 47], in elderly subjects [139], and in patients with schizophrenia [83], brain tumors [129], Alzheimer disease [140], etc. Although DTI is still the most wide spread technique, it underestimates the complex diffusion patterns in areas of fiber crossing, kissing, and branching, etc., due to the assumption of a Gaussian probability distribution function. Therefore, the HARDI technique emerged.

3.2 Brief Introduction of High Angular Resolution Diffusion Imaging (HARDI)

High Angular Resolution Diffusion Imaging (HARDI) was proposed by Tuch et al. [148, 149] to enable a more precise angular characterization of the diffusion signal. Based on different mathematical modes used, HARDI techniques may be further divided into three major categories: high angular apparent diffusion coefficient(ADC) modeling, diffusion propagator model, and fiber models. A more detailed review can be found in [8].

3.2.1 High Angular Apparent Diffusion Coefficient(ADC)

Higher angular apparent diffusion coefficient was a direct generalization of modeling the apparent diffusion coefficient from a low to a high angular resolution without the Gaussian assumption imposed by DTI [74, 147, 4, 54]. It allows high angular modeling of the ADC by using a higher-order tensor (at least fourth-order) rather than a second-order tensor in Eq. 3.1. Higher-order tensor contains more unknowns, which require diffusion weighted images in more noncolinear diffusion weighted directions. Since a fully symmetric fourth-order tensor contains fifteen unknowns, at least fifteen diffusion weighted images need to be acquired to recover all of the independent components of the fourth-order tensors in each voxel. Descoteaux et al. [43] and Özarslan et al. [165] formalize the ADC model as the following

$$D(\mathbf{g}) = \sum_{j=1}^{J_l} \mu_j D_j \prod_{p=1}^{l} \mathbf{g}_j(p) \tag{3.6}$$

where D_j is the j^{th} independent component of the tensor, μ_j is its corresponding multiplicity, and $g_j(p)$ is the component of the gradient direction g corresponding to the p^{th} index of the j^{th} independent component. Several studies suggested the use of spherical harmonics (SH) for angular ADC estimation [74, 54, 4, 32]

$$D(\mathbf{g}) = \sum_{j=0}^{J_l} C_j Y_j(\mathbf{g}) \tag{3.7}$$

where the symbol $J_l = (l+1)(l+2)/2$ corresponds to the number of terms of an order l harmonic expansion, the symbol Y_j stands for the real and symmetric spherical harmonics. These two forms are equivalent under the linear transform of

$$C_m = \sum_{j=1}^{J_l} D_j \int_{\Omega} \mu_j \prod_{p=1}^{l} g_j(p)(g) Y_m(g) dg \tag{3.8}$$

with the matrix form as

$$C = MD \tag{3.9}$$

where

$$M = \begin{pmatrix} \mu_1 \int_{\Omega} \prod_{p=1}^{l} g_1(p)(g) Y_1(g) dg & \cdots & \mu_{J_l} \int_{\Omega} \prod_{p=1}^{l} g_1(p)(g) Y_1(g) dg \\ \vdots & \ddots & \vdots \\ \mu_1 \int_{\Omega} \prod_{p=1}^{l} g_1(p)(g) Y_{J_l}(g) dg & \cdots & \mu_{J_l} \int_{\Omega} \prod_{p=1}^{l} g_1(p)(g) Y_{J_l}(g) dg \end{pmatrix}$$

The higher-order tensor modeling technique resolve the brain regions with complex configuration, such as crossing, kissing, etc., which are problematic cases for DTI [4, 54, 167]. However, the maxima of ADC profiles are not aligned with the underlying fiber directions [67]. This prevents the extraction of accurate fiber directions, which is crucial for fiber tracking algorithms.

3.2.2 Diffusion Propagator

Diffusion propagator is probably the most widely used HARDI technique. Q-ball imaging, Diffusion Orientation Transform (DOT), and Diffusion Spectrum Imaging (DSI) all belong to this category.

3.2.2.1 Q-ball Imaging

Tuch [147] showed that diffusion orientation distribution (ODF) could be estimated directly from a diffusion signal measured on a single sphere of q-space without the full probability distribution function (PDF) information. It relies on the fact that the PDF is related to the measured diffusion signal by Fourier transform,

$$P(\mathbf{r}) = \mathcal{F}[E(\mathbf{q})] = \int_{r \in R^3} E(\mathbf{q}) \exp\left(-2\pi i \mathbf{q} \cdot \mathbf{r}\right) d\mathbf{q} \tag{3.10}$$

The ODF is the radial projection of the diffusion function,

$$\Psi(\mathbf{u}) = \frac{1}{Z}\int_0^\infty P(r\mathbf{u})dr \tag{3.11}$$

where Z is the dimensionless normalization constant. This actually is the zero-order radial projection of,

$$ODF_k(k) = \frac{1}{Z_k}\int_{r=0}^\infty P(r\mathbf{k})r^k dr \tag{3.12}$$

Tuch employed the Funk-Radon transform to approximate the ODF, which treats each point on the sphere as a pole and assigns the integral over the associated equator to it.

$$\begin{aligned}\Psi_{q'}(\mathbf{w}) &= \int_{u\in S^2} E(q'\mathbf{u})\delta(\mathbf{U}^\mathbf{T}\mathbf{w})du \\ &= 2\pi q' \int_{r\in R^3} P(\mathbf{r})J_0(2\pi q' r)\delta(1-\mathbf{r}^\mathbf{T}\mathbf{w}))dr\end{aligned} \tag{3.13}$$

where $w \in S^2$ and the symbol J_0 represent the zeroth order Bessel function of the first kind [1]. Following Tuch's work, The spherical harmonics basis , which lowers the number of samples needed, was introduced [5, 72, 44].

$$E(\mathbf{q}) = \sum_{l=0}^{L}\sum_{m=-l}^{l} a_{lm}Y_l^m(\mathbf{u})\delta(q-q') \tag{3.14}$$

where E is the normalized diffusion weighted signal, $q\prime$ is the radius of HARDI acquisition q-space sphere, and $\mathbf{u}$ is a three-dimensional unit vector. This simplifies the computation of the Funk-Radon transform stated by the Funk-Hecke theorem [6], and only involves a matrix multiplication between the coefficient of a_{lm} and $P_l(0)$.

$$\Psi_{q'}(\mathbf{w}) = \sum_{l=0}^{L}\sum_{m=-l}^{l} 2\pi P_l(0)a_{lm}Y_l^m(\mathbf{w}) \tag{3.15}$$

The obtained ODF by QBI method [147] has a low angular contrast due to the assumption of $P(\mathbf{r}) \approx P(\mathbf{r})J_0(2\pi q'\mathbf{r})$ and the drop of r^2 term in Eq. 3.11. To solve this problem, either a min-max normalization [147] or a deconvolution with the Laplace- Beltrami operator [45] was used as the postprocessing step.

3.2.2.2 Diffusion Orientation Transform (DOT)

Diffusion Orientation Transform (DOT) [166], based on { mono,bi,tri } -exponential decay assumption on diffusion signal attenuation $E(\mathbf{q})$, gives the full information about $E(\mathbf{q})$ in the three-dimensional q-space from the only single shell $E(\mathbf{q_0u})$. The key idea of

DOT is to use Rayleigh expansion of a plane wave in the spherical coordinate to do Fourier transform. The $\exp(-2\pi i\mathbf{q}\cdot\mathbf{r}d\mathbf{q})$ term in Eq. 3.10 can be expanded as,

$$e^{\pm 2\pi i\mathbf{q}\cdot\mathbf{r}} = 4\pi \sum_{l=0}^{\infty} \sum_{m=-l}^{l} (\pm i)^l j_l(2\pi qr) Y_l^m(\mathbf{u}) * Y_l^m(\mathbf{r}) \tag{3.16}$$

where $q = |\mathbf{q}|$ and $r = |\mathbf{r}|$. The term $j_l(2\pi qr)$ is the l-th order spherical Bessel function whereas $Y_l^m(\mathbf{u})$ is the spherical harmonic function. Then Eq. 3.10 can be rewritten as,

$$P(R_0\mathbf{u}) = \sum_{l=0}^{\infty} \sum_{m=-l}^{l} (-i)^l Y_l^m(\mathbf{r}) \int d\mathbf{u} Y_l^m(\mathbf{u}) * I_l(\mathbf{u}) \tag{3.17}$$

where

$$I_l(\mathbf{u}) = 4\pi \int_0^{\infty} dq q^2 j_l(2\pi q R_0) \exp(-4\pi^2 q^2 t D(\mathbf{u})) \tag{3.18}$$

It reconstructs the diffusion propagator $P(R_0\mathbf{u})$ at a given radius R_0, given that $P(R_0\mathbf{u})$ denotes $p(\mathbf{r}|\mathbf{r}_0, \tau)$ for a constant time $t = \tau$. Here the $P(R_0\mathbf{u})$ means the probability of finding the particles, which initially were at origin, at the point $R_0\mathbf{u}$. This means we want to calculate the probability on a sphere of radius R_0, which is an additional parameter that has to be determined in advance.

Since Eq. 3.18 is a function of orientation, it can be expanded in a Laplace series and can be evaluated analytically.

$$I_l(\mathbf{u}) = \sum_{l'=0}^{\infty} \sum_{m'=-l'}^{l'} \alpha_{ll'm} Y_{l'm'}(\mathbf{u}) \tag{3.19}$$

Inserting this expression into Eq. 3.17, we get

$$P(R_0\mathbf{u}) = \sum_{l=0}^{\infty} \sum_{m=-l}^{l} p_{lm} Y_l^m((u)) \tag{3.20}$$

with

$$p_{lm} = (-1)^{l/2} \int Y_l^m(\mathbf{u}) * I_l(\mathbf{u}) d\mathbf{u} \tag{3.21}$$

3.2.2.3 Diffusion Spectrum Imaging (DSI)

Diffusion Spectrum Imaging (DSI) [157, 147] samples the entire q-space in three dimensions, rather than only one spherical q-space surface in Q-ball Imaging (Sec. 3.2.2.1). It can acquire both the angular information and the radical information of the diffusion process denoted Ensemble Average Propagator (EAP), and requires very few prior assumptions.

The simplied expression for the b value takes the form of $b = \gamma^2 G^2 \delta^2 (\Delta - \delta/3)$ (Equation 2.65). The so called q value takes the form,

$$q = (2\pi)^{-1} \gamma \delta G \tag{3.22}$$

This leads to the following expression

$$b(q) = 4\pi^2 q^2 (\Delta - \delta/3) \tag{3.23}$$

where Δ is the time interval between two diffusion gradients, also called diffusion time. δ is the duration of the diffusion gradient and G is the magnitude of the diffusion gradient. γ is the gyromagnetic ratio for water protons, which is a physical constant. To fully explorer the q-space, q value or b value need to be very large. However, δ needs to be small to satisfy the narrow pulse approximation. From Eq. 3.22, we can see that G needs to be very large, which will create heavy eddy current distortions and even possibly induce harmful electric fields in the subject. In addition, DSI needs to acquire multiple shells in q space with many diffusion weighted directions, which lead to a much longer data acquisition time. All of these are the severe technical limitations of DSI.

3.2.3 Fiber Model Approaches

3.2.3.1 Mixture Models

The basic idea of the mixture models is that the diffusion signal can be decomposed as a weighted sum of generic diffusion models h_i:

$$E(\mathbf{q}) = \sum_{i=1}^{n} f_i h_i(\mathbf{q}) \text{ with } \sum_{i=1}^{n} f_i = 1 \tag{3.24}$$

The multi-Gaussian model [147] is the direct generalization of the DTI model, which assumes that the diffusion signal can be modeled as the sum of several second-order tensors:

$$h_i(\mathbf{q}) = \exp(-4\pi^2 \tau \mathbf{q}^\mathbf{T} \mathbf{D_i} \mathbf{q}) \tag{3.25}$$

The Ball and Stick model [20, 75] models the signal as two components: isotropic compartment (ball) and anisotropic compartments (stick).

$$h_{iso}(\mathbf{q}) = \exp(-4\pi^2 q^2 \tau \mathbf{D_{iso}}) \tag{3.26}$$

$$h_{aniso}(\mathbf{q}) = \exp(-4\pi^2 q^2 \tau u^T \mathbf{D_{aniso}} u) \tag{3.27}$$

The mixture models are very intuitive and the peak interference is taken into account automatically. However, the estimation of mixture models is generally nonlinear and is

obtained by iterative computations, which makes the model estimation process unreliable and inefficient. In addition, the appropriate number of fibers need to be determined in advance.

3.2.3.2 Spherical Deconvolution

Spherical Deconvolution was put forward by Tournier et al. [143]. It assumes the diffusion signal is the convolution of the single fiber response function with the expected true fiber distribution, rather than a discrete number of fiber bundles used in mixture modes. Later linear or nonlinear methods have been put forward to resolve the issues like instability, noise, and negative diffusivity [78, 77, 5, 126, 40, 86]. One disadvantage of Spherical Deconvolution is that a fiber response function needs to be assumed a priori. It either can be a choice based on experience [3] or calculated by statistical estimation on the whole diffusion image [143, 78]. We will review Spherical Deconvolution in more detail in Chapter 4.

CHAPTER 4

DETECTION OF CROSSING WHITE MATTER FIBERS WITH HIGH-ORDER TENSORS AND RANK-K DECOMPOSITIONS

Fundamental to high angular resolution diffusion imaging (HARDI) is the estimation of a positive-semidefinite orientation distribution function (ODF) and extracting the diffusion properties (e.g., fiber directions). In this chapter, we show that these two goals can be achieved efficiently by using homogeneous polynomials to represent the ODF in the spherical deconvolution approach, as was proposed in the Cartesian Tensor-ODF (CT-ODF) formulation. Based on this formulation, we first suggest an estimation method for positive-semidefinite ODF by solving a linear programming problem that does not require special parametrization of the ODF. We also propose a rank-k tensor decomposition, known as CP decomposition, to extract the fibers information from the estimated ODF. We show that this decomposition is superior to the fiber direction estimation via ODF maxima detection as it enables one to reach the full fiber separation resolution of the estimation technique. We assess the accuracy of this new framework by applying it to synthetic and experimentally obtained HARDI data.

4.1 Introduction

Diffusion Tensor MRI (DT-MRI) measures the Brownian motion of water molecules in a tissue and enables one to reveal its diffusion properties. It is primarily used to infer the white matter connectivity of the brain. The signal attenuation model in DT-MRI is given by Equation 3.1. In traditional DTI, the ADC is modeled by a quadratic form $D(\mathbf{g}) = \mathbf{g}^T \mathrm{D} \mathbf{g}$, where D is a second-order tensor known as diffusion tensor. Since $D(\mathbf{g})$ is a quadratic form, the modeled ADC is elliptic and thus cannot model complex structures such as crossing fibers. To overcome the limitations of DTI, High Angular Resolution Diffusion

Imaging (HARDI) is used. Different modalities and estimation techniques associated with HARDI have been proposed over the years. These methods include the multicompartment model [150], Q-ball imaging (QBI) [149, 44], spherical deconvolution [143, 3], Diffusion Orientation Transform (DOT) [113], OPDF [146], and methods that describe the ADC profile using high-order tensors [10, 12]. These latter methods represent $D(\mathbf{g})$ as an even-order homogeneous polynomial whose coefficients are identified with the entries of a high-order tensor. The resulting function can describe multiple maxima and can be used to model complex fiber structures. Unfortunately, in contrast to the diffusion tensor model, the maxima of the ADC profile described by a high-order homogeneous polynomial do not correspond to the underlying fiber directions. This is solved by computing the diffusion propagator and locating the fiber directions at its local maxima. This computation involves a nontrivial Fourier transform step that adds complexity to the estimation process. To solve this problem, it was proposed in [159] to combine the high-order tensor formulation with the spherical deconvolution technique. This strategy enables one to estimate a positive-definite ODF, dubbed Cartesian Tensor-ODF (CT-ODF), whose maxima correspond to the orientations of the fibers.

Although finding all the local maxima of higher-order spherical functions is not trivial, only a handful of papers have been devoted to this important issue [26, 2, 135]. It turns out that since each maximum has a finite width, maxima tend to interfere below a certain fiber separation angle. Therefore, using maxima finding, the maximal fiber separation resolution enabled by the data acquisition technique cannot be reached. An interesting solution to this problem was proposed in [135]. The ODFs in that case were estimated using the Q-Ball imaging technique and then were converted to high-order tensors using a linear transformation. Then, a heuristic rank-k tensor approximation was applied to the tensors to extract the fiber directions beyond the resolution limit determined by the maxima. This method was later used to initialize the ball-and-stick model [136]. Although the proposed method was applied successfully to synthetic and real data, it has some inherent limitations: To calculate the different rank-1 tensors that contribute to the rank-k approximation, rank-1 tensor subtractions were used. It is known that rank-1 tensor subtractions can potentially increase the tensor rank [138] and hence, the convergence of the algorithm is not guaranteed. Furthermore, although the initial ODF is non-negative, the residuals obtained by these subtractions do not have this property. In this chapter, we address these problems and in addition to a new ODF estimation technique, we propose an alternative way to decompose the tensors.

This chapter is organized as follows: We first develop the estimation technique for positive-semidefinite ODFs of any order. This estimation method is based on the CT-ODF formulation for high-order tensors proposed by Weldeselassie et al. [159]. Then, we formulate the estimation problem as a linear programming problem with linear constraints that enforce non-negativity of the ODF. For extracting the individual fiber properties, we apply a rank-k tensor decomposition, known as the CP decomposition, to the ODF. In addition to providing the fiber directions, the decomposition also enables us to estimate the fiber fractions. Finally, we demonstrate our proposed technique on synthetic and real HARDI data and show that the proposed algorithm provides accurate results and can reliably resolve two crossing fibers with much higher fidelity than by maxima detection. We confirm the accuracy of the algorithm on both synthetic, phantom, and real HARDI data.

4.2 Spherical Deconvolution

Following the work by Tournier et al. [143], the Diffusion-Weighted MR signal can be modeled by a spherical convolution of an orientation distribution function (ODF) with an axially symmetric kernel, K:

$$S(\mathbf{g}, b) = S_0 \int_{S^2} F(\mathbf{v}) K(\mathbf{g}, \mathbf{v}, b) d\mathbf{v}, \tag{4.1}$$

where $\mathbf{g}$ is the gradient direction. The function F is associated with the ODF (or fiber-ODF in Tournier's original work), and it is composed of a sum of k delta functions, each is oriented along one fiber direction and weighted according to the corresponding fiber fraction. The kernel K can be chosen in various ways depending on the dataset and the region in the brain (e.g., [11, 3]). A very common choice is the single fiber response which is described by the bipolar Watson function

$$K(\mathbf{g} \cdot \mathbf{v}, b) = e^{-c(\mathbf{g}^T \mathbf{v})^2}, \tag{4.2}$$

where the concentration parameter, c, is a function of the b value and the diffusivity. Given the measured DW-signal and a kernel, which is known *a priori*, the ODF is computed by performing spherical deconvolution of K from $S(\mathbf{g}, b)$. Technically, this may be solved using least squares where the solution is given by a simple pseudo-inverse operation [143].

In [159], it was proposed to represent F as a spherical, even-order, and positive-definite homogeneous polynomial induced by a high-order tensor. In that work, it was suggested to use the single fiber response kernel described in Eq. (4.2). The concentration parameter was chosen to be large enough to describe a diffusion process which is highly restricted perpendicular to the orientation $\mathbf{v}$. We use the same ideas here.

Any ODF estimated from the data has to be non-negative. In [159], a special parametrization was used to yield a positive-definite ODF. In this section, we show that the same goal can be achieved by minimizing an objective function subject to linear constraints that enforce the positivity on the ODF. That is, given measurements in n gradient directions, we aim to solve the following problem:

$$\min_F \frac{1}{2}\sum_{i=1}^{n}\left\| S(\mathbf{g}_i,b) - S_0\int_{S^2} F(\mathbf{v})K(\mathbf{g}_i,\mathbf{v},b)d\mathbf{v}\right\|^2 \tag{4.3}$$

subject to

$$F(\mathbf{g}_i)\geq 0, \quad \mathbf{g}_1,\ldots,\mathbf{g}_n\in S^2.$$

The solution to this problem guarantees positive-semidefiniteness in the discrete sense, that is, in the directions which were used to acquire the signal. We believe that under certain conditions, the estimated ODF will be positive-semidefinite in every direction on the sphere. However, since this is an open problem, we leave the complete mathematical study as future work.

We now formulate the problem explicitly. This formulation holds for tensors of any order; however, in this chapter, we only consider fourth-order tensors that are also *supersymmetric*. Here we will refer to a supersymmetric tensor by using the term *symmetric*. The coefficients of a symmetric fourth-order tensor are invariant under any permutation of the indices. Thus, a symmetric fourth-order tensor has 15 unique coefficients associated with a homogeneous polynomial:

$$F(\mathbf{g}) = \sum_{a=0}^{4}\sum_{b=0}^{4-a} c_{ab}g_1^a g_2^b g_3^{4-a-b}, \tag{4.4}$$

where c_{ab} denote the unique tensor coefficients and g_1, g_2, and g_3 are the components of the gradient direction $\mathbf{g}$.

Substituting F into the integral (5.1), we have a sum of integrals, each related to a different monomial:

$$S(\mathbf{g},b) = \sum_{a=0}^{4}\sum_{b=0}^{4-a} c_{ab}\int_{\mathbf{v}\in S^2} v_1^a v_2^b v_3^{4-a-b}K(\mathbf{g},\mathbf{v},b)d\mathbf{v}. \tag{4.5}$$

Solving these integrals analytically is intractable; hence, we approximate each one of them according to the centroid rule for integration of functions on the sphere [9]. Given a sphere triangulation with N faces, for a spherical function, $f(\mathbf{v})$, the centroid rule is given by

$$\int_{S^2} f(\mathbf{v})d\mathbf{v} \approx \sum_{i=1}^{N} f(\mathbf{v}_i)A(\Delta_i) \tag{4.6}$$

where $\mathbf{v}_i$ is the centroid of the i'th face and $A(\Delta_i)$ is the area of the face. This scheme is very accurate for specific sphere triangulations. Here we choose the third-order icosahedron

triangulation which results in 1280 faces (642 nodes). The evaluation of each integral according to this scheme is very fast as the centroids and the areas of the faces are computed only once.

Following these calculations, we can define a matrix, C, whose entries correspond to the numerical approximation of Eq. (4.6) for each monomial, in each direction $\mathbf{g}_i$. The size of this matrix is then $n \times m$ where n is the number of gradient directions and m is the number of unique tensor coefficients.

The linear constraints that impose the positivity on F are defined by using a $n \times m$ matrix A. Each row of A corresponds to a different gradient direction, and each column corresponds to a different monomial. The multiplication $\mathrm{A}\mathbf{x}$ results in a n-dimensional vector, and each element of it corresponds to $F(\mathbf{g}_i)$, where F is defined by Eq. (4.4). Thus, we obtain a set of n linear constraints, and each constraint is applied to a different gradient direction.

Finally, with respect to the matrices defined above, for each voxel, we solve the following linear programming problem:

$$\begin{aligned} &\arg\min_{\mathbf{x}} \frac{1}{2} \|\mathbf{S} - \mathrm{C} \cdot \mathbf{x}\|^2 \\ &\text{subject to} \quad -\mathrm{A}\mathbf{x} \leq \mathbf{b}, \end{aligned} \tag{4.7}$$

where $\mathbf{S}$ is a vector of the n DW measurements, and $\mathbf{b}$ is a n-dimensional vector which defines the boundary of the convex polytope on which we minimize the objective function. Setting the values of $\mathbf{b}$ to be zero results in estimation of a positive-semidefinite ODF.

To solve this problem, the number of gradient directions has to be larger than the number of the tensor coefficients. Since, typically, in HARDI scans $n > 60$, this condition holds as a fourth-order homogeneous polynomial defined by $m = 15$ unique coefficients. This problem may be solved efficiently using the MatLab optimization toolbox or through open source packages for convex optimization such as CVX [63]. Given the optimal vector of coefficients, $\mathbf{x}^\star$, the ODF is computed by $F = \mathrm{A}\mathbf{x}^\star$. The unique tensor coefficients are then arranged in a fourth-order tensor using the symmetry and the appropriate monomial factors.

Once the ODF has been estimated, we proceed to extracting the fiber directions and fractions. As an ODF is associated with a finite-order expansion of spherical harmonics, its maxima has a finite width. Thus, the ODF's maxima interfere and do not correspond to the correct fiber directions below a certain separation angle. In the following section, we solve this problem by using a rank-k tensor decomposition known as the CP decomposition. We show that while a rank-1 decomposition corresponds to finding the maxima of F, a

decomposition with $k > 1$ corresponds to finding the different components (fibers) that contribute to F which, in turn, significantly increases the ability to separate crossing fibers.

4.3 High-Order Tensor Decompositions

To discuss HOT decompositions, we have to first define the notion of a *tensor rank*. Tensor rank, denoted here as $R = \text{rank}(\mathcal{D})$, is defined as the minimal number of terms such that the following equality holds

$$\mathcal{D} = \sum_{r=1}^{R} \mathbf{v}_r^1 \otimes \mathbf{v}_r^2 \otimes \cdots \otimes \mathbf{v}_r^n, \tag{4.8}$$

where $\mathbf{v}$ are first-order tensors (vectors). The *order* of the tensor, n, is defined by the number of its indices and it determines the number of tensor products in Eq. (4.8). A *cubic* tensor is a tensor whose different modes have the same size, i.e., $\mathcal{D} \in \mathbb{R}^{d \times d \times \cdots \times d}$. The decompositions that we discuss in this section hold for a general n'th-order tensor which is not necessarily cubic or symmetric. In our case, $\mathcal{D}$ is cubic and symmetric where $n = 4$ and $d = 3$.

Unlike the matrix case ($n = 2$), the rank of a given HOT is not known. In fact, the problem of determining the rank of a given tensor is NP-complete [71]. However, in this work, we are interested in low-rank tensor approximation. For a given tensor rank $k < R$, the low-rank approximation is defined by:

$$\mathcal{D} \approx \sum_{r=1}^{k} \lambda_r (\mathbf{v}_r^1 \otimes \mathbf{v}_r^2 \otimes \cdots \otimes \mathbf{v}_r^n), \tag{4.9}$$

where $||\mathbf{v}_r|| = 1$, and for a symmetric tensor, $\mathbf{v}_r^1 = \mathbf{v}_r^2 = \cdots = \mathbf{v}_r^n$. A low-rank tensor approximation is known as rank-k decomposition and it is applied to various branches of science and engineering. It is also known in the mathematical literature as the CANDECOMP\PARAFAC (CP) decomposition [89]. The vectors $\mathbf{v}_r$ represent here the fiber directions, and the fiber weights are simply $w_r = \lambda_r / \sum_{r=1}^{k} \lambda_r$. The rank of the tensor corresponds here to the number of crossing fibers within a voxel. Since we do not expect to detect reliably more than two crossing fibers using a fourth-order tensor, we restrict ourselves to the $k = 2$ case.

The fiber model is determined in this work according to the ratio between the singular eigenvalues, λ_r. That is, the weakest fiber term is rejected whenever $\lambda_{\text{strong}}/\lambda_{\text{weak}} > t$, where the threshold was set to $t = 4$. An alternative model selection approach is the core consistency diagnostic (CORCONDIA) [30]. However, it is not within the scope of this chapter.

To compute the CP decomposition for a given tensor, $\mathcal{D}$, and a given rank, k, one has to solve the least squares problem

$$\min_{\tilde{\mathcal{D}}} ||\mathcal{D} - \tilde{\mathcal{D}}||^2 \tag{4.10}$$

where $\tilde{\mathcal{D}} = \sum_{r=1}^{k} \lambda_r (\mathbf{v}_r^1 \otimes \mathbf{v}_r^2 \otimes \cdots \otimes \mathbf{v}_r^n)$. Due to its simplicity and efficiency, the most popular technique to compute a rank-k tensor approximation is the Alternating Least Squares (ALS) [37, 92]. The principal of the ALS is straightforward. In each iteration, it solves a least squares problem for the set of vectors $\{\mathbf{v}_r^i\}_{r=1}^k$, $i = m$, while keeping the vectors with $i \neq m$ fixed.

A particular case with $k = 1$ is the *rank-1* decomposition. Given a symmetric tensor $\mathcal{D}$, its best rank-1 approximation is computed by solving the problem (4.10) where $\tilde{\mathcal{D}} = \lambda \underbrace{\mathbf{v} \otimes \mathbf{v} \otimes \cdots \otimes \mathbf{v}}_{n \text{ times}}$. This problem is equivalent to the nonlinear optimization problem [96]

$$\begin{aligned} &\max_{\mathbf{v}} |D(\mathbf{v})| \\ &\text{subject to} \quad ||\mathbf{v}|| = 1, \end{aligned} \tag{4.11}$$

where $D(\mathbf{v})$ is the homogeneous polynomial induced by the tensor and identified here with the ODF. The best rank-1 decomposition for symmetric tensors can be efficiently computed by solving the ALS for $k = 1$ or by using a high-order power method (HOPM) (e.g., [93]). This problem may have multiple nonantipodal solutions and the different solutions are found by multiple initializations. Upon converges, for each initialization, the algorithm produces an eigenpair ($\mathbf{v}_i$,λ_i). For each eigenpair, the unit-norm vector $\mathbf{v}_i$ specifies a global maximum location where $\lambda_i = D(\mathbf{v}_i)$. As in our case, $D(\mathbf{v})$ corresponds to the ODF; *as long as the maxima are distinguished*, the resulting vectors will point in the directions of the underlying fibers. As we will show in the next section, at these cases as well, the CP decomposition is superior to maxima finding.

4.4 Experiments

4.4.1 Synthetic Data Simulations

To assess the accuracy of our new algorithm, we applied it to synthetic as well as measured experimental HARDI data. First, we generated synthetic data by simulating two crossing fibers according to the multicompartment model

$$S(\mathbf{g}, b) = S_0 \sum_{i=1}^{k=2} w_i e^{-b\mathbf{g}\mathrm{D}_i\mathbf{g}^T} \tag{4.12}$$

For both tensors, we assume a prolate tensor model with eigenvalues $\lambda_1 = 1.7 \cdot 10^{-3}\mathrm{mm}^2/\mathrm{s}$, $\lambda_2 = \lambda_3 = 3 \cdot 10^{-4}\mathrm{mm}^2/\mathrm{s}$ and a b-value of 1500 $\mathrm{s/mm}^2$. The baseline signal was set to

$S_0 = 1$. One fiber direction was created randomly and the second one was obtained by rotating the corresponding tensor to get the desired separation angle between the fibers. The weights were set equally. For the convolution kernel, we have used Eq. (4.2) with a concentration parameter of $c = 200$.

The algorithm was tested on noisy data at three levels of SNR_0[1]: 50, 25, and 12.5, where the signal was corrupted by Rician distributed noise. For each noise level, the separation angle was varied from 30 to 90 in 5 degree steps. The signal was measured using 81 gradient directions which were computed using a second-order icosahedron sphere tessellation. For each separation angle and noise level, we performed 100 experiments where fourth-order tensors were estimated using the linear programming approach and a rank-2 decomposition was applied to extract the fiber directions and fractions. The mean and the standard deviation of the separation angle, the fiber direction deviation, and the weights estimation were calculated for each case.

The CP decompositions were performed using the ALS algorithm [37]. Although the ALS algorithm produces nonsymmetric intermediate results for symmetric tensors, we have found that eventually it converges to a symmetric tensor solution. We have implemented a symmetric version of the ALS according to [37]. Although it produces symmetric intermediate solutions, it has not obtained more accurate solutions than the nonsymmetric version. For a MatLab implementation of the ALS [2], it takes 20ms on a Linux workstation with a 2.4MHz quad core CPU and 6GB to produce a rank-2 decomposition for a given tensor.

There are only rare cases where the ALS will not converge to a stationary point. However, it may converge to local minima. While local minima solutions cannot be entirely avoided, we have found that they can be adequately treated by initializing the ALS using the singular eigenvectors of the unfolded tensor [96]. Random initialization gave less accurate results as the algorithm produced local minima solutions more often, especially in low SNR simulations and for small separation angles.

In Fig. 4.1, we present the minimal fiber direction deviations of the estimated directions from the true directions, as well as the separation angle deviations. For SNR ratios of 50 and 25, it is shown that the algorithm can reliably resolve the fiber directions, especially above a separation angle of 35 degrees. When the SNR drops down to 12.5, which is a value found in real scans, below an angle of 45 degrees, we observed large biases and

[1]Measured as the baseline signal, S_0, divided by the noise standard deviation, σ.

[2]Available at: http://csmr.ca.sandia.gov/~tgkolda/TensorToolbox/

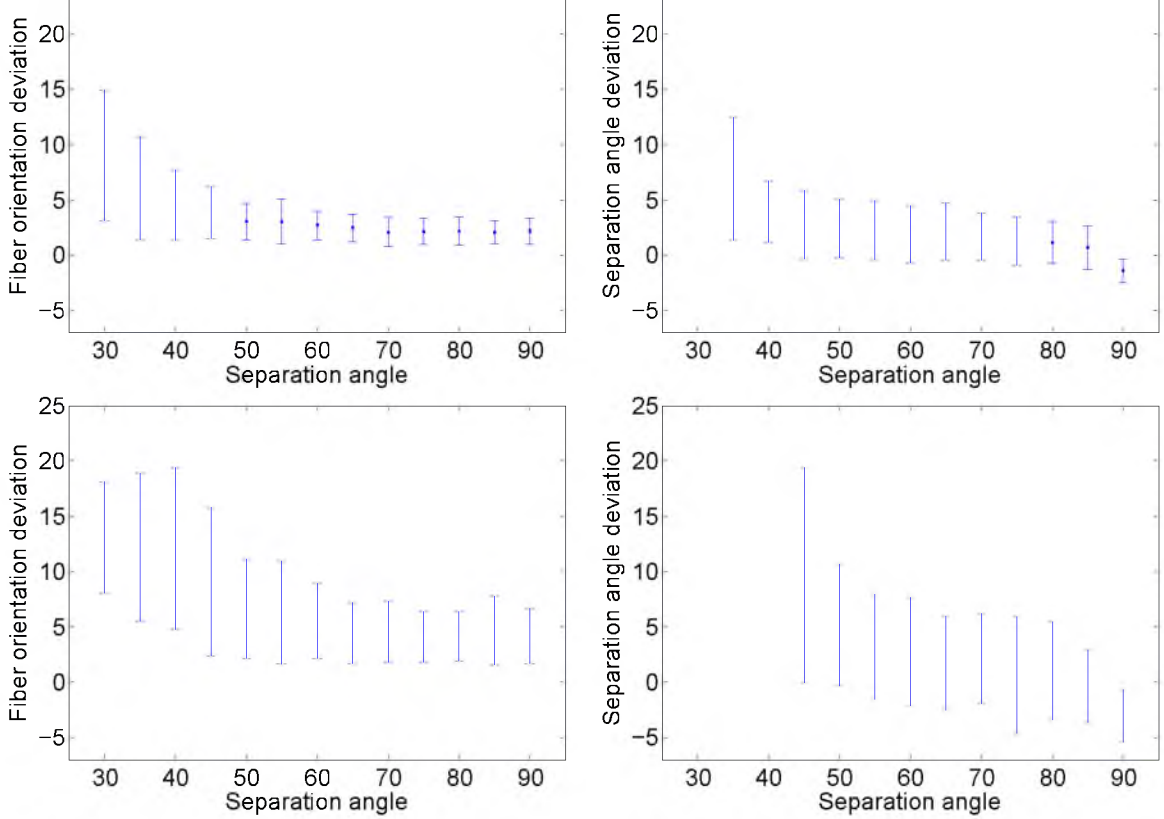

Figure 4.1: The minimal fiber direction deviation (left) and separation angle deviation (right). The SNR decreases from top to bottom.

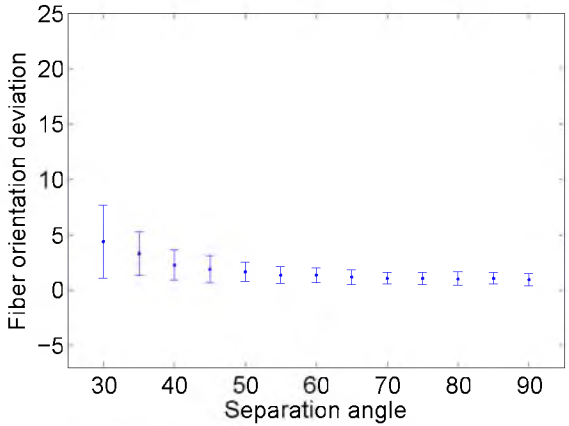
Fiber orientation deviation
Separation angle
25
20
15
10
5
0
−5
30
40
50
60
70
80
90

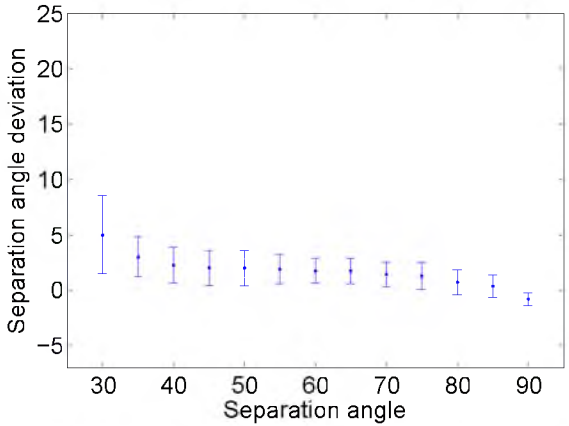
Separation angle deviation
Separation angle
25
20
15
10
5
0
−5
30
40
50
60
70
80
90

high standard deviations at one fiber direction. Hence, the separation angle deviation is not shown for these cases. The performance of the algorithm in this SNR level improves significantly above a separation angle of 50 degrees where both fiber directions could be resolved reliably. As shown in Fig. 4.2, the fiber fractions could be estimated accurately above 45 degrees for SNR levels of 50 and 25, whereas at the lowest SNR level, 60 degrees is the point where the accuracy improves significantly. In Fig. 4.3, we show that the rank-2 CP decomposition has an advantage over maxima finding even at large separation angles where the ODF has distinct maxima. While at a fiber separation angle of 80 degrees, the rank-2 decomposition has a slight advantage only at low SNR levels (top left image), at 70 degrees, it outperforms the rank-1 decomposition at all noise levels (top right image). Below 70 degrees, the maxima merge and maxima finding is no more reliable. In the bottom images, ODFs that represents crossing fibers at 30, 45, and 90 degrees are presented. In these cases, the correct fiber orientations can be estimated by using the rank-2 decomposition only. Maxima directions in this experiment were calculated using the SS-HOPM algorithm [93].

4.4.2 Phantom Data

To test our algorithm on experimentally obtained HARDI data where the ground truth fibers are known, we first apply our decomposition algorithm to the publicly available phantom data used in the MICCAI 2009 Fiber Cup contest [121]. The data were scanned at three b-values: 650,1500, and 2650 s/mm^2. We used the dataset with a b-value of 2650s/mm^2 in this study. The top row of Fig. 4.4 shows the reconstructed fourth-order tensor field, the rank-1 decomposition, and the rank-2 decomposition results. The two right-hand side images in this row illustrate the comparison between the rank-1 and the rank-2 decomposition where the differences between the decompositions are highlighted by ellipses. The fiber directions are presented as thin cylinders at each voxel, where the length of the cylinder is determined by the fiber weight. We have integrated the ground truth fibers as a reference.

As shown, the decomposed directions clearly delineate the hidden fiber orientations. However, by using the rank-2 decomposition, our algorithm could detect more crossing fibers which are oriented along the ground truth fibers.

4.4.3 Cat Brain Data

To test the algorithm on real data, we used a HARDI scan of a cat brain. The data were acquired using a standard 3D diffusion-weighted spin-echo sequence with TR=500 ms, TE=39.8 ms, field of view $70 \times 40 \times 32$mm, matrix size $175 \times 100 \times 80$, zero padded

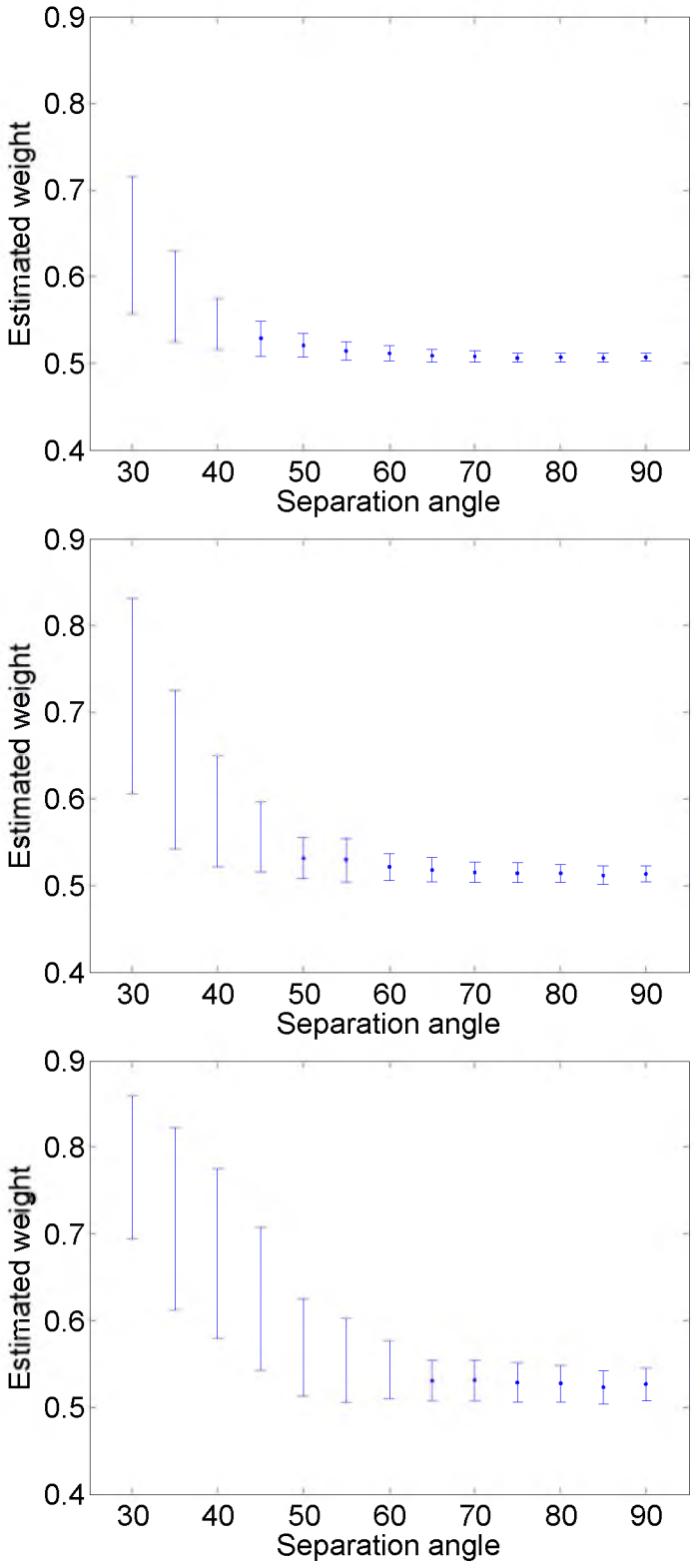

Figure 4.2: The estimation of fiber fraction for one fiber using the rank-2 decomposition. The SNR ratio decreases from 50 to 12.5, from top to bottom.

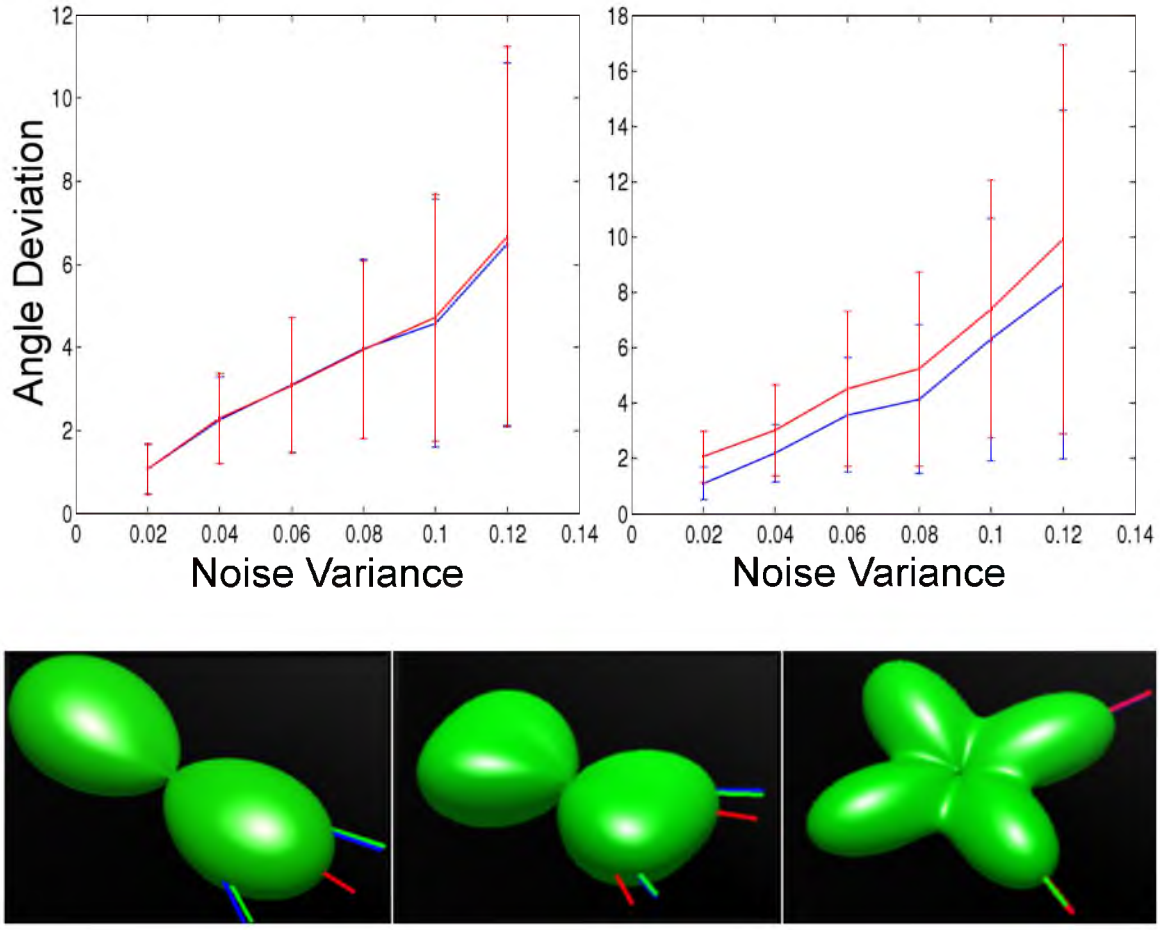

Figure 4.3: Rank-2 decomposition vs. maxima finding with rank-1 decomposition. These results present the minimal fiber direction deviation for a separation angle of 80 degrees (top left) and 70 degrees (top right). The red curve is for the maxima finding, and the blue curve is for the rank-1 decomposition. The bottom images demonstrate the differences between the approaches when the separation angle is 30 deg(bottom left), 45 deg (bottom middle), 90 deg (bottom right). The green and the blue lines show the true and the estimated fiber directions, respectively. The red line shows the direction of the maximum obtained by a rank-1 tensor decomposition. The mean and the standard deviation were calculated from 100 experiments for each noise level.

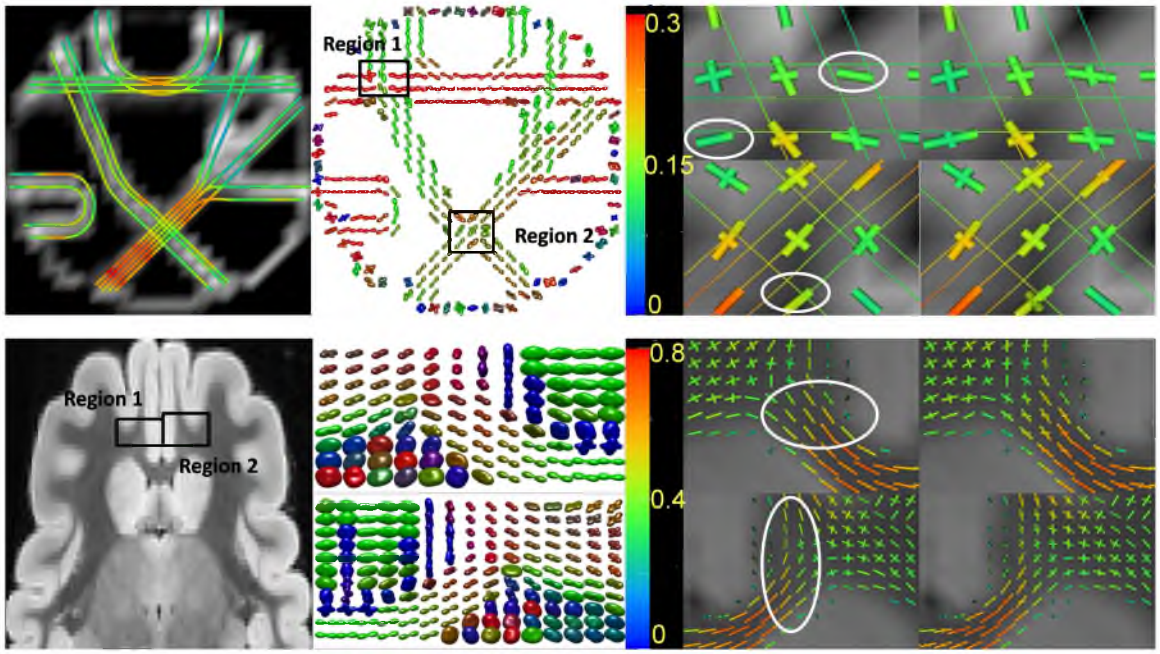

Figure 4.4: The decomposition results of the ODF field of the phantom (top row) and cat brain (bottom row) show the following: b0 image (left), fourth-order tensor field of region 1 and region 2 (middle left), rank-1 decomposition (right middle), and rank-2 decomposition (right). The results of region 1 are presented at the top and the results of region 2 are at the bottom. For the phantom, the ground truth fibers are shown both in the b0 image and in the detailed views of the decomposition results.

to $200 \times 100 \times 80$, yielding an isotropic resolution of 400 microns and a b-value of 6000 s/mm^2. Four images without diffusion weighting (b0 image) and 96 diffusion-weighted images were acquired. The diffusion gradients were uniformly spaced over a unit sphere. The two left images of the bottom row in Fig. 4.4 show the b0 image and the reconstructed fourth-order tensor field for the two specified ROIs. The two right images in this row compare between maxima finding method, with the rank-1 decomposition and the rank-2 decomposition. These results show that some of the crossing fibers, which are not detectable using maxima finding, could be detected using the rank-2 decomposition. Although further validation needs to be done on more datasets, promising results are already demonstrated qualitatively on cat brain data.

4.5 Conclusions

In this chapter, we propose a novel framework that combines an ODF estimation method with a parameter extraction technique for estimation of fiber directions and fiber fractions. For the estimation method, we have used a specific form of spherical deconvolution where the ODF is represented by a homogeneous polynomial induced by a high-order tensor. The ODF was constrained to be non-negative by adding a set of linear constraints to the objective function that represents the spherical deconvolution. Then, we show that fiber directions and fiber fractions are accurately extracted by applying a rank-2 CP decomposition to the ODF. As the ODF in this case is associated with a higher-order tensor, we can apply the decomposition directly to the tensor without using the conversion step which was necessary in [135]. The CP decomposition optimizes the *sum* of the different rank-1 terms and no tensor subtractions are being used. Consequently, the problems of rank increasing and nonpositive residuals do not exist here.

Experiments performed on synthetic data, phantom, and real data show that this method can resolve two crossing fibers reliably, even at low SNR, and at far better resolution than the maxima detection approach.

As future work, we plan to make the algorithm more efficient, accurate, and more robust to noise both at the spherical deconvolution and the tensor decomposition levels. Tensors of order greater than four will be considered as well.

CHAPTER 5

A DIRECT APPROACH FOR WHITE MATTER STRUCTURE ASSESSMENT USING LOW-RANK POLYNOMIAL APPROXIMATIONS

This chapter presents a novel approach to extract white matter fiber orientations and volume fractions *directly* from diffusion-weighted imaging (DWI) measurements. It is based on a spherical deconvolution technique and decomposition of a homogeneous polynomial into a sum of powers of linear forms, known as a *symmetric tensor decomposition*. The fiber-ODF (fODF), which is described by a homogeneous polynomial, is approximated here by a discrete sum of even-order linear forms that represents single fibers. This polynomial approximation is convolved to a single fiber response function, and the result is optimized against the DWI measurements to assess the fiber parameters. This formulation leads to a nonlinear optimization problem that we solve here by means of an iterative alternating scheme, which is based on the Levenberg-Marquart technique. Using synthetic data simulations, we show that the proposed algorithm is more accurate and stable compared to the state-of-the-art. In addition, we apply this method to *in vivo*, human brain data and show that it successfully recovers complex fiber structures.

5.1 Introduction

In contrast to diffusion tensor imaging (DTI), High Angular Resolution Diffusion Imaging (HARDI) is an imaging technique that is capable of describing more complex white matter structures such as crossing fibers. Given HARDI data, various reconstruction techniques are used to infer the fiber structures (e.g., [44, 142, 150, 113]). These techniques are primarily based on the reconstruction of an orientation distribution function (ODF) that describes the dominant diffusion directions. To recover the white matter fiber pathways, the dominant diffusion directions are extracted from the ODF. Since white matter connectivity

maps are obtained from tracking these dominant directions, an accurate reconstruction of this information is crucial. This motivated the development of various analytical and numerical techniques to achieve this task. These techniques are mainly based on polynomial root-finding and higher-order ODF tessellation [2, 26, 59], or low-rank tensor approximations [78, 135]. However, the accuracy of these algorithms is limited by the ODF quality of reconstruction and its reconstruction order (i.e., the spherical harmonics truncation order). Also, since these algorithms introduce significant complexity, the complete process of ODF reconstruction, followed by orientations estimation, is inefficient. Thus, to combine these two optimization problems into one, and avoid the complexity of extracting the orientations from the ODF, we propose here a novel approach to reconstruct the fiber orientations and the volume fractions *directly* from the DWI measurements. Since an ODF describes only the angular part of the diffusion, we may eliminate its reconstruction and still allow it to recover the fiber pathways by directly obtaining the orientation information.

The proposed approach is motivated by the *symmetric tensor decomposition* [28]; that is, any homogeneous polynomial of order d may be decomposed into a sum of r distinct linear-forms of the same order. Since any ODF with antipodal symmetry may be represented as an even-order homogeneous polynomial (or a higher-order tensor) [43], it could be decomposed in a similar manner. Here, we consider a lower-rank polynomial approximation of a fODF in terms of even order linear-forms. In this approximation, each linear-form represents a single fiber and its coefficients correspond directly to the fiber orientation and the volume fraction. These coefficients are estimated via a spherical deconvolution operation [142] such that each term is convolved to a single-fiber response and the result is optimized against the HARDI measurements by means of l_2 norm. The resulting nonlinear optimization problem is solved here using an iterative alternating scheme based upon the Levenberg-Marquardt technique, and is shown to produce stable and accurate results.

In addition to the ability to estimate the orientations directly from the measurements, this approach has more advantages over the commonly used reconstruction techniques: 1) The fODF expansion in linear-forms is naturally positive-definite, and hence, no additional constraint that guarantees this property is required. 2) Higher-order polynomials generally lead to a better fiber separation resolution. However, they increase the number of model parameters above the number of measurements that are typically available. Thus, a reconstruction of a higher-order polynomial requires a nonlinear constrained reconstruction technique, which involves additional heuristic parameters [142]. Here, the number of model parameters is determined by the number of fibers only (three parameters per fiber) and not

by the polynomial order. Therefore, high accuracy can be achieved without increasing the number of model parameters and introducing additional parameters. Also, the order of the polynomial can be easily adjusted to obtain the best results.

5.2 Spherical Deconvolution via Symmetric Tensor Decomposition

Spherical deconvolution is a common technique to recover major diffusion directions from DWI data [142]. It is based on a convolution between a spherically symmetric function, known as fODF, and an axially symmetric kernel that represents a single fiber response. Given a vector of n DWI measurements in the gradient directions, the fODF, denoted by F, is reconstructed by solving the following deconvolution problem:

$$\min_{F} \frac{1}{2} \sum_{i=1}^{n} \left\| S(\mathbf{g}_i, b) - S_0 \int_{S^2} F(\mathbf{v}) K(\mathbf{g}_i, \mathbf{v}) d\mathbf{v} \right\|^2 . \tag{5.1}$$

This problem is solved for a fixed kernel, K, where its width is adjusted to the particular dataset. The resulting fODF represents a sum of spherical delta functions aligned with the fiber orientations and weighted by the volume fractions. This basic problem is solved by means of least squares where the fODF is reconstructed by a pseudo-inverse operation. However, additional constraints such as fODF positivity lead to a nonlinear optimization problem [142], which we discussed in Chapter 4.

In [28], it was shown that any homogeneous polynomial of order d may be decomposed into a sum of linear-forms of the same order such that:

$$F(x_1, x_2, \ldots, x_l) = \sum_{i=1}^{r} \lambda_i f_i^d \tag{5.2}$$

where $f_i = (\sum_{i=1}^{l} \alpha_i x_i)$, r is the polynomial *rank* and l is the polynomial *dimension*. This decomposition is known as *symmetric tensor decomposition* since homogeneous polynomials are directly related to symmetric tensors. An algorithm to decompose a general homogeneous polynomial was proposed in [28].

It is known that any spherical function with antipodal symmetry may be represented as an even-order homogeneous polynomial, where its order is equivalent to the truncation order of the corresponding spherical harmonics expansion [43]. Since an fODF may be represented as a homogeneous polynomial, one may use [28] to compute its full-rank decomposition. However, a full-rank fODF encodes information on white matter fibers, as well as noise. Thus, it was proposed in [78, 135] to recover the fiber orientations via a lower-rank tensor approximation. This approximation was applied to the fODF and required its estimation first.

To combine the fODF reconstruction and the orientations estimation into one optimization problem, we first approximate the fODF using an equivalent lower-rank approximation by means of polynomial approximation (symmetric tensor decomposition) such that:

$$F(\mathbf{v}) \sim \sum_{i=1}^{\tilde{r}} \gamma_i f_i^d = \sum_{i=1}^{\tilde{r}} (\boldsymbol{\alpha}_i \cdot \mathbf{v})^d, \quad \tilde{r} < r, \tag{5.3}$$

where $\boldsymbol{\alpha}_i \in \mathbb{R}^3$, $\mathbf{v} \in S^2$ and each fiber aligned in direction $\boldsymbol{\alpha}_i$ is identified with a linear form $(\boldsymbol{\alpha}_i \cdot \mathbf{v})^d$. The number of fibers to be estimated is determined by the approximation rank $\tilde{r}$ and the expansion coefficients are defined as $\gamma_i = \|\boldsymbol{\alpha}_i\|^d$.

Next, we substitute (5.3) into (5.1). This leads to the following nonlinear optimization problem:

$$\min_{\boldsymbol{\alpha}_j} \frac{1}{2} \sum_{i=1}^{n} \left\| S(\mathbf{g}_i, b) - S_0 \int_{S^2} \sum_{j=1}^{\tilde{r}} (\boldsymbol{\alpha}_j \cdot \mathbf{v})^d K(\mathbf{g}_i, \mathbf{v}) d\mathbf{v} \right\|^2. \tag{5.4}$$

This problem is solved for the coefficients of the linear forms, three coefficients for each fiber, which are directly estimated from the DWI measurements. The fiber orientations and the volume fractions are derived as follows: Since each linear-form gets its maximum at the direction specified by $\boldsymbol{\alpha}_j$, given the optimal solution, $\tilde{\boldsymbol{\alpha}}_j$, the corresponding fiber orientation is simply $\mathbf{u}_j = \frac{\tilde{\boldsymbol{\alpha}}_j}{\|\tilde{\boldsymbol{\alpha}}_j\|}$. As we do not impose the constraint $\sum_{j=1}^{\tilde{r}} \|\boldsymbol{\alpha}_j\|^d = 1$, the corresponding volume fraction is given by $w_j = \frac{\|\tilde{\boldsymbol{\alpha}}_j\|^d}{\sum_{j=1}^{\tilde{r}} \|\tilde{\boldsymbol{\alpha}}_j\|^d}$.

5.3 Rank Selection Criterion

To determine the number of fibers for each voxel, i.e., the rank/model selection problem, we first provide a brief review. Alexander et al. [4] use the ANOVA F-test based on spherical harmonic representation of the ADC profile for several truncation orders to classify the diffusion data. The ANOVA F-test was used to test whether increasing the order of spherical harmonic will significantly change the fitting. Several thresholds of the trunction error were given before running the algorithm by controlling the volume ratio of the non-Gaussian voxels, which should vary for different noise level, b-value, and spacial resolution, etc. In addition, it was shown in [136] that the F-test tends to underestimate the correct number of fibers comparing to weight-based thresholding. Frank et al. [54] used a fourth-order spherical harmonic series to approximate the ADC profile and defined fractional multifiber index (FMI), which is the high-order versus lower-order ratio of the spherical harmonic coefficients, to classify the non-Gaussian profiles. Recently, Support Vector Machine (SVM), based on rotational invariant measures of HARDI data, were introduced to classify HARDI *in vivo* data by Schnell et al. [133]. Six classes of image components are determined: grey

matter, parallel neuronal fiber bundles in white matter, crossing neuronal fiber bundles in white matter, partial volume between white and grey matter, background noise, and cerebrospinal fluid. These invariant measures of HARDI data used in this study are the sum of the spherical harmonic coefficients per order at each voxel, while Frank et al. [54] use the higher-order versus lower-order ratio of the spherical harmonic coefficients. Although these classification methods based on rotational invariants produce somewhat promising results, they suffer one common problem which is two tensor shapes that have completely different shape may have exactly the same rotational invariant. As shown in Figure 5.1, these three fODFs have exactly the same rotation invariants but completely different configurations. The left column shows that the simulation of fODF contains one dominate fiber direction, while the middle and right column shows that the simulation of fODF contains two dominate fibers, crossing at 60 degrees and 90 degrees, correspondingly. Based on the vector of rotational invariants, there is no way to classify whether there is only one fiber or two fibers. Behrens et al. [19] use automatic relevance determination in a Bayesian modeling framework to help with fiber tracking in a multi-orientation field. It aims at Bayesian model averaging rather than at making a hard decision about the model type. Freidlin et al. [55] apply the Bayesian Information Criterion (BIC) to diffusion model selection. However, it exhibited a strong bias towards selecting two fibers according to Schultz et al. [136].

As we will discuss in Chapter 6, a fourth-order tensor is a fifteen-dimensional object, where the scalar measures or peak weights are the low-dimensional projections. In order to acquire accurate classification results, all of this aforementioned multidimensional information need to explored fully. Similar ideas were adopted by one recent study done by Prčkovska et al. [122]. However, they focused more on the fast classification and did not fully make use of all of the information in each dimension. Especially, they did not consider any neighborhood information, which may be crucial for improving the ROC curve of the model selection.

Since our method is not a full parametric technique, the full ODF and scalar measure

Figure 5.1: Three fODF shapes with exactly the same rotational invariant but with different number of fibers and different configuration: one-fiber simulation(left), two-fiber crossing at 60 degrees (middle), two-fiber crossing at 90 degrees (right).

information are not available. We select the optimal rank, $\tilde{r}$, based on a threshold. That is, we estimate the orientations for a fixed rank (generally, $\tilde{r} <= 3$) and eliminate solutions based on the estimated volume fractions. A solution will be accepted if its volume fraction is above a certain threshold where we learn the threshold directly from the data, as described in the next section.

5.4 Numerical Optimization

To solve this nonlinear optimization problem (5.4), we adopt the Levenberg-Marquardt (LM) technique. When $\tilde{r} = 1$, the three coefficients can be estimated accurately using a straightforward implementation of the LM. However, when $r > 1$, more coefficients are involved and estimating them at once provides poor results. To deal with the multifiber estimation case, we suggest an iterative alternating LM scheme. In this scheme, a complete update step is composed of $\tilde{r}$ LM substeps. In each substep, only the coefficient associated with a single fiber are updated while the other coefficients are kept fixed, as described in Algorithm 1. In each iteration, one has to convolve the fiber estimate to the kernel. This operation is performed using a discrete spherical integration scheme [9]. As an initial guess, we use random orthonormal vectors.

5.5 Experiments

5.5.1 Synthetic Data

To assess the accuracy of the algorithm, we simulated two crossing fibers at various separation angles, equal volume fractions and two b-values. The signal was simulated according to the multitensor model (Eq. 4.12) where for each compartment, we assumed a

Algorithm 1 Alternating LM for $\tilde{r} = 2$

Let I be the objective function defined in 5.4, and let $J_k = \frac{\partial I}{\partial \boldsymbol{\alpha}_k}$, $k = 1, 2..$
Set $t = 0$.
Initialize $\boldsymbol{\alpha}_k^t$, $k = 1, 2$.
Compute $\boldsymbol{\alpha}_1^{t+1}$ using an LM update with respect to $J_1(\boldsymbol{\alpha}_1^t, \boldsymbol{\alpha}_2^t)$ and a damping parameter ϵ_1.
Compute $\boldsymbol{\alpha}_2^{t+1}$ using an LM update with respect to $J_2(\boldsymbol{\alpha}_1^{t+1}, \boldsymbol{\alpha}_2^t)$ and a damping parameter ϵ_2.
if converged **then**
    return $\boldsymbol{\alpha}_{1,2}^t$
else
    $t \leftarrow t + 1$
    goto 4
end if

prolate tensor model with FA=0.8. The b-values were set to $1500s\backslash mm^2$ and $3000s\backslash mm^2$, and 64 gradient directions were used. Each dataset was generated in two baseline SNR levels: 40 and 20, where the clean data were corrupted by Rician noise distribution as follows:

$$S_{\text{noisy}}(\mathbf{g}_i, b) = \sqrt{(S(\mathbf{g}_i, b) + n_1)^2 + n_2^2} \tag{5.5}$$

where $n_1,\ n_2 \sim \mathcal{N}(0, \sigma^2)$, and $\sigma = \frac{S_0}{\text{SNR}}$. For each SNR level, we generated 200 noise realizations of the signal and estimated the fiber orientations using the low-rank polynomial approximation (LRPA), constrained spherical deconvolution (CSD), and analytical Q-ball imaging (QBI). The polynomial order is set to $d = 12$, as this value gives an optimal trade-off between the ability to resolve low separation angles and noise sensitivity [142]. The single-fiber response kernel is described here by the Watson function $K(\mathbf{g}_i, \mathbf{v}, \delta) = \exp\left(-\delta(\mathbf{g}_i^T \cdot \mathbf{v})^2\right)$ where δ is a function of the b-value and the principal diffusivity, $\mathbf{g}_i$ is the gradient direction, and $\mathbf{v}$ is the integration parameter.

We compared our method to the CSD technique that was shown to be more accurate and robust to noise compared to other HARDI reconstruction techniques. For the CSD reconstruction, we have used the authors' implementation with the recommended settings. To allow the reconstruction of a twelfth-order fODF, the signal was super-resolved from 64 to 321 directions. For LRPA, no super-resolution was applied and the original 64 directions were used. The algorithms are compared based on the mean orientation deviation at different separation angles (30 to 90), and two SNRs (40 and 20). The mean deviation is computed by averaging the deviations of the estimated orientations from the simulated ones, and is given in degrees. In addition, we compared our method to standard fourth-order ODF, which was reconstructed using analytical QBI [44] and sharpened using Laplace-Beltrami sharpening with parameter $\lambda = 0.2$.

The results depicted in Fig. 5.2 show that the LRPA performs well at high as well as low SNR and provide more accurate and stable results compared to CSD and analytical QBI, especially at b=$3000s\backslash mm^2$. The measured running time for a Matlab implementation of the LRPA was on average 50ms per voxel. This was measured on a standard laptop with 2.4Ghz Intel Core i5 CPU and 4GM RAM. The tested implementation is nonoptimal and its efficiency may be increased significantly by using high-level programming language. Similar running times were measured for CSD and QBI (Matlab implementations), but for the ODF reconstruction step only.

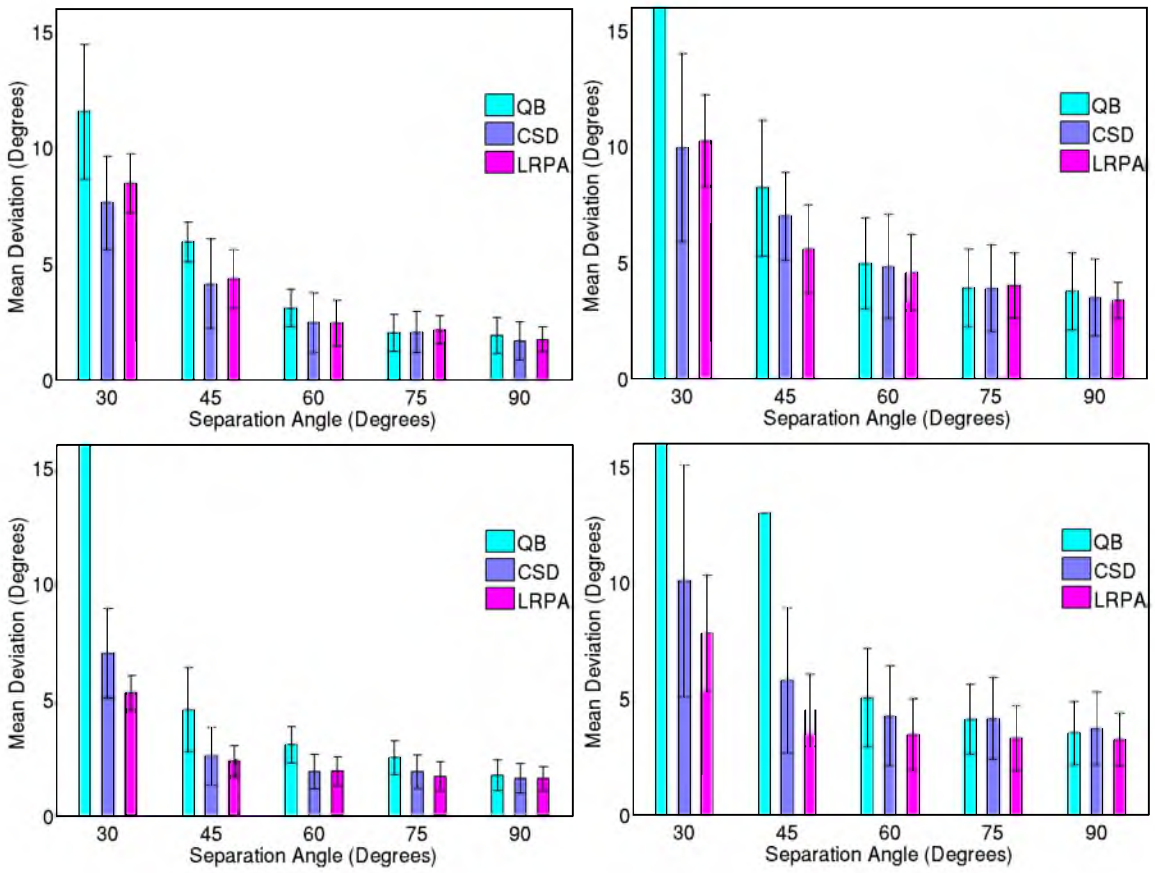

Figure 5.2: Simulated data comparisons between Q-ball, CSD, and LRPA. Two b-values are compared: $1500s\backslash mm^2$ (top) and $3000s\backslash mm^2$ (bottom). The SNRs are 40 (left figures) and 20 (right figures). When the standard deviation exceeds the axis limit, we present the mean only.

5.5.2 Human Brain Data

The human brain data were acquired on a 3T Siemens Tim Trio scanner using a single-shot spin-echo EPI sequence and a b-value of 2000 s/mm^2. One B0 image and 64 diffusion-weighted images in a resolution of $106 \times 106 \times 76$ and a voxel size of $2 \times 2 \times 2$mm^3 were acquired. The measured baseline SNR for these data was approximately 20. A white matter mask was registered to the data and the kernel width, δ, was estimated by computing the mean principal diffusivity of all white matter voxels with FA > 0.7. Furthermore, we use these voxels to estimate the rank-selection threshold. As most of these voxels lie in single tract regions, such as the corpus callosum, they presumably consist of single fibers. Thus, by applying a rank-two polynomial approximation to these voxels, the lowest weight term is likely to describe noise rather than a fiber. Indeed, the results show a high ratio between the weights of the first and the second term in these voxels. The threshold was then set as the average of the lowest weights where we measured a value of 0.21. Thus, fibers with a volume fraction less than 25% of the dominant volume fraction are considered as noise and eliminated. To test the algorithm, we have chosen the brain region in the centrum semiovale region with a crossing pattern (Fig. 5.3). The results show that along the single tracts, mostly one-fiber model was selected, whereas in the center of the ROI, where the different tracts cross, two- and three-fiber patterns were selected. The fiber orientations were estimated using a twelfth-order polynomial and were compared to CSD

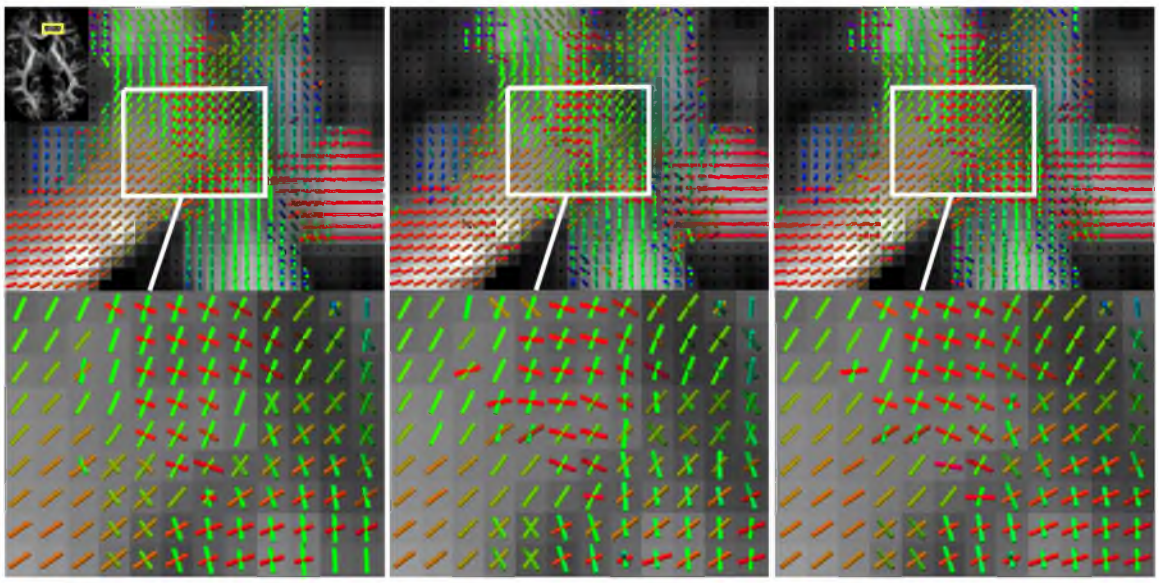

Figure 5.3: Axial slice showing reconstruction results of a crossing fibers region in human brain. From left to right: QBI, CSD, and LRPA reconstruction methods. The FA values are shown in the background.

with a reconstruction order of 12 and QBI with a reconstruction order of 4. All methods show very similar orientations and separation angles at the crossings region. However, the CSD reconstruction results show some noise sensitivity which results in less structured fiber orientations. This suggests that the reconstruction order for this method might be too high for this noise level and has to be reduced.

5.6 Conclusions

We presented a novel technique to recover white matter fiber orientations and volume fractions. This technique avoids the complexity of extracting the orientations from the ODF by directly estimating this information from the DWI data. It relies on a low-rank homogeneous polynomial approximation by means of powers of linear-forms representing single fibers. An l_2 optimization problem based on a spherical deconvolution technique is used to estimate the fiber orientations and the volume fractions. To solve this problem, an iterative alternating Levenberg-Marquardt scheme is introduced. The results presented here show that this algorithm performs well on synthetic and *in vivo*, human brain data and outperforms the state-of-the-art in terms of accuracy and stability.

Without the time-consuming ODF reconstruction process, our algorithm may be especially useful for improving the speed and the accuracy level of fiber tracking algorithms. Since the number of model parameters is determined by the number of fibers only (three parameters per fiber) and not by the polynomial order, this algorithm may potentially be useful for reducing the number of gradient directions needed by other HARDI techniques.

CHAPTER 6

UNCERTAINTY VISUALIZATION IN HARDI BASED ON ENSEMBLES OF ODFS

In this chapter, we propose a new and accurate technique for uncertainty analysis and uncertainty visualization based on fiber orientation distribution function (ODF) glyphs, associated with high angular resolution diffusion imaging (HARDI). Our visualization applies volume rendering techniques to an ensemble of 3D ODF glyphs, which we call *SIP functions* of *diffusion shapes*, to capture their variability due to underlying uncertainty. This rendering elucidates the complex heteroscedastic structural variation in these shapes. Furthermore, we quantify the extent of this variation by measuring the fraction of the volume of these shapes, which is consistent across all noise levels, the *certain volume ratio*. Our uncertainty analysis and visualization framework is then applied to synthetic data, as well as to HARDI human-brain data, to study the impact of various image acquisition parameters and background noise levels on the diffusion shapes.

6.1 Introduction

Diffusion-weighted magnetic resonance (DW-MR) is an imaging technique that enables one to measure diffusion priorities of water molecules in a fibrous tissue [13]. It is primarily used to reveal the white matter fibers structure of the brain, as well as structures of muscle fibers. Under the assumption of a Gaussian diffusion, the connection between the acquired DW signal and the diffusion rate is described by the Stejskal-Tanner equation:

$$S(\mathbf{g}, b) = S_0 e^{-b\mathbf{g}^T D\mathbf{g}} = S_0 e^{-bD(\mathbf{g})}, \tag{6.1}$$

where $S(\mathbf{g}, b)$ measures the signal decay in a direction $\mathbf{g}$ due to the application of a magnetic field gradient, and S_0 is the nonweighted diffusion signal (the signal measured in the presence of a constant magnetic field). Given a vector $\mathbf{S}$ of measurements in n gradient directions, an optimization problem is solved for $D(\mathbf{g})$, the diffusivity function. This problem is solved for

each brain voxel where $D(\mathbf{g})$ describes the apparent diffusion coefficient (ADC) in direction $\mathbf{g}$. The parameter b, which we denote here as *the sensing parameter*, is determined by the physical properties of the measurement (e.g., magnetic field strength, pulse duration).

In diffusion-tensor imaging (DTI), the diffusivity function is represented by a symmetric positive-definite second-order tensor known as the diffusion tensor (DT). Diffusion tensors can only model one dominant diffusion direction per voxel, and thus, are incapable of describing complex fiber structures. To overcome this limitation, new imaging techniques, which are known as high angular resolution diffusion imaging (HARDI), have emerged. There are various image reconstruction techniques associated with HARDI (e.g., [149, 143, 44]). In most of these reconstruction techniques, an orientation distribution function (ODF) is used to describe the diffusion profile. Unlike a DT, an ODF can have multiple maxima; thus, it can capture complex fiber structures such as crossing fibers.

The estimation accuracy of an ODF (or a DT) is influenced by a number of parameters such as the b-value, number of gradient directions, and signal-to-noise ratio. These different parameters introduce a level of uncertainty to the estimated diffusion profiles, and hence, uncertainty analysis and visualization become crucial to obtaining a better understanding of the fiber structure.

Over the last decade, various works have been devoted to the uncertainty study in the DTI model (e.g., [114, 81, 162]). However, only a handful of papers study the uncertainty in the ODFs associated with the HARDI model [34, 52, 164, 61, 134, 143].

An ODF in DW-MR is often presented as a symmetric spherical glyph that provides information on the three-dimensional diffusion profile within a brain voxel. We refer to these glyphs and their many variants [91, 74] as *diffusion shapes* since they provide a tangible shape-based representation of the dominant diffusion directions. The distance from the origin to the boundary of the diffusion shape is typically defined as being proportional to the value of the ODF in that direction; we use this definition. While an ODF is a function that assigns a scalar value to each point in S^2, a diffusion shape assigns either 0 or 1 to each point in $\mathbb{R}^3$, where a point inside the diffusion shape is assigned 1, and a point outside is assigned 0. This binary representation is crucial in our ensemble structure. However, diffusion shapes alone do not provide any information on ODF variabilities due to uncertainty caused by the different parameters. The main contribution of this chapter is an uncertainty analysis and visualization tool based on *ensembles* of diffusion shapes.

Our approach to analyze ensembles follows the framework of Löffler and Phillips [103] to construct a shape inclusion probability function (or SIP function), applied here to diffusion

shapes. That is, we construct a function on a three-dimensional domain where each point indicates the probability of inclusion in the diffusion shape. When there is no uncertainty in the data, this function is again binary where the values 1 or 0 indicate whether a point belongs to the diffusion shape, or not, respectively. However, in real scenarios, the uncertainty results in a region of points that take SIP values in the range $[0, 1]$. Studying and visualizing this heterogeneous region provides insight into the effects of different parameters describing the underlying uncertainty. We focus on one, we believe, particularly effective visualization of this SIP function. It is rendered using a 1D transfer function, which results in a 3D multiple iso-level visualization that approximates the inclusion probability at several levels simultaneously.

Following the approach of Löffler and Phillips to construct the SIP function, we first instantiate a number (1000) of DW-MR data sets drawn from the probability distribution modeling the uncertainty. For each instantiation, we construct the diffusion shape, and at each voxel, we report the fraction of diffusion shapes which include that point. This provides a sample estimate, but accompanying analysis provides accuracy bounds that depend only on the number of samples and complexity of the shapes, indicating that a large enough sample (such as 1000) is sufficient to accurately visualize the SIP for the diffusion shape. This entire approach produces a *quantifiable visualization* where the key structure is clearly presented *and* the underlying data values can be accurately recovered.

This chapter is organized as follows: In Section 6.2, we give an overview of the related work. In Section 6.3, we present the method to construct a SIP function from an ensemble of estimated diffusion shapes. Section 6.4 describes how the data are generated in the synthetic and real case. Results are presented in Section 6.5 where we employ this technique to study the impact of the background noise (Rice distributed) and b-value on the uncertainty in diffusion modeling. Finally, concluding remarks are drawn in Section 6.6.

6.2 Related Work

Several approaches for analyzing the uncertainty inherent in Diffusion Tensor Imaging (DTI) have been proposed. One approach studies the uncertainty in diffusion anisotropy measures derived from the components of the tensor [13], such as the FA (Fractional Anisotropy), RA (Rational Anisotropy), and principal diffusion directions [114, 81, 84, 99, 160, 35]. Often, bootstrapping methods are employed to simulate the distribution governing the random noise on real data sets. A different approach studies DTI (and HARDI) data sets, where several measurements in multiple imaging directions are available. These

multiple readings allow one to construct a distribution of possible values, and an estimation of noise related to the choice of b value [53, 143, 52, 67, 123], the registration [128, 76], the model fitting [7, 125, 90, 159, 77], the maximum finding, decomposition, or enhancement [78, 135, 75, 123, 134], or the fiber tracking algorithms [69, 41, 57, 119, 163, 79, 52].

Most of the uncertainty analysis and visualization focuses on the eigenvector directional uncertainty caused by the background noise [81, 70, 22] or the choice of a b value [52]. Only a few studies [164, 14, 7, 61, 162] address the uncertainty of the diffusion shape, which can describe complex white matter structures. Schwartzman [137] provides a simplified representation for diffusion tensors as ellipsoids and presents a 2D-quantile visualization along restricted slices. Principal component analysis (PCA; a mathematical procedure that uses an orthogonal transformation to convert a set of observations of possibly correlated variables into a set of values of linearly uncorrelated variables called principal components) was also employed to perform the uncertainty analysis in a second-order tensor field [162] and Q-ball imaging [61]. Recently, Zhan et al. [164] studied the influence of the number of diffusion-weighted directions on the diffusion shape and the resulting parameters. They showed that as the number of sensing directions increased, the signal-to-noise ratio also increased when measured with respect to fractional anisotropy (FA), rational anisotropy (RA), geodesic anisotropy (GA), and hyperbolic tangent of geodesic anisotropy (tGA) for an ROI in the corpus callosum. They also showed that the diffusion shape converges toward the ground truth shape when the number of sensing directions is increased. However, they did not study or visualize the more nuanced structural uncertainty with respect to the sensing parameter b, nor with respect to the parameters governing the true diffusion shape, such as the angle between the dominant diffusion directions and the corresponding weights. Also, Tournier et al. [143] visualize uncertainties of the ODFs using semitransparent glyphs, but are only able to represent the mean and standard deviation of variation in diffusion shapes. This lacks the ability to capture the full fiber orientation variabilities described by a large set of noise realizations. Therefore, a better understanding about uncertainty analysis and visualization in HARDI is needed.

6.3 Methods

We propose a general method that can be applied to visualize uncertainty in ODFs associated with various sources of data. In this chapter, we demonstrate our proposed method on ensembles of diffusion shapes derived from ODFs that are estimated from DW-MR data sets. First, we revisit how to determine ODFs. Our framework is agnostic to

which technique is used, but we describe the specific variant on which our visualization is built. Second, we discuss our proposed method to construct the SIP functions to visualize the uncertainty represented by a large sample estimate of the diffusion shapes according to the uncertainty in the data due to noise.

6.3.1 The Diffusion Shape Estimation Technique

Classical DTI constructs a diffusion tensor representing the major diffusion directions by solving the best fit (second-order) tensor in (6.1) using a least squares approach. A single diffusion tensor is associated with a second-order homogeneous polynomial which is incapable of describing complex diffusion patterns, such as crossing fibers. In HARDI, however, the estimation process results in an ODF that is associated with an even-order homogeneous polynomial of a higher order. Unlike classical DT, an ODF has more degrees of freedom and, hence, can represent 2 or more crossing fibers simultaneously and their corresponding weights (e.g., [149, 143, 44]).

Although our framework is applicable to ODFs associated with polynomials of any order, we focus here on fourth-order polynomials as they provide adequate trade-off between angular resolution and over-fitting due to noise [136]. The diffusivity function is

$$D(\mathbf{g}) = \sum_{a=0}^{4} \sum_{b=0}^{4-a} c_{ab} g_1^a g_2^b g_3^{4-a-b}, \tag{6.2}$$

where c_{ab} are the tensor coefficients and each vector $\mathbf{g} = [g_1, g_2, g_3]$ denotes a measurement direction. Figure 6.1 shows an example of different noise realizations of fourth-order diffusion shapes reconstructed from a synthetically generated dataset that simulates two crossing fibers at 60 degrees at a b-value of 2000 and an SNR of 10. The diversity of the reconstructed shapes illustrates variation of diffusion patterns under noise due to modest SNR values, and motivates the study of visualization of this inherent uncertainty.

There are various HARDI techniques to estimate ODFs (e.g., [143, 44, 149, 78]), and all are applicable within our framework. We choose the recent HARDI variant based on spherical deconvolution to perform all further experiments because it enables one to extract easily the diffusion information (e.g., [142, 78, 159]). These approaches ensure that the ODF is a positive definite entity. Following [78], we solve a minimization problem of the form

$$\min_D \frac{1}{2} \sum_{i=1}^{n} \left\| S(\mathbf{g}_i, b) - S_0 \int_{S^2} D(\mathbf{v}) K(\mathbf{g}_i, \mathbf{v}, b) d\mathbf{v} \right\|^2, \tag{6.3}$$

subject to a set of constraints that guarantees the positive-definiteness of the ODF in m reconstruction directions. The optimization problem is solved for the coefficients of

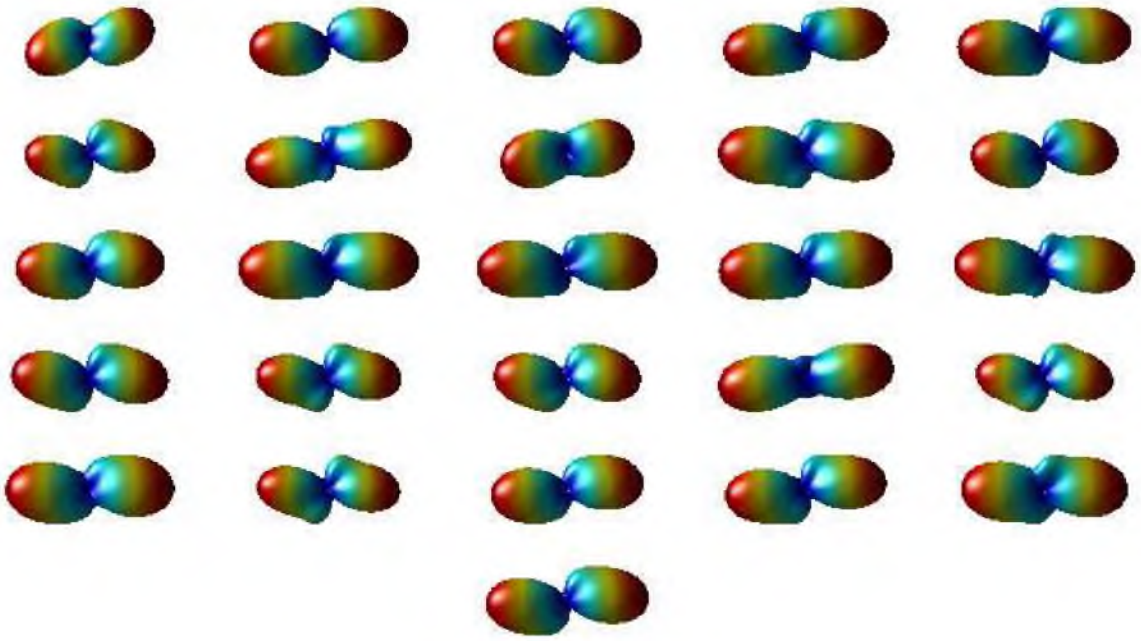

Figure 6.1: 25 noisy diffusion shapes at the crossing of two fibers at 60° and relative weights $0.7 : 0.3$. The SNR is 10 and b-value is 2000 s/mm^2. The original, noiseless diffusion shape is shown in the bottom row.

the homogeneous polynomial, c_{ab}, described in Eq. (6.2). The coefficients are estimated for a given set of diffusion-weighted measurements, S, and a convolution kernel, K. For a fourth-order polynomial, we estimate a set of 15 coefficients that describe it uniquely. Once the coefficients have been estimated, the associated diffusion shape is reconstructed according to Eq. (6.2). Importantly, the restriction that the ODF is described by 15 parameters prevents over-fitting, and will be relevant in the forthcoming accuracy analysis.

6.3.2 Diffusion Shape as a 3D Volume

To better understand how the diffusion shape varies with respect to the different acquisition parameters and background noise, we propose to change the widely used (single) triangular mesh visualization of diffusion shapes [12] (many instances are shown in Figure 6.1) to a probabilistic 3D volume, where volume rendering and isosurfacing techniques can be used to visualize these variations. Figure 6.2 and Figure 6.3 show the volume rendering of two tensors with four approximate iso-levels of the SIP function (defining 5 layers), indicating the probability (governed by uncertainty) that a diffusion shape occupies that part of the volume. Boundaries between layers demarcate the approximate iso-levels at the 25% quantile (inside grey region, outside dark grey region), the 50% quantile (inside dark grey region, outside green region), the 75% quantile (inside green region, outside blue region), and the 95% quantile (outside yellow region, inside blue region). That is, all points in the yellow region are included in the diffusion shape with probability of at least 0.95 and represent the *certain* part of the diffusion shape.

The diffusion shape is centered in a $200 \times 200 \times 200$ cube and normalized so the furthest point is at the boundary of the cube. This is justified by the fact that the outcome of the spherical deconvolution is a fiber-ODF, which only provides relative measurements of fiber orientations; hence, the scale is insignificant. The SIP function is evaluated at the center of each voxel. Its value is based on diffusion shapes estimated from 1000 different noise realizations of the raw data (as described in Section 6.4). Specifically, the SIP measures the fraction of diffusion shapes, each constructed using (6.2) from an instantiated data set, that contains the voxel center.

As the SIP function is calculated via a random process, it is subject to some error itself, but this process is unbiased and the error can be quantified [103]. In particular, via Theorem 4 in [103], the worst case error of a SIP function at any voxel is inversely proportional to the square root of the number of random instantiations m, and proportional to the square root of the complexity of the diffusion shape ν (i.e., the VC-dimension [152] dual to the shape, called ν' within proof of Theorem 4 [103], which can be bounded by the largest degree of a

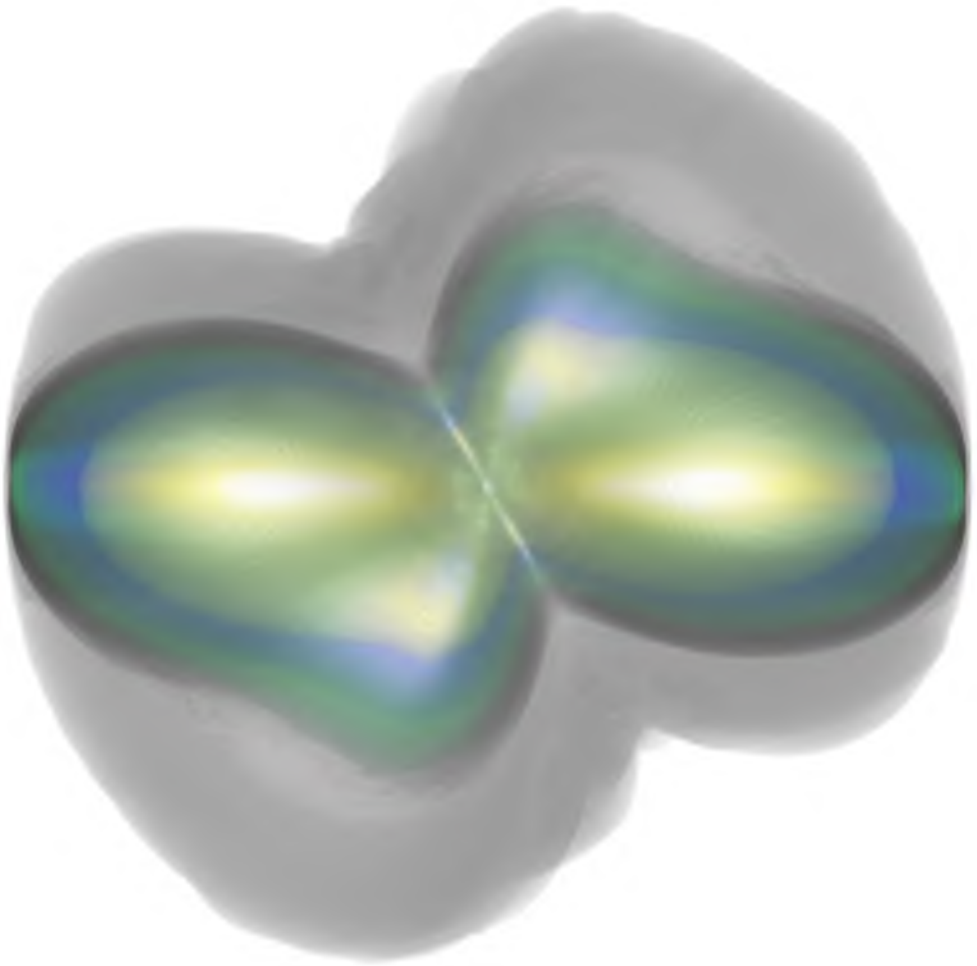

Figure 6.2: Visualization of the uncertainty in diffusion shape, two fibers crossing at 60 degrees with relative weight of 0.6:0.4, b-value 7000 s/mm^2, and SNR of 10.

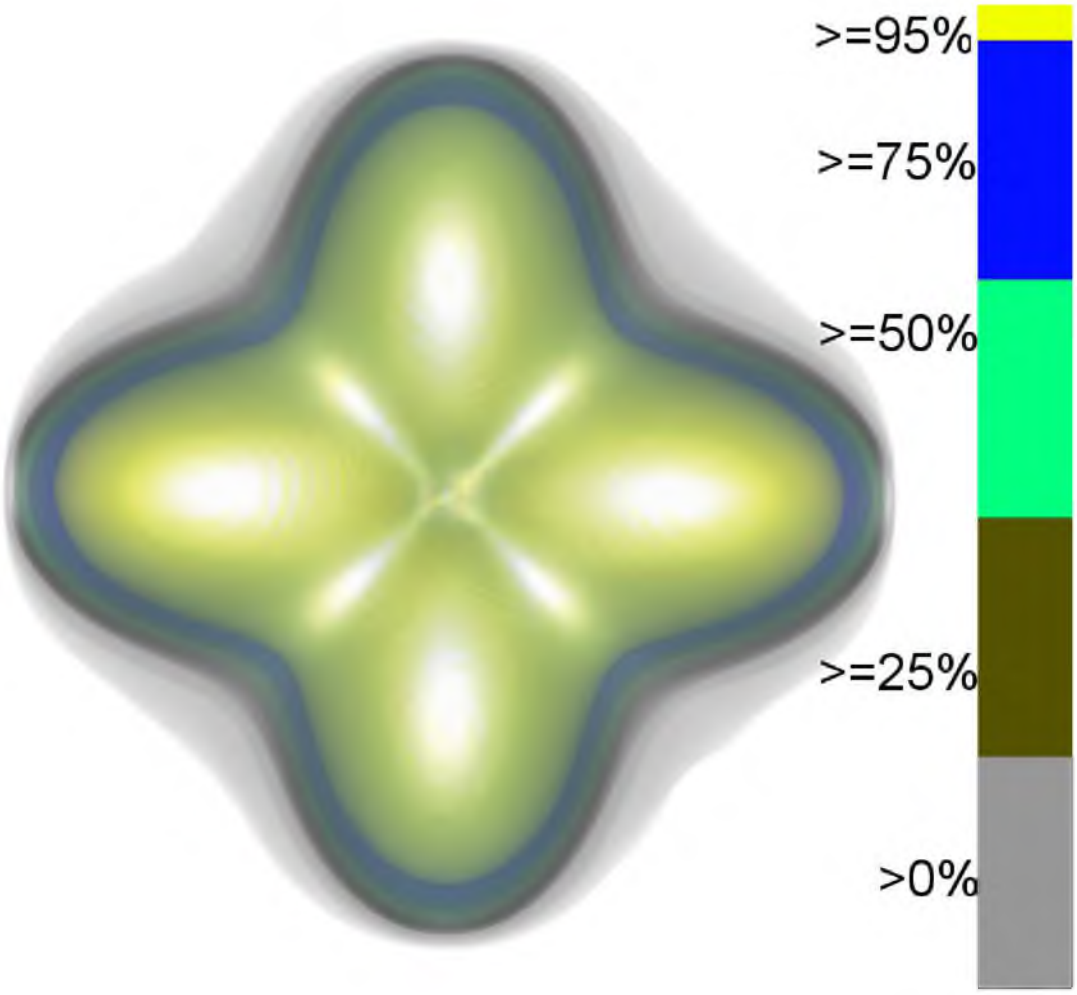

Figure 6.3: Visualization of the uncertainty in diffusion shape, two fibers crossing at 90 degrees with equal weight, b-value 1000 s/mm^2, SNR of 20 (with much less uncertainty than Figure 6.2).

polynomial describing a shape). Specifically, the maximum error ε of the SIP function over all voxels is approximately $\sqrt{(1/2m)(\nu + \ln(1/\delta))}$ with probability $1 - \delta$.

Thus, in our case, with $\delta = .01$, $m = 1000$, and $\nu = 15$, then on 99% of all simulations, the maximum error for any voxel is at most 10%. Most voxels will have much less error. We can interpret this as being able to reliably distinguish between iso-levels about every 10% (i.e., $> 90\%$, $> 80\%$, $> 70\%$, $\ldots$, $> 10\%$).

However, our visualization only chooses to highlight four different iso-levels (25%, 50%, 75%, 95%) and 5 probability regions ($< 25\%$, $25\% - 50\%$, $50\% - 75\%$, $75\% - 95\%$, $> 95\%$) because of the challenge of rendering a larger number of layers in 3D in an effective way. We use an analogous color map [127]. We choose one dominant color (we found a bright yellow visually appealing) to highlight the certain, innermost region. And then the subsequent, intermediate layers were shown as blues and greens which are adjacent on the color wheel. Neutral grays were chosen to represent the outermost layers with most uncertainty.

By decreasing the opacity of the outer layers, we are able to easily recognize all 5 regions on the 3D image, even through the outer layers completely occlude the inner layers. We found using more than 5 regions detracted from the visual aesthetics of the images without adding significant additional information. Most analogous colormaps derived to distinguish several iso-levels (for instance as provided by colorbrewer : `colorbrewer2.org`) contrast alternating levels by varying brightness. However, when using these colormaps in our 3D visualizer, we view the inner layers through the decreased-opacity outer layers; this combines these outer layers and muddles the view of the inner layers. As seen in Figure 6.4, which shows alternate color maps with between 4 and 8 layers, each layer is recognizable (on close inspection), but they appear increasingly drab as the number of layers increase, despite vibrant color maps.

This choice of only 4 iso-levels (and 5 regions) can be used to reinterpret the analysis in two ways. Either we can say with 1000 samples, we achieve 25% accuracy on the SIP function with probability greater than $1 - 1/10^{10}$, or we reach 10% accuracy, meaning each iso-level visualized (say the .5 iso-level) represents the true value with error of at most 10% (its value is between .4 and .6) in the entire SIP function with probability greater than 0.99.

The visualization technique that we propose here is applicable to various diffusion shape representations, reconstructed from DTI or HARDI data. Figure 6.5 illustrates our technique for computing SIP glyphs when using several different algorithms to generate the base diffusion shape, including classic DTI [120, 95], super quadratics [91], and fourth-order homogeneous polynomial [78], a representative of ODF-based visualizations[149].

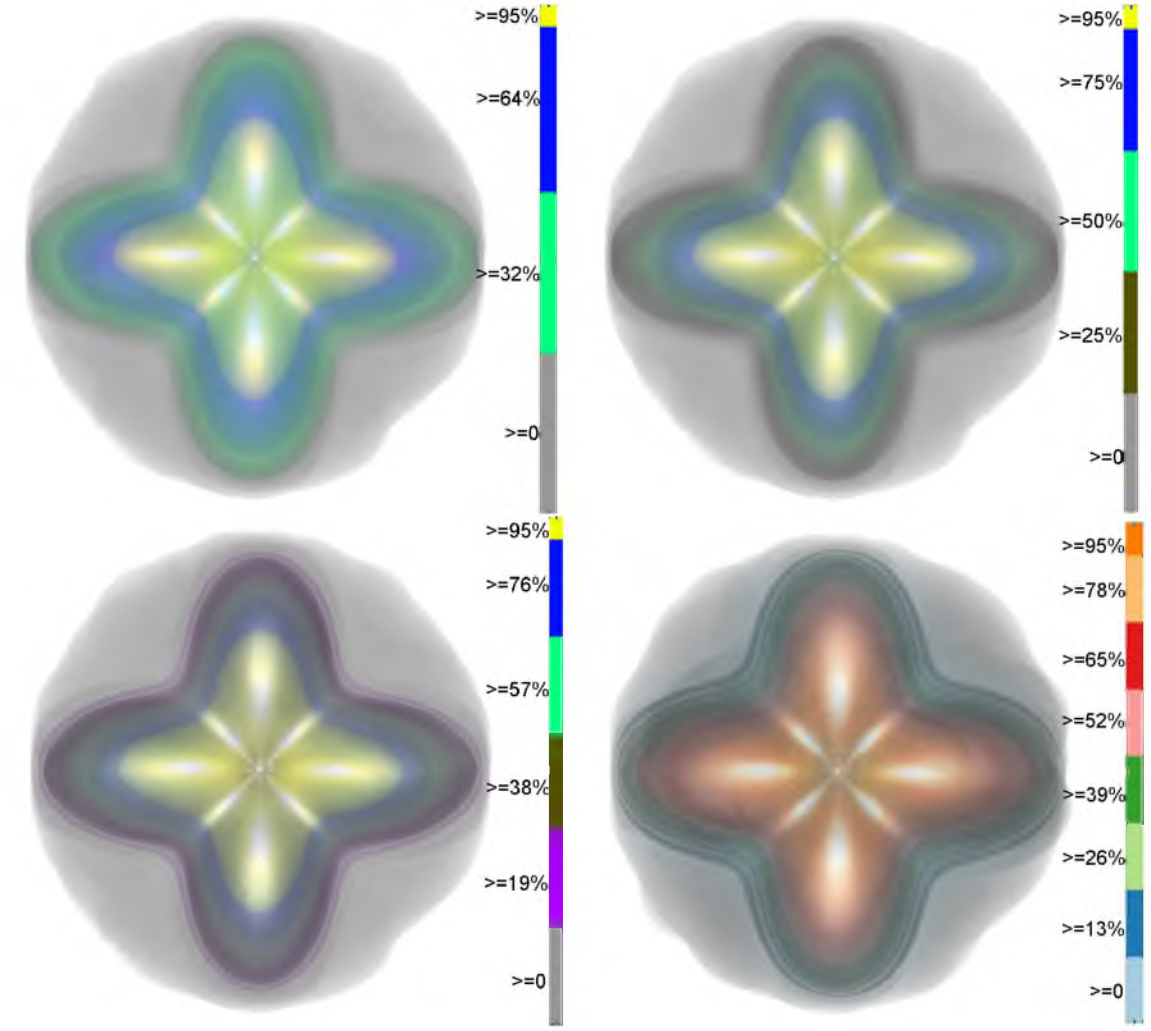

Figure 6.4: SIP function of diffusion shapes with $b = 1000$ and SNR of 5 illustrated with colormaps highlighting 4 (upper left), 5 (upper right), 6 (lower left), or 8 (lower right) layers.

Figure 6.5: SIP functions for different ODF representations: Left to right: ellipsoids (DTI), super quadratic (DTI), fourth-order homogeneous polynomial (HARDI). All use the same data with SNR of 20, b-value = 3000, two crossing fibers at 75°, and relative weights $0.6 : 0.4$.

As expected, the two techniques based on classical DTI (left two) fail to represent the two crossing fibers. Also, they exhibit more ambiguous uncertainty (note the larger, more uniform light grey region), presumably as the DTI technique is unable to consistently fit a single dominant direction on two crossing fiber directions. Hence, we focus here on the HARDI approaches.

6.4 Synthetic and Human Brain Data

We apply our method to synthetic and real, *in vivo*, human brain DW data.

6.4.1 Synthetic Data Design

In the synthetic data setting, two crossing fibers are simulated according to Eq. 4.12, the multicompartment model [147]. For both tensors, we assume a prolate tensor model with eigenvalues $\lambda_1 = 1.9 \cdot 10^{-4}\text{mm}^2/\text{s}$, $\lambda_2 = \lambda_3 = 1 \cdot 1.0^{-5}\text{mm}^2/\text{s}$ and b-values varying from 1000 s/mm^2 to 8000 s/mm^2 in 1000 s/mm^2 intervals. The principal eigenvectors of the tensors were chosen to simulate crossing fibers at angles of 30, 60, and 90 degrees. To test the influence of the fiber weights, data sets are generated with fiber weights equally or at ratio 0.7 : 0.3. The signal was simulated using 64 gradient directions. The clean data sets $S(\mathbf{g}_i, b)$ were corrupted by Rician distributed noise to create six levels of noisy data sets with SNR$_0$[1]: 50, 40, 30, 20, 10, and 5.

For each noise level, the process was repeated 1000 times. In each repetition, for each set of parameters (i.e., noise level, b-value, crossing angle, and weight), a diffusion shape was estimated according to the method described in Section 6.3.1. Then, the 1000 different instantiated diffusion shape samples are used to construct the SIP function as described in Section 6.3.2. See Figure 6.6, Figure 6.7, Figure 6.8, Figure 6.9, Figure 6.10, and Figure 6.11.

6.4.2 The Data Acquisition and Random Effects Simulation of Human Brain

The human brain data were acquired on a 3 Tesla Siemens Tim Trio scanner with a single-shot spin-echo EPI sequence with a resolution of $2 \times 2 \times 2\text{mm}^3$. One B0 image and 64 diffusion-weighted images, with image resolution of $106 \times 106 \times 76$, were acquired. To test the effects of the b-value, three different b-values were used to acquire the data: 1000, 2000, and 3000 s/mm^2. Then, eddy current correction and mutual information based affine registration was applied.

[1] SNR$_0 = S_0/\sigma$, where σ is the noise standard deviation.

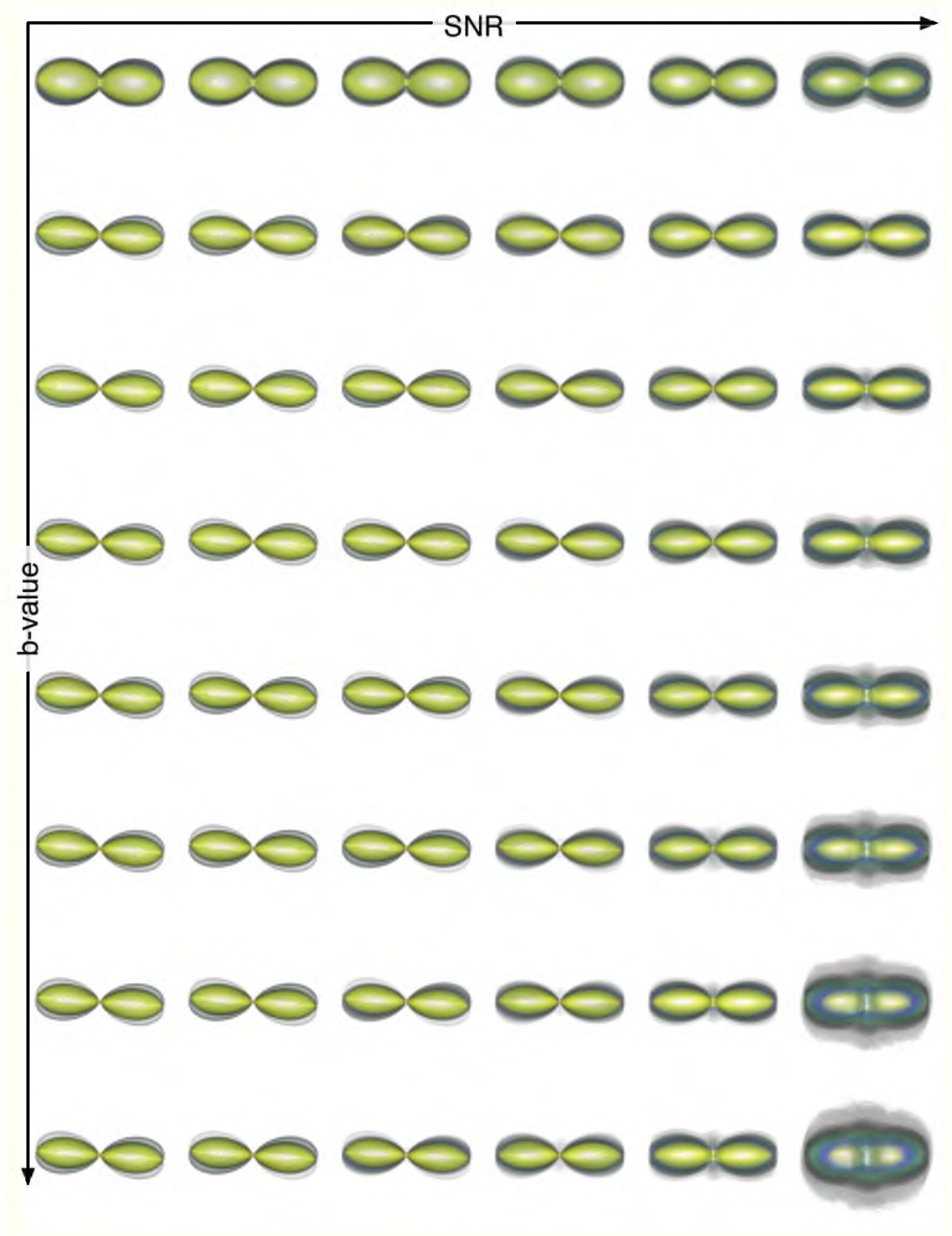

Figure 6.6: SIP functions of diffusion shapes for two fibers crossing at 30 degrees with equal weight. Six levels of noise (SNR = $\{5, 10, 20, 30, 40, 50\}$ from right to left) each with 8 different b-values (= $\{1, 2, 3, 4, 5, 6, 7, 8\} \times 1000\text{s/mm}^2$ from top to bottom) were used.

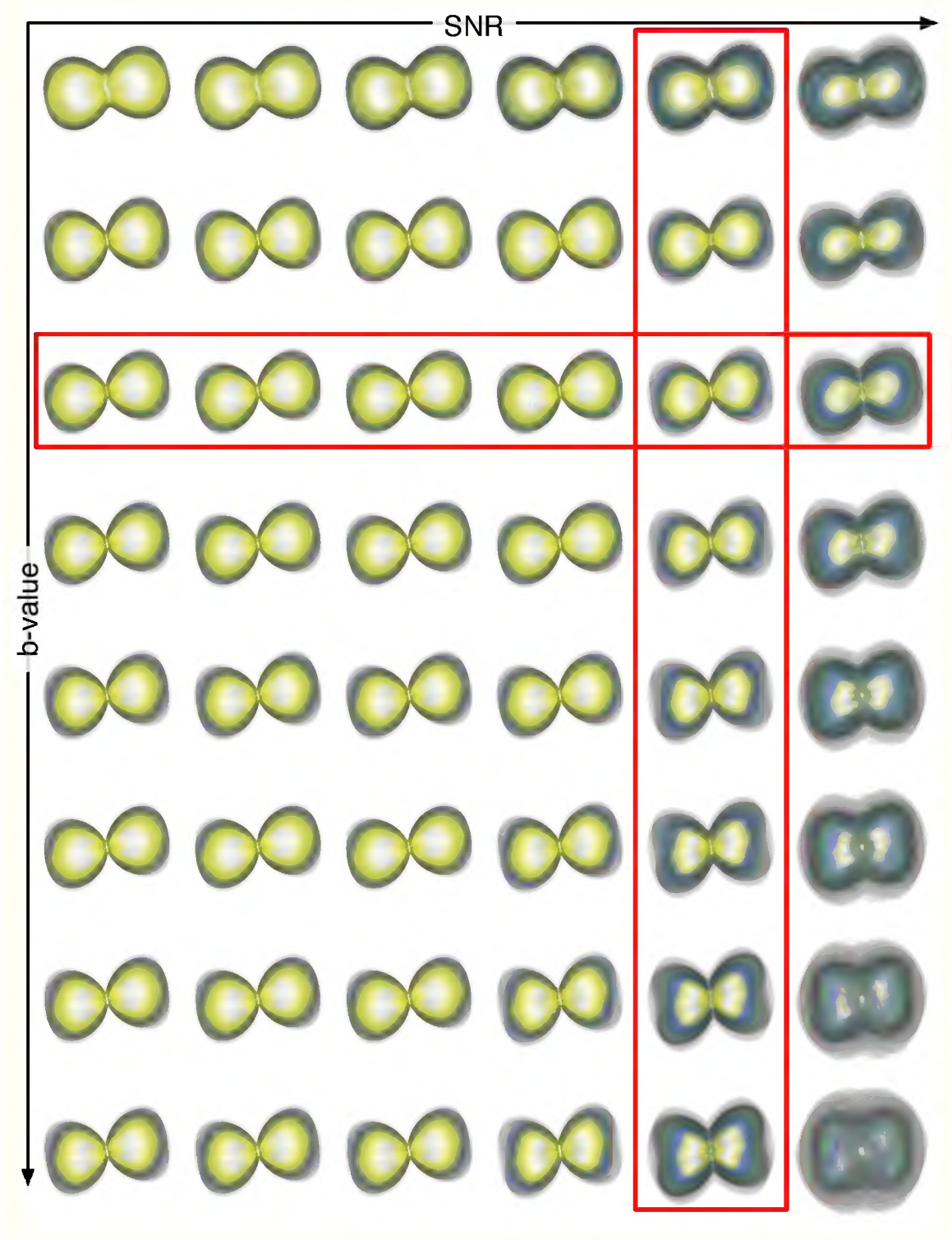

Figure 6.7: SIP functions of diffusion shapes for two fibers crossing at 60 degrees with equal weight. Six levels of noise (SNR = $\{5, 10, 20, 30, 40, 50\}$ from right to left) each with 8 different b-values (= $\{1, 2, 3, 4, 5, 6, 7, 8\} \times 1000\text{s/mm}^2$ from top to bottom) were used.

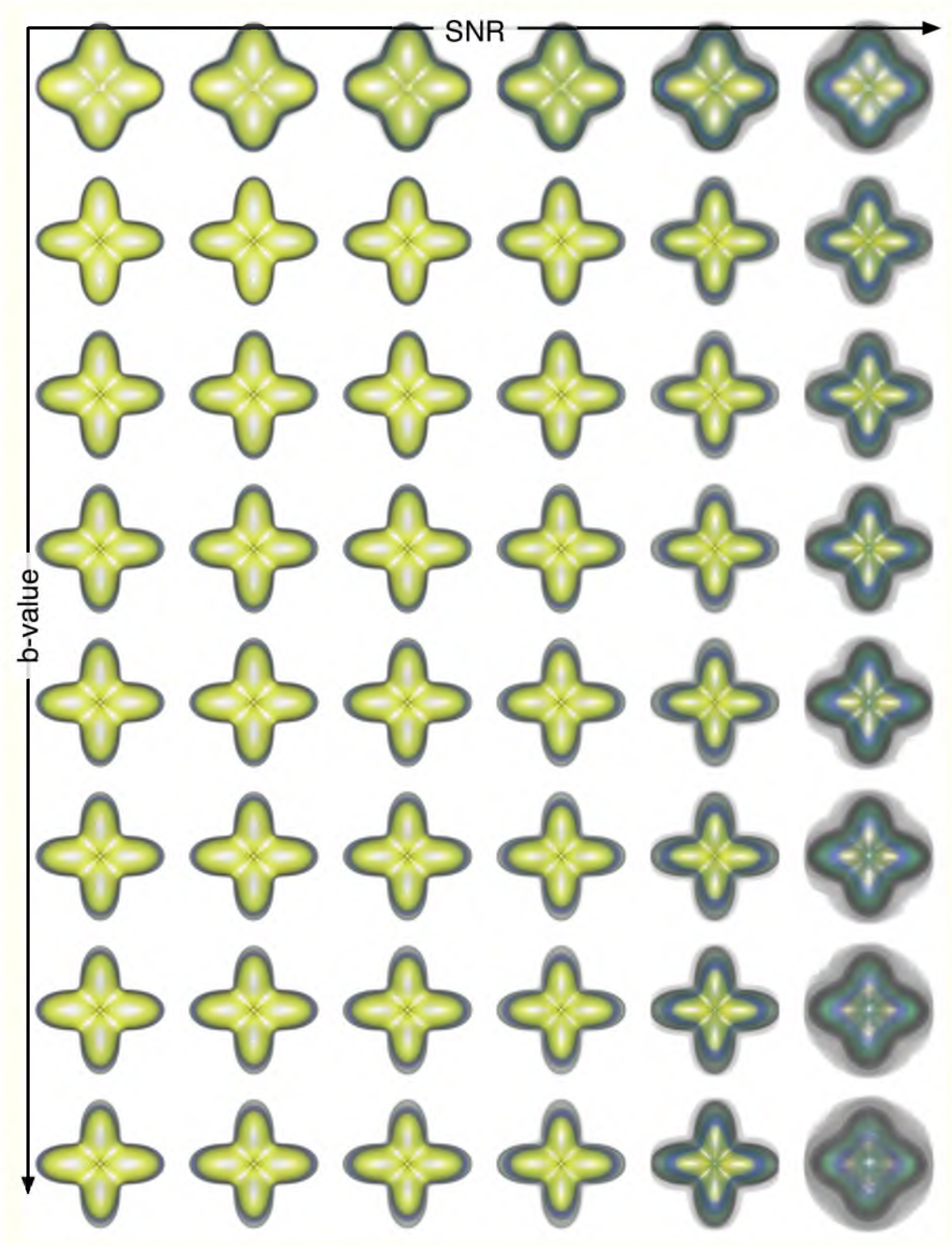

Figure 6.8: SIP functions of diffusion shapes for two fibers crossing at 90 degrees with equal weight. Six levels of noise (SNR = $\{5, 10, 20, 30, 40, 50\}$ from right to left) each with 8 different b-values (= $\{1, 2, 3, 4, 5, 6, 7, 8\} \times 1000\text{s/mm}^2$ from top to bottom) were used.

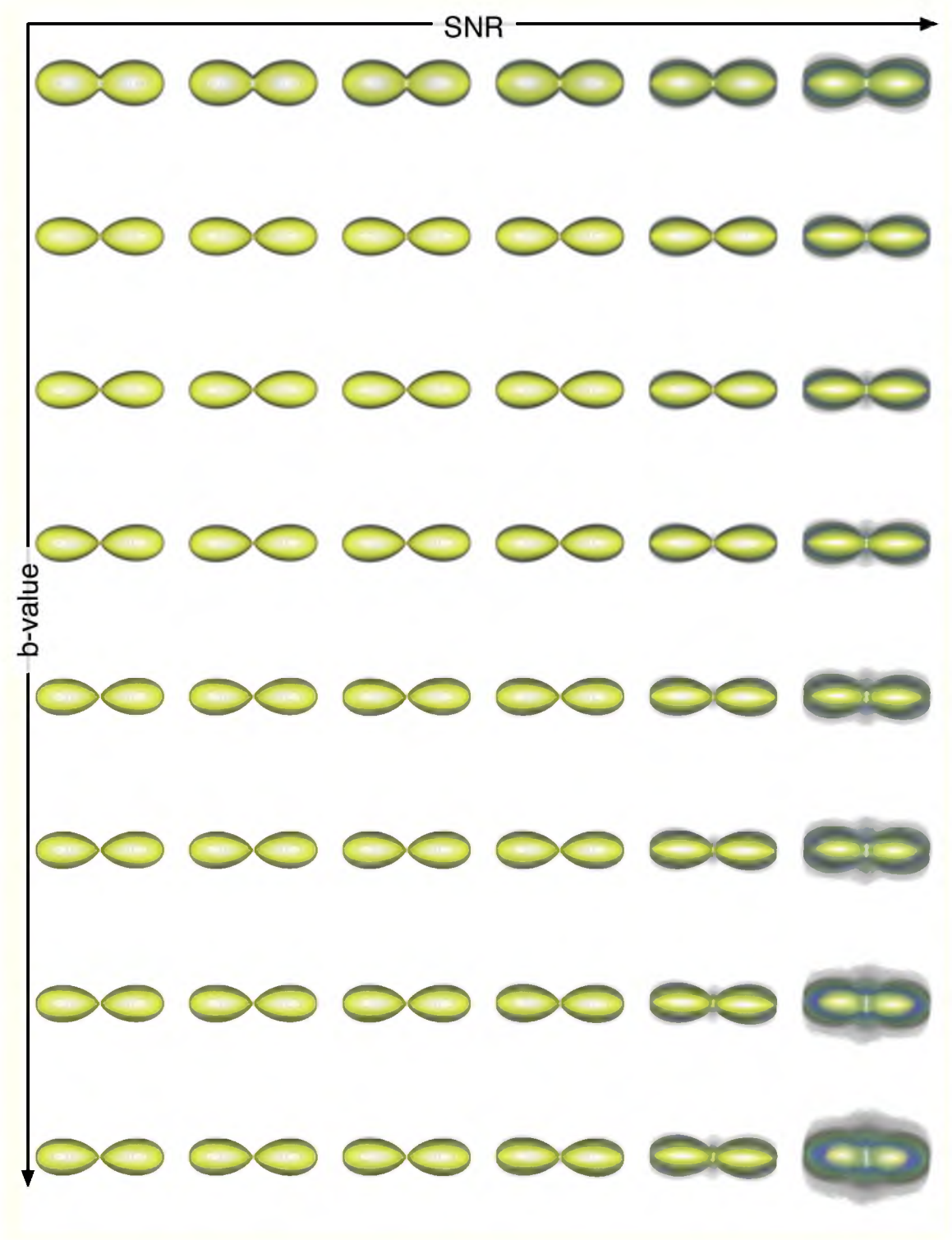

Figure 6.9: SIP functions of diffusion shapes for two fibers crossing at 30 degrees with relative weights of 0.7 and 0.3. Six levels of noise (SNR = $\{5, 10, 20, 30, 40, 50\}$ from right to left) each with 8 different b-values (= $\{1, 2, 3, 4, 5, 6, 7, 8\} \times 1000\text{s/mm}^2$ from top to bottom) were used.

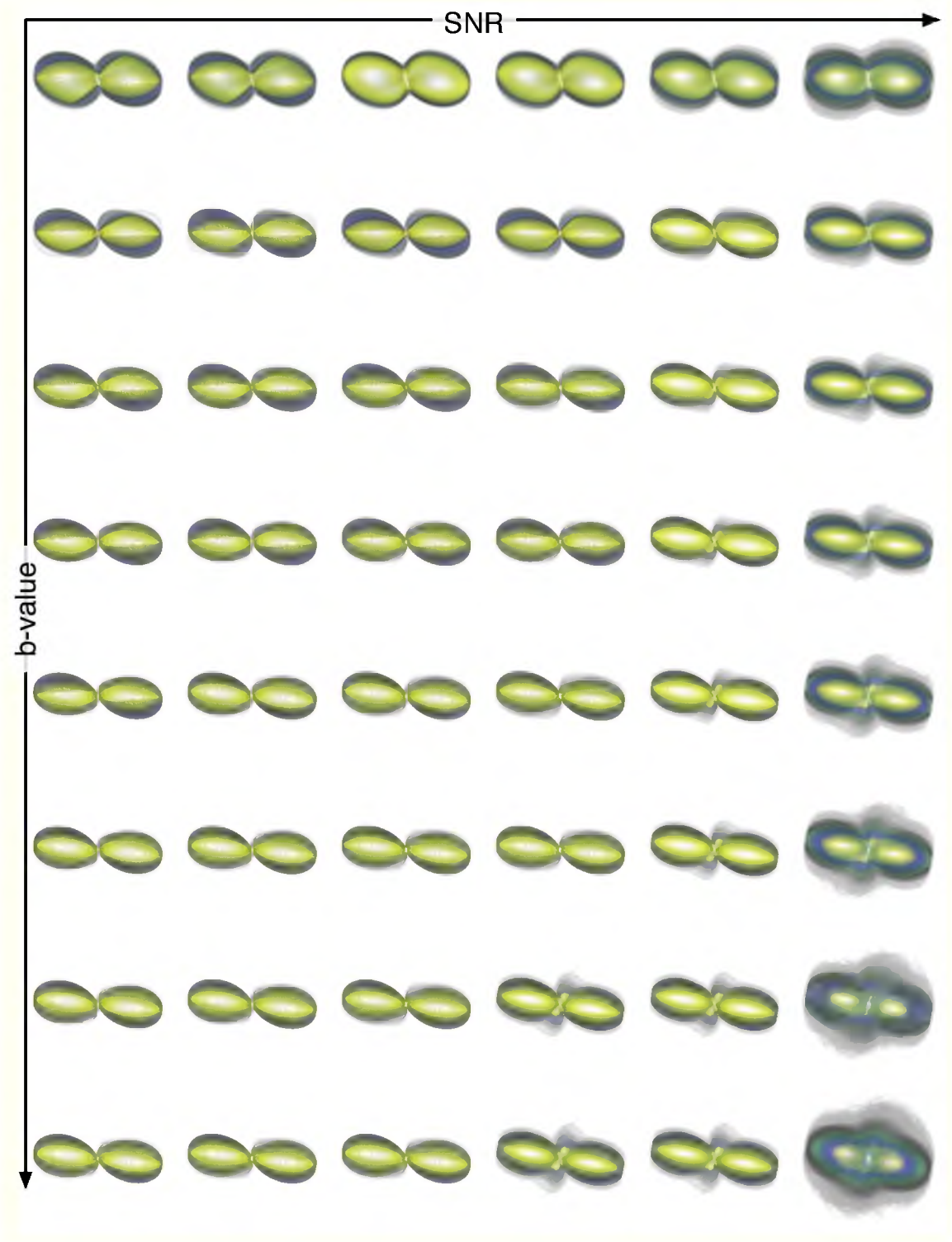

Figure 6.10: SIP functions of diffusion shapes for two fibers crossing at 60 degrees with relative weights of 0.7 and 0.3. Six levels of noise (SNR = $\{5, 10, 20, 30, 40, 50\}$ from right to left) each with 8 different b-values (= $\{1, 2, 3, 4, 5, 6, 7, 8\} \times 1000\text{s/mm}^2$ from top to bottom) were used.

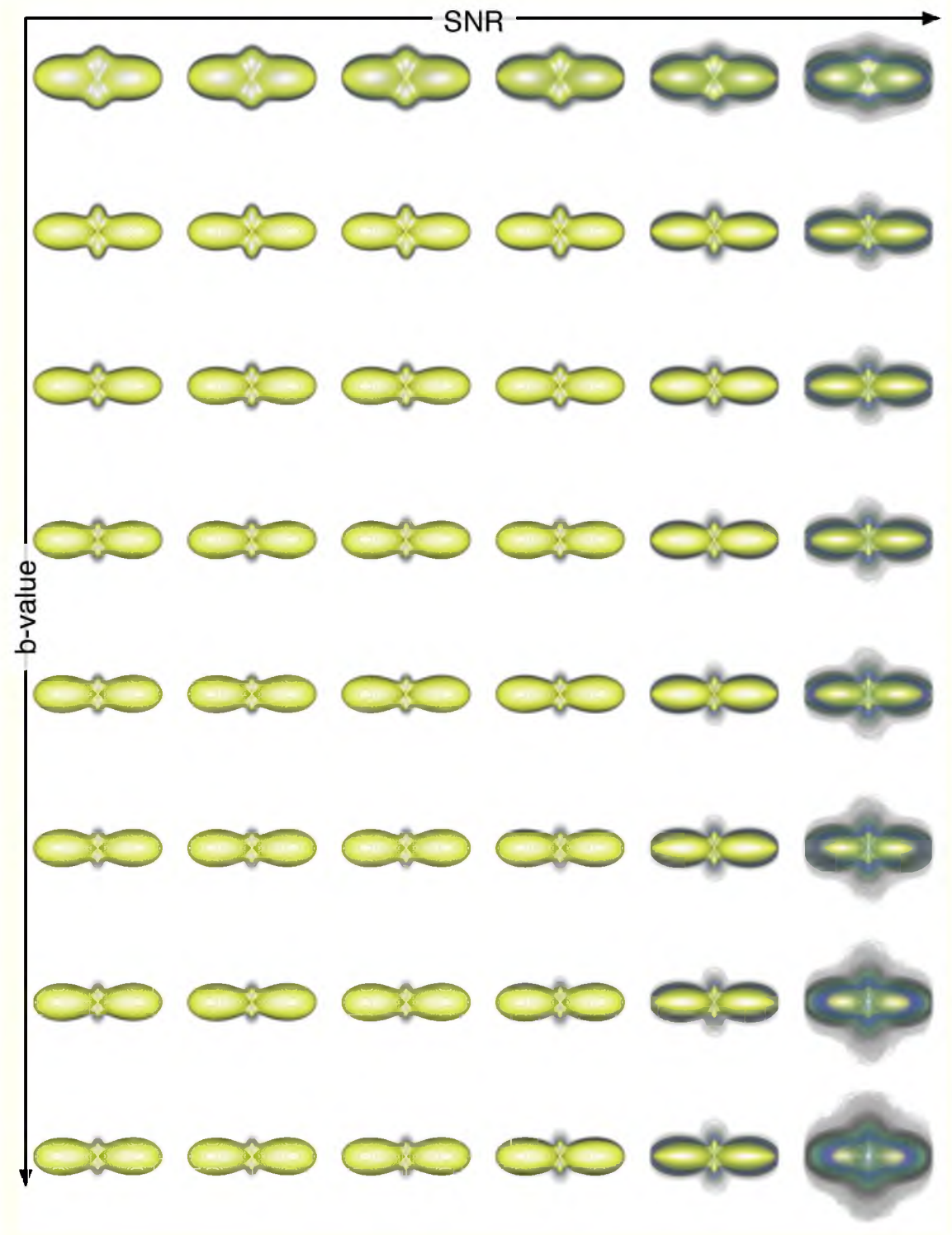

Figure 6.11: SIP functions of diffusion shapes for two fibers crossing at 90 degrees with relative weights of 0.7 and 0.3. Six levels of noise (SNR = $\{5, 10, 20, 30, 40, 50\}$ from right to left) each with 8 different b-values (= $\{1, 2, 3, 4, 5, 6, 7, 8\} \times 1000\text{s/mm}^2$ from top to bottom) were used.

There are two predominant approaches to simulate noise in real data sets for DW-MR: directly adding Rician noise, and wild bootstrapping. Both techniques start by first solving for a single ODF or DT. For each sensing direction $\mathbf{g}_i$, let $S_i = S(\mathbf{g}_i)$ be the sensed value. Let $\mathrm{c}S = \{S_1, \ldots, S_n\}$ be this data set and $\hat{D}$ be the estimated ODF according to the method discussed in Section 6.3. Then, for each direction $\mathbf{g}_i$, we compute $\hat{S}(\mathbf{g}_i)$ as a function of $\hat{D}$ using (6.3). The residual is given by $r_i = \hat{S}(\mathbf{g}_i) - S_i$.

The technique of adding Rician noise estimates the standard deviation σ of a complex Gaussian using the r_i values. It instantiates uncertain data sets $\mathrm{c}S_j = \{S_{1,j}, S_{2,j}, \ldots, S_{n,j}\}$ from the perceived noise levels. To replicate each sensed value, it sets $S_{i,j} = \hat{S}(\mathbf{g}_i) \oplus R(\sigma)$, where $\oplus R(\sigma)$ signifies the perturbation of $S(\mathbf{g}_i)$ by Rician noise with standard deviation of σ. It has been observed that the noise in these DTI measurements closely follows a Rice distribution [65], so this technique has been accepted as a realistic way of simulating noise [16].

Wild bootstrapping [35, 82] makes an effort to preserve the heteroscedasticity of the noise (that is, certain areas have larger noise distributions than others). But, as a consequence, it sacrifices the strict adherence to the Rice noise model. Again starting from each $\hat{S}(\mathbf{g}_i)$, we instantiate a data set from the noise as $\mathrm{c}S_j = \{S_{1,j}, S_{2,j}, \ldots, S_{n,j}\}$. We then set $S_{i,j} = \hat{S}(\mathbf{g}_i) \pm r_i$, where the choice of adding or subtracting the residual is chosen independently at random for each simulated measurement and instantiated data set (i.e., each j and i).

A third approach estimates the posterior probability density functions of the model parameters under certain noise models [20].

To simulate noise on real data, any of these conventional methods could be used. They would be repeated 1000 times (i.e., for $j = 1, \ldots, 1000$) to instantiate 1000 data sets representing the distribution of possible data sets as prescribed by the residual noise in the sensed data. In our experiments, we choose to follow the wild bootstrapping method since we believe it will highlight our algorithm's ability to visualize complicated heteroscedastic noise.

6.5 Results

6.5.1 Uncertainty in Diffusion Shapes Generated from Synthetic Data

Using synthetic data, we demonstrate the usefulness of our diffusion uncertainty visualization by comparing other approaches, and show variations of SIPs of diffusion shapes for varying parameters.

6.5.1.1 Comparison to Alternate Visualizations

The most standard visualization of an ODF is hiding the uncertainty and showing the one best-fit diffusion shape. Not only does this not illustrate the uncertainty, but it gives the illusion that there is no uncertainty, which as demonstrated by other figures is a dangerous assumption.

Another approach is to treat each uncertain shape in the ensemble of uncertain shapes as a vector of data elements. Each element is represented as either each discrete diffusion direction, or as each voxel's binary value determined by inclusion in the diffusion shape. Then, given a set of 1000 diffusion shapes, we have a matrix of data, with each diffusion shape vector as one column. We can run PCA on this matrix and determine the most dominant modes of variation. From the visualization perspective, there are two clear disadvantages of this approach. First, it is difficult to visualize more than one principal component in a single glyph. The typical approach is to show the variation along the top several principal components in separate visuals of the same object, but in the context of diffusion shapes, this is not an option since there are typically a collection of them. Additionally, displaying the variation along the top component is usually done by overlaying two (or more) images, offsetting the mean shape $\hat{D}$ by 2 standard deviations in the positive and negative direction of variation. These generated shapes may not actually be physically releasable configurations. For instance, if all of the variation comes from two modes, one standard deviation from the mean shape in each direction, then no configuration ever reaches two standard deviations away. Second, the first few principal components (let alone the top one) do not capture all of the complex variations of the diffusion shapes. Figure 6.12 shows the cumulative variation explained by the top $k = \{1, 2, \ldots, \}$ principal components. Only about 55% of the variation is shown by the top component, and it takes approximately six components to explain 90% of the variation. Intuitively, since the diffusion shape is described by $\nu = 15$ parameters, it is reasonable to expect 15 different components to capture the main sources of the variation. This partially agrees with one of the findings in [61], which reflects the complexity of the meaning of the first several major principal axes.

A third attempt at visualizing the diffusion uncertainty on a single glyph is to choose a single representative diffusion shape and use a color map to annotate the amount of uncertainty along each direction. A variation of this paradigm is present in the thesis of Hlawitschka [73]. This approach does not have any dramatic short-comings, and we produce a variant of our own. We measure the variability of the diffusion shape between the 50% and 95% iso-levels of the ensemble of diffusion shapes and display this using a colormap on

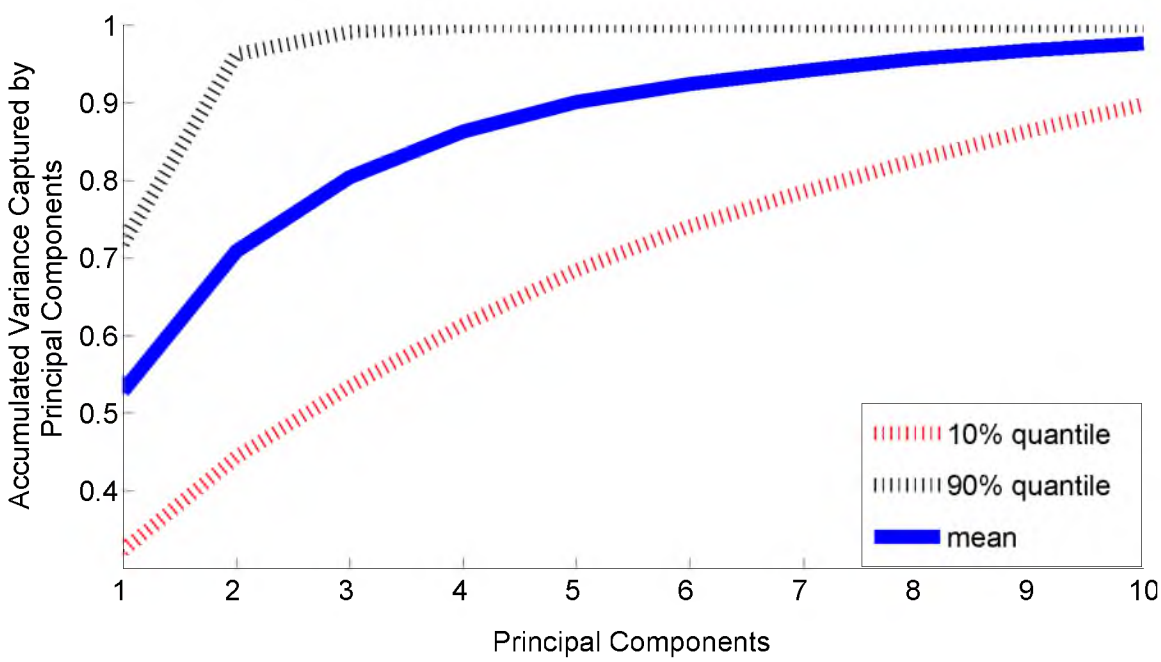

Figure 6.12: Distribution of cumulative variation explained by up to the first 10 principal components for cases shown in Figure 6.6 to Figure 6.11.

the 50% iso-level. This leaves the glyph a bit less cluttered, and provides a sense of how stable the 50% iso-level is with respect to the 95% iso-level. However, this approach (as well as other variants) fail to capture how the uncertainty changes (and robustness of iso-levels change) among all iso-levels. Just showing the standard deviation, or any local variability, does not capture the full distribution of variation in the same way our visualization does.

To compare these glyphs, we present them on the same data set in Figure 6.13. This simulates two crossing fibers at 60°, with relative weights of 30%, 70% using b-value of 3000 and SNR of 20. Much more nuanced and heteroscedastic uncertainty is presented in our visualization using a SIP function of diffusion shapes on the far right.

6.5.1.2 Variation in Parameters

To document the inferences available from the use of SIP functions of diffusion shapes, we show a variety of glyphs generated by varying the parameters to the synthetic data. We show either two crossing fibers at angles of either 30, 60, or 90 degrees, and with relative weights of either 50% and 50%, or of 30% and 70%. We then vary the manner in which the data is gathered by letting the b-value be from $\{1000, 2000, 3000, 4000, 5000, 6000, 7000, 8000\}$, and the SNR be from $\{5, 10, 20, 30, 40, 50\}$; see Figure 6.6 to Figure 6.11.

Figure 6.14 shows the diffusion shape size change with the different b-values, different fiber weights, and different noise levels. The tensor size was measured in the following way: we first normalized the homogeneous polynomials using the same factor and put it in a grid volume with the same size, then we count the number of the grid voxels bounded by the fourth-order tensor. The total number of the voxels included in the union of all diffusion shapes will be an approximation of the size of the tensor. We can see that the influence of different fiber weights is quite small, and the size of the tensor seems to increase with the increasing of the noise level, especially when SNR is 10 and 5. However, the biggest influence is due to the b-value. The size of the tensor is shrinking with the increase of the b-value.

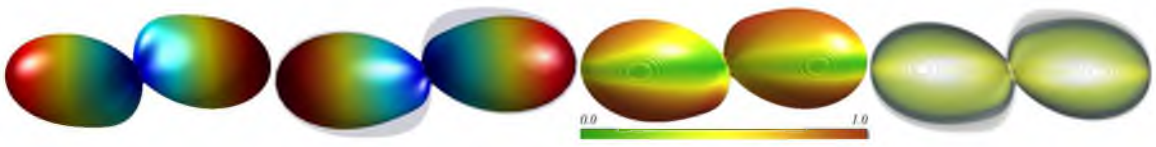

Figure 6.13: Different visualizations of diffusion uncertainty in a single glyph. Left to right: the single best-fit diffusion shape; two standard deviation of top principal component in either direction superimposed; local variation color-mapped onto the 50% iso-level of diffusion shape; and SIP function of diffusion shapes with iso-levels at 25%, 50%, 75%, and 95%. The colormap for the left two images signifies ODF values, not uncertainty.

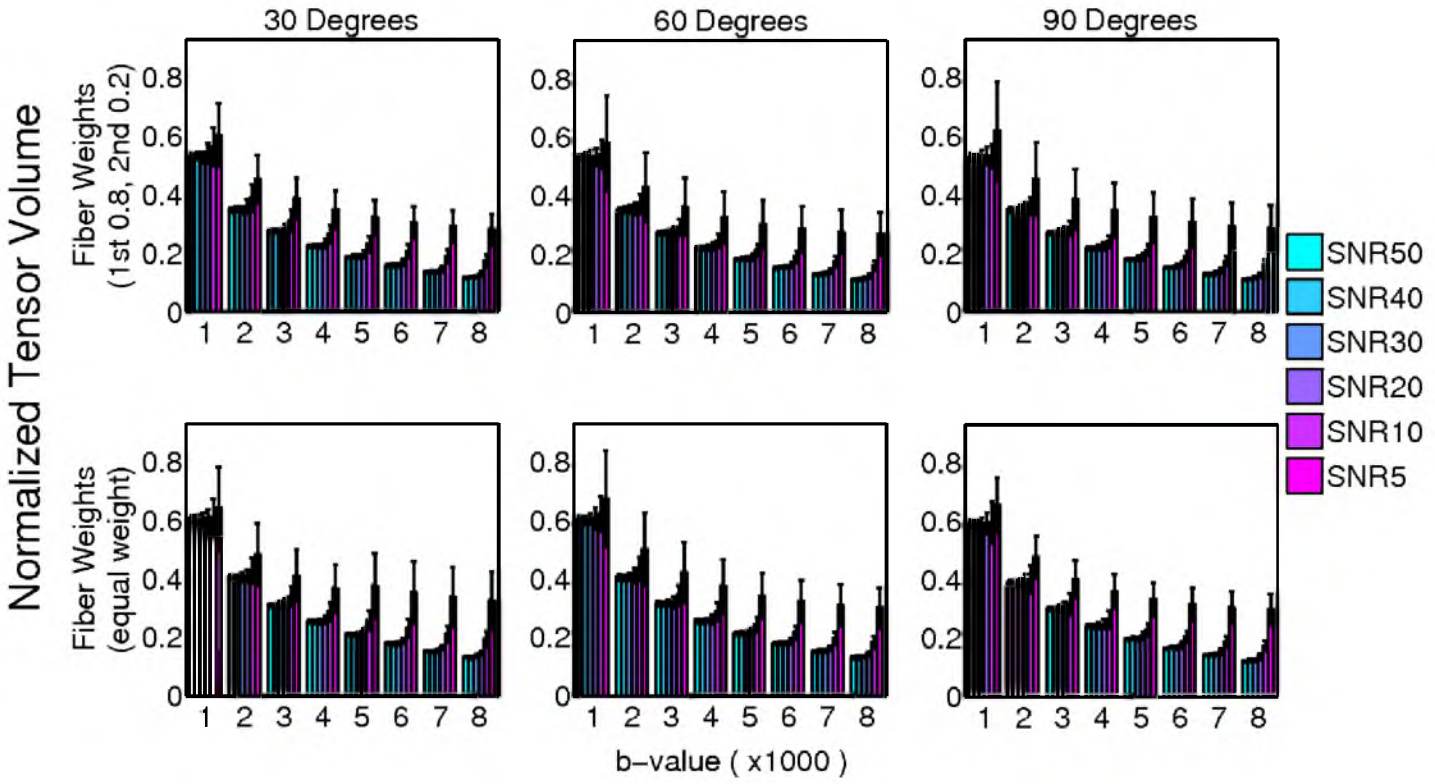

Figure 6.14: The tensor volume quantification for two fibers crossing at 30 (left-hand side), 60 (middle), and 90 (right-hand side) degrees. Two groups of fiber weights are used: 0.7 and 0.3 (top row), and 0.5 and 0.5 (bottom row). Six levels of noise with the SNR of 50, 40, 30, 20, 10, and 5 were applied.

For visualization and comparison purposes, the uncertain diffusion shapes have been individually normalized so they are all approximately the same size, and the volume shrinking effects due to mono-exponential decay of the dMRI signal shown in Figure 6.14 are ignored. Figure 6.2 and Figure 6.3 show two enlarged SIP functions for diffusion shapes.

Immediately, two possible conclusions could be drawn from Figure 6.6 to Figure 6.11, although further study should be performed before making any definitive claims. First, as the b-value increases, the variability and hence uncertainty increases and then decreases. It could be inferred that the best b-value to minimize uncertainty is around 2000 or 3000; or any value in that range. Second, as expected, as the SNR increases, the uncertainty decreases. Interestingly, not much is gained as the SNR goes above 40 (or even above 30 in some cases). This might suggests that DW images with an SNR of 40 are sufficient for successful HARDI analysis and visualization.

A more quantitative way to analyze the amount of uncertainty in the diffusion, based on the variation of input parameters, is to use a measure we call the *certain volume ratio*, which computes the ratio of the volume of the region within the 95% iso-level (the certain volume) to the area inside the 50% iso-level (a representation of the typical volume). Both parts of the ratio are robust and thus not sensitive to outliers in the generation of the diffusion shapes. The larger the ratio, the closer the 50% iso-level is to the 95% iso-level, indicating that most shapes are all very similar. Figure 6.15 and Figure 6.16 plot certain volume ratio as a function of b-value and SNR, respectively, and support our visual observations about the b-value and SNR. The certain volume ratio is plotted for the glyphs corresponding to those highlighted in Figure 6.6 to Figure 6.11.

6.5.2 Uncertainty in Diffusion Shapes Generated from Human Brain Data

The human brain data were acquired using the parameters provided in Section 6.4.2. The SNR_0 values of the $b = 1000$, 2000, and 3000 s/mm^2 acquisitions, were estimated as 21.06, 19.76, and 19.48, respectively. These estimates were derived from the mean intensity of five different regions of interest (ROI) in the white matter and grey matter regions, divided by the variance of the pure background intensity of the $S0$ image; one ROI is shown in Figure 6.17.

For the spherical deconvolution, we have used the single-fiber response kernel (e.g., [159]), where the kernel parameter was estimated from the data to compensate for the different b-values, as described in [142].

Both single triangular mesh diffusion shapes as well as the SIP functions of diffusion

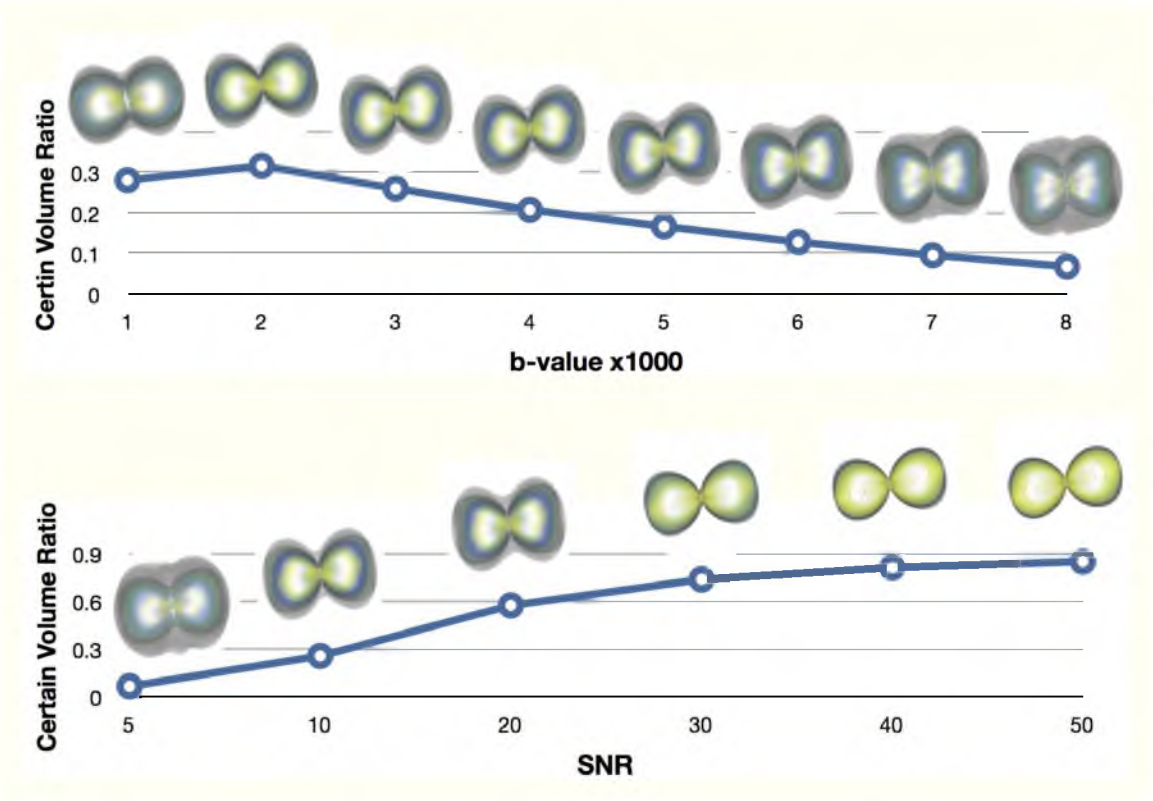

Figure 6.15: Plots of certain volume ratio as a function of b-value (top) and SNR (bottom). All experiments on synthetic example of two fibers crossing at 60° with equal relative weights and an SNR of 10 (top) or b-value of 3000 (bottom).

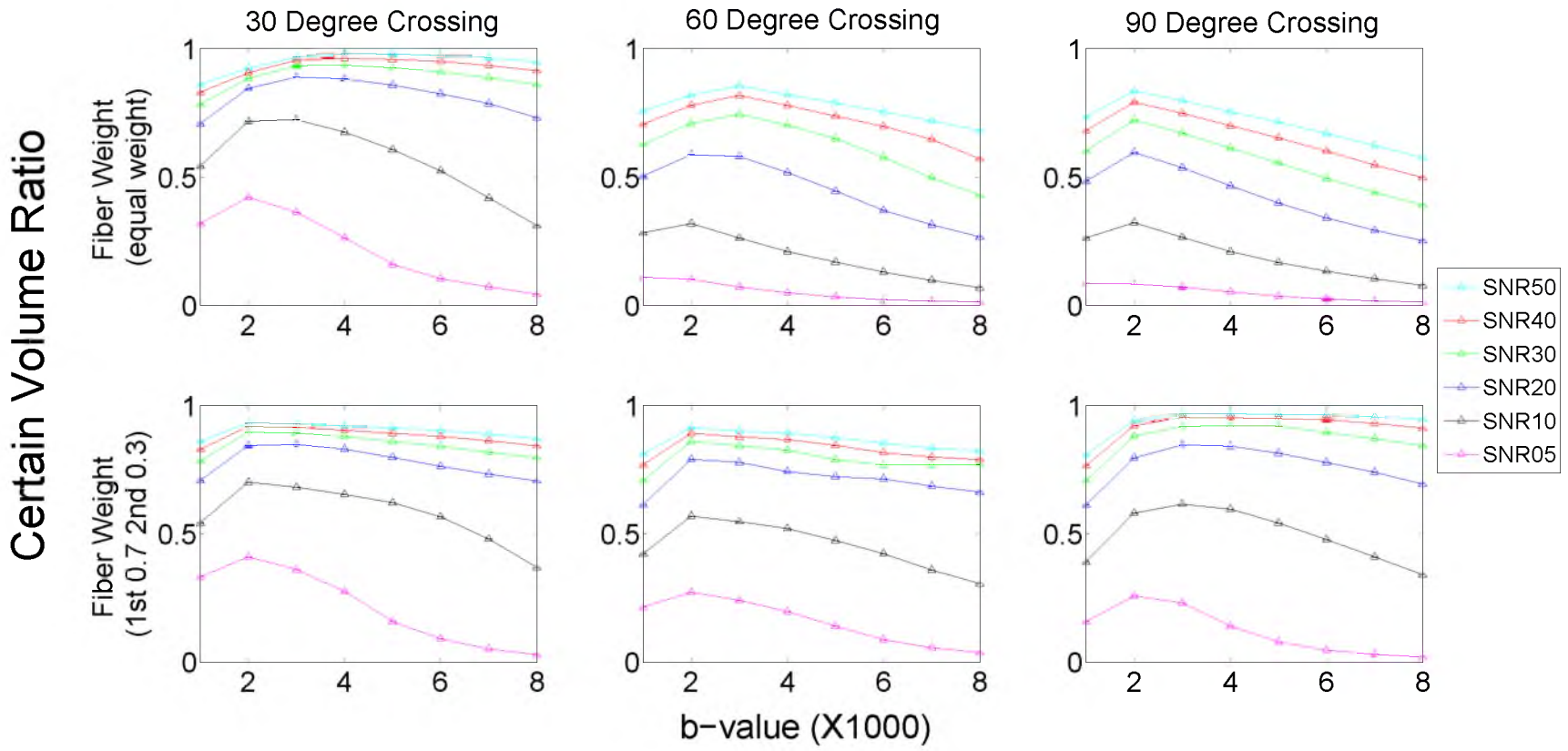

Figure 6.16: The certain volume ratio for two fibers crossing at 30 (left-hand side), 60 (middle), and 90 (right-hand side) degrees. Two groups of fiber weights are shown: 0.5 and 0.5 (top row) and 0.7 and 0.3 (bottom row). Six levels of noise with the SNR_0 of 50, 40, 30, 20, 10, and 5 were applied.

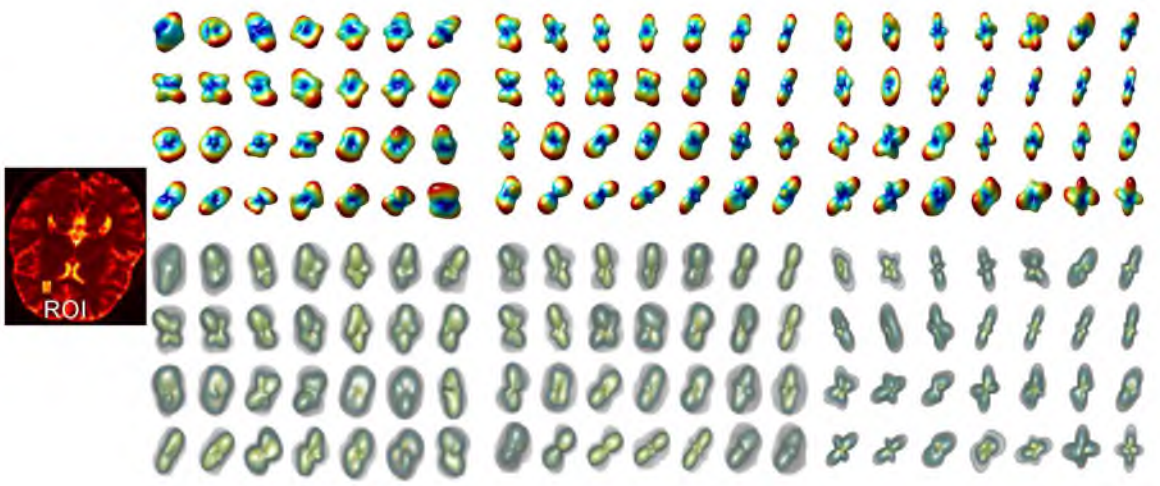

Figure 6.17: Left: 7 by 4 region of interest from the white matter. Right three columns: human data with a b-value of 1000, 2000, and 3000 s/mm2. Each column shows 28 diffusion shapes as a single triangular mesh (top) and a SIP function using 1000 instantiations of each diffusion shape.

shapes are shown. The extent of the uncertainty is shown clearly in the latter.

Our analysis based on the certain volume ratio (as shown in Figure 6.16) recommends a b-value of 2000. By visual inspection of the uncertain shapes in Figure 6.17, the data sensed with a b-value of 2000 seems to have the least uncertainty; a b-value of 1000 also seems adequate. Note that the regions with $b = 3000$ have been scaled small since the gray region with low probability is noticeably larger. This is supported by the certain volume ratios of 0.343, 0.367, and 0.283 for b-values of 1000, 2000, and 3000, respectively. Thus, our guidelines recommending a b-value of about 2000 s/mm^2 for this noise level were observed to be useful.

Also notice the variability of the single best-fit diffusion shape on the top of Figure 6.17 as the b-value changes. These, in principle, should represent the same diffusion functions, but due to real sensing errors, they have nontrivial variance. Our presented SIP functions of diffusion shapes below faithfully represent a realistic amount of uncertainty, preventing a user from drawing too strong a conclusion about the true diffusion patterns from these data.

6.5.3 Uncertainty Quantification Using Dominant Directions

A convenient way to simplify the representation of diffusion tensors is by their dominant diffusion directions, derived by the rank-two decomposition. Representing diffusion by just one or two directions clearly loses information regarding the importance of the nondominant

diffusion directions, the variability in these directions, and the uncertainty inherent in the diffusion. Furthermore, accurately constructing these directions from fourth-order tensors is still an open research problem [28] since the current state-of-the-art introduces a noticeable amount of error, especially when the directions are similar. However, because of their convenient representation, it is simple to compute quantification measures, and these measures can be simple to interpret, although not always accurate. As argued above, the use of fourth-order tensor shapes provides a clean and informative alternative approach, especially for understanding uncertainty; below, we discuss the common specific measures based on dominant diffusion directions and the particular issues that can arise.

Given a fourth-order diffusion tensor estimate $\mathcal{D}$, we can derive two dominant diffusion directions v_1 and v_2 along with corresponding weights w_1 and w_2, such that $w_1 \geq w_2$ [78, 135]. The weights correlate to the relative importance of the eigenvectors. Much research in numerical analysis [145] deals with the instability in eigenvectors, and avoids using them as a reliable measure of shape, especially when the eigenvalues are similar or small; related issues arise in our context when the weights are similar or small.

In the analysis of techniques for DT-MRI, and specifically HARDI, several common measures are used to compare the top two observed direction-weight pairs $(\hat{v}_1, \hat{w}_1)$ and $(\hat{v}_2, \hat{w}_2)$ to ground truth values (v_1, w_1) and (v_2, w_2). Let $\angle(u, v) = \arccos(|u \cdot v|)$ represent angle (or deviation) between two unit vectors u and v.

Angular Resolution: calculates $\mathsf{AngRes} = |\angle(v_1, v_2) - \angle(\hat{v}_1, \hat{v}_2)|$. This measures how similar crossing fibers are in relative direction (from completely aligned to completely orthogonal) compared to the ground truth, and it is the most widely adopted fiber direction devation measure [42, 135, 78].

Weights-Based Eigenvector Deviation: calculates $\mathsf{WEigDev} = \angle(v_1, \hat{v}_1), \angle(v_2, \hat{v}_2)$. This compares the diffusion direction of most dominant fibers and second most dominant fibers to that of the ground truth fibers, assuming correspondence based on weights [143, 78], or calculates the average deviation for all of the fibers at each voxel [122].

Minimum Deviation: calculates the largest and the second largest eigenvector deviation $\mathsf{MinDev} = \min\{\angle(v_1, \hat{v}_1), \angle(v_1, \hat{v}_2)\}$, and $\mathsf{MinDev} = \min\{\angle(v_2, \hat{v}_2), \angle(v_2, \hat{v}_1)\}$. This compares the diffusion direction of the two most dominant observed fibers to those of the ground truth tensor, allowing correspondence by direction [159].

First Eigenvector Deviation: calculates $\mathsf{FirEigDev} = \min\{\angle(v_1, \hat{v}_1), \angle(v_1, \hat{v}_2)\}$. So the first eigenvector v_1 will correspond to the $\hat{v}_i$ that gives the minimum deviation angle, then the second eigenvector v_2 will automatically correspond to another $\hat{v}_i$. This compares the

diffusion direction of either of the two most dominant observed fibers to that of the most dominant ground truth fiber, thus favoring only the most dominant true fiber direction.

Angular resolution (AngRes) is useful when the dominant fiber directions are relatively stable to show the effectiveness of different decomposition algorithms [42, 135, 78], but can be confused by other issues that arise when studying more general types of uncertainty natural to these settings. In particular, it only measures the relative deviation between fibers, not the absolute deviation of each fiber. So, the relative angle could be identical to ground truth, but both directions could rotate some large number of degrees (as in Figure 6.18(a)), and this measure would fail to capture this error.

The absolute deviation measures (WEigDev, MinDev, FirEigDev) are also susceptible when the weights are very similar (e.g., $w_1 \approx w_2$). In these cases, small variations in the sensed data can cause the directions of v_1 and v_2 to rotate large angles, as there may be no strongly dominant diffusion directions. In particular, WEigDev is susceptible to the problem where the weights switch so $v_1 \approx \hat{v}_2$ and $v_2 \approx \hat{v}_1$, in which case WEigDev evaluates to $\angle(v_1, v_2)$, due to the fact that the order of the eigenvalue can be easily flipped under the influence of noise. This phenomenon is observed for instance in second-order diffusion tensors [97], and is illustrated in Figure 6.18(c). A similar scenario can corrupt the FirEigDev where the top two diffusion directions have similar weights, and the most dominant direction in the ground truth is observed to have only the second largest weight, and thus the comparison is flipped again. One problem for MinDev is that the two ground truth dominant directions may always be compared the same observed dominant direction since it always picks up the minimum pair. Furthermore, WEigDev and MinDev are unreliable when the angular resolution is small, because the two dominant directions may be observed as a single direction, thereby observing that the second direction $\hat{v}_2$ is dependent on random noise; see Figure 6.18(b). The second observed direction $\hat{v}_2$ is also susceptible to noise when its true weight w_2 is small.

These scenarios do arise in noisy data; Figure 6.19 shows a comparison between MinDev and WEigDev. The fiber weights were set at 0.8 (1st fiber) 0.2 (2nd fiber); the SNR changes from 50 to 5. The first and second row shows the first eigenvector and second eigenvector deviation correspondingly for MinDev. The third and fourth row shows the first eigenvector and second eigenvector deviation correspondingly for WEigDev. Clearly, minimum deviation reduces the error in both first and eigenvector deviation. However, the ground truth first eigenvector or the second eigenvector may always compare with the same observed eigenvector (the first or the second observed eigenvector direction). For WEigDev,

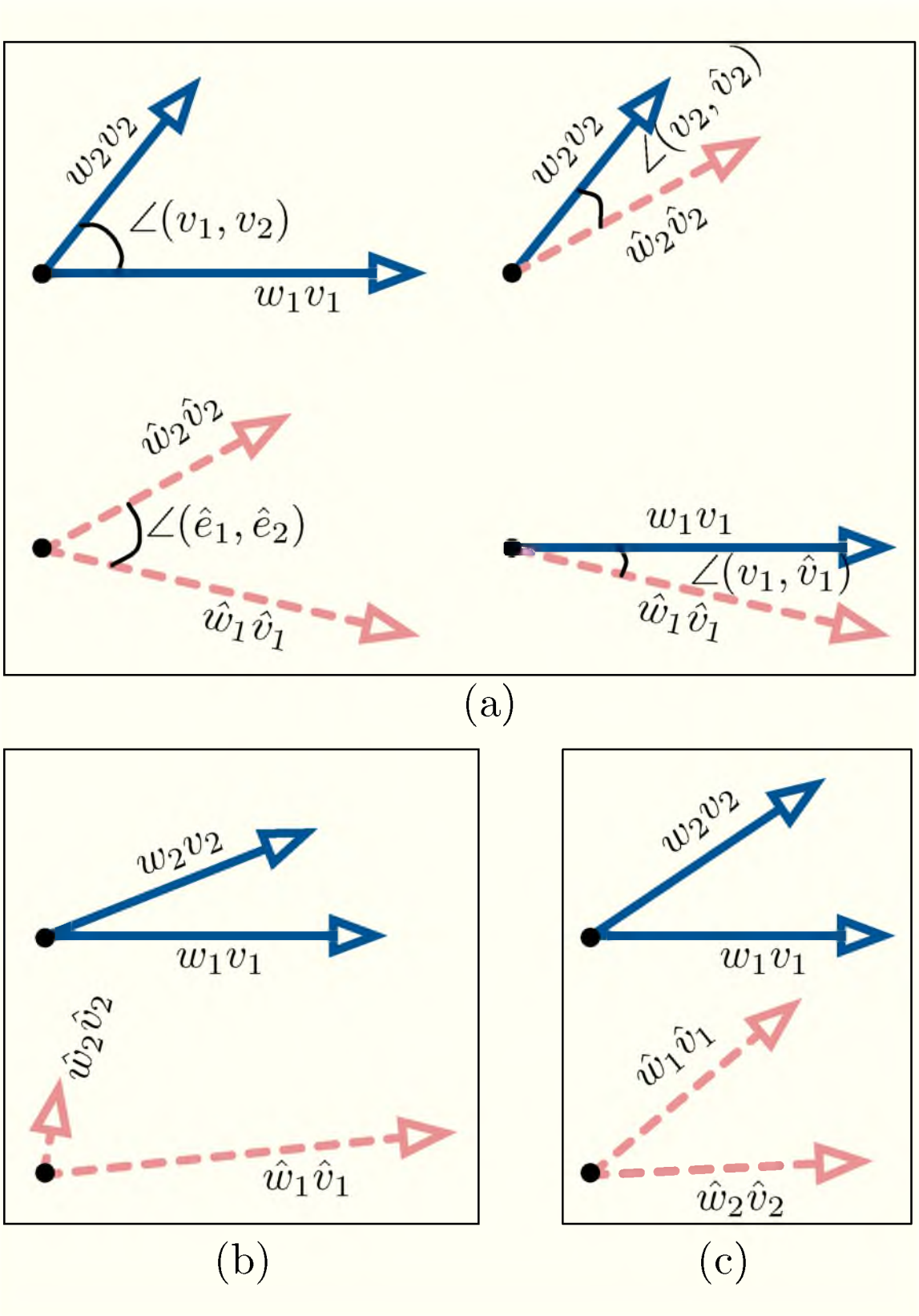

Figure 6.18: Different methods for angle deviation measurement. (a) Measurement of deviations, a difficult case for AngRes. (b) Difficult case for WEigDevand MinDev. (c) Difficult case for WEigDev.

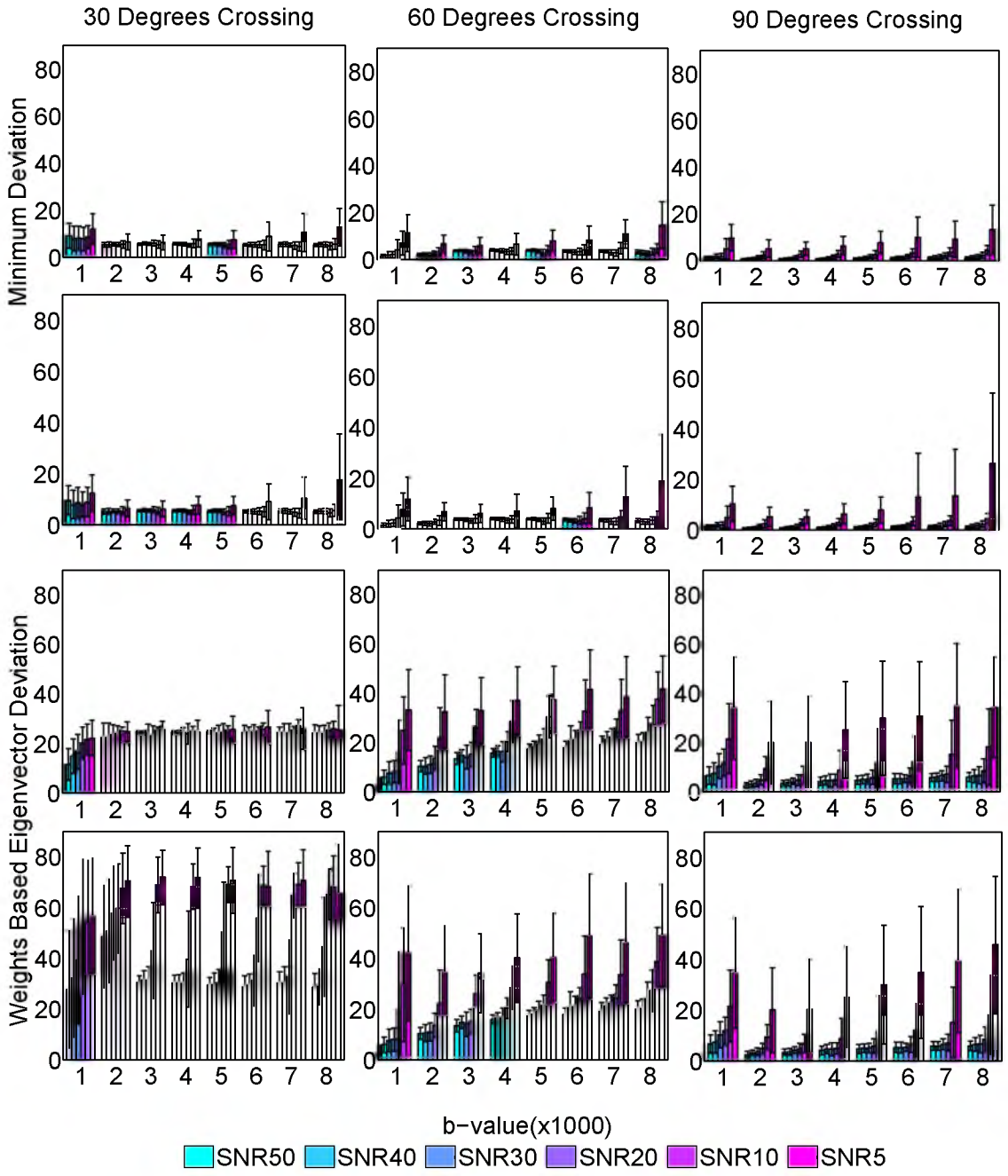

Figure 6.19: The comparison between the MinDev (top two rows, first row is for the largest eigenvector and second row is for the second largest eigenvector) and WEigDev (bottom two rows, third row is for the largest eigenvector and fourth row is for the second largest eigenvector) method to choose the order of eigenvectors. Two fibers crossing at 30, 60, and 90 with the fiber weights of 0.8 (1st fiber) and 0.2 (2nd fiber) were generated.

the mismatch between observed eigenvectors and the true eigenvectors caused a bigger error in both the first eigenvector and the second eigenvector, especially for the smaller crossing angles or the heavier noise level. The reason why smaller crossing angle is even worse is because when the crossing angle is small, the two true directions almost combined into one single direction, which makes the second eigenvector almost like a random vector due to the noise. As far as the authors know, there may not be a rigorously right way to judge the true order of the observed eigenvectors at a small crossing angle or under the influence of a heavy noise. For a three or even more fiber crossing case, it will be even challenging to compare. Thus, we advocate that more careful considerations need to be taken for comparisons based on fiber direction uncertainties, and more focus needs to be put on the study of the diffusion shapes uncertainties, which may be more robust than fiber directions only.

6.6 Conclusions

Representing uncertainty in ODFs is a real and important challenge. In this work, we provide a general and elegant technique to visualize and quantify uncertainty in DW imaging. The key object of our technique is a SIP function generated from a large number of diffusion shapes, associated with different noise realizations of given DW data. The SIP function is constructed by transforming a 3D ODF to a general volume rendering problem using a 1D transfer function to generate 5 layers separated by approximate iso-levels. We found that the SIP function provides a simple, clear, and informative way to study uncertainty, especially in comparison with other techniques.

As future work, we plan to elaborate this technique by using 3D glyphs that combine both diffusion profile information, as well as the fiber orientations and weights, accompanied by appropriate quantification measures. We hope to increase the admittedly slow construction time using a GPU, and plan to incorporate it into an interactive visualization system. We hope this will help to understand better the impact of the different acquisition parameters, and consequently, to design successful HARDI acquisition protocols.

CHAPTER 7

THREE METRICS FOR UNCERTAINTY ANALYSIS AND VISUALIZATION OF DIFFUSION TENSOR IMAGES

Diffusion tensor magnetic resonance imaging (DT-MRI) is an important noninvasive technique for evaluating the three-dimensional white matter structure within the brain. Over time, numerous DT-MRI fiber tracking algorithms that work by integrating along the eigenvector direction(s) of local diffusion tensor fields have been proposed to visualize and quantify the connections between different anatomical regions of the brain. However, because diffusion tensor measurements are affected by many sources of uncertainty, such as noise and imaging artifacts, accumulated uncertainty in fiber orientation along fiber tracks may produce erroneous tracking results. Thus, questions of how to analyze and effectively visualize the accuracy and uncertainty of different diffusion tensor imaging fiber tracking algorithms are important research questions with direct clinical applications in neurological diagnosis and treatment. In this chapter, we propose three metrics to quantify the differences between the results of diffusion tensor magnetic resonance imaging (DT-MRI) fiber tracking algorithms: the area between corresponding fibers of each bundle, the Earth Mover's Distance (EMD) between two fiber bundle volumes, and the current distance between two fiber bundle volumes. We also discuss an interactive fiber track comparison visualization toolkit we have developed based on the three proposed fiber difference metrics and have tested on six widely-used fiber tracking algorithms. To show the effectiveness and robustness of our metrics and visualization toolkit, we present results on both synthetic data and high-resolution monkey brain DT-MRI data. Our toolkit can be used for testing the noise effects on fiber tracking analysis and visualization and to quantify the difference between any pair of DT-MRI techniques, comparing single subjects within an image atlas.

7.1 Introduction

Diffusion tensor magnetic resonance imaging (DT-MRI) is a powerful tool for non-invasive investigation of the reconstruction of white matter pathways. By obtaining diffusion-weighted MR images from multiple locations, a diffusion tensor can be reconstructed which is believed to delineate the local diffusion properties of water molecules in tissue [13]. A number of Diffusion Tensor Imaging (DTI) tractography algorithms, based on classical second-order tensor models [15], two-tensor models [118], higher-order tensor models [74, 135], or q-ball models [149], etc., have been proposed over the last decade. These tracking algorithms fall into two main categories: deterministic tractography [15] or probabilistic tractography [56]. Deterministic tracking algorithms are based on the assumption that the largest eigenvector(s) direction of a diffusion tensor aligns with the dominant fiber orientation(s) in each voxel, while the probabilistic algorithms calculate the probability of a connection between two anatomical regions. The issues of noise, motion, imaging artifacts, or partial volume effects create a certainty degree of uncertainty for both kinds of algorithms and may produce misleading tracking results. However, quantifying and effectively visualizing the accuracy and the uncertainty between results of different fiber tracking algorithms remains a significant challenge.

A first step in quantifying fiber tracking uncertainty is to calculate distances between fibers. Several fiber bundle difference metrics have been proposed [38, 62, 17, 58], most of which use a Euclidean distance measure based upon predefined correspondences. One problem with the distance metric is that it is easily disturbed by the predefined correspondences, with most being overestimated, as shown in Section 7.2. In addition, most difference metrics do not take into account the local fiber directional information and the local fiber probability information, i.e., how many fibers pass through a single voxel, which will overweight the peripheral or tail voxels and ignore the directional information of the local diffusion profile. In this chapter, we proposed three similarity metrics: the area between corresponding fibers of each bundle, the Earth Mover's Distance (EMD) between two fiber bundle volumes, and the current distance between two fiber bundle volumes [85], which can help better quantify differences between fiber bundles and better understand uncertainty associated with fiber tracking algorithms. The first metric still depends on the predefined correspondences, but is more robust than the Euclidean distance metrics. To the best of our knowledge, we are the first group to define an area metric between two fiber bundles. The last two metrics do not depend on any correspondences and the third metric incorporates both the local fiber directional information and the fiber probability information.

Visualization of error and uncertainty is a growing area with important applications in science, engineering, and medicine [80]. However, there are very few works addressing the visualization of uncertainty or the accuracy of tensor fields and specifically of fiber tracking algorithms. A recent paper by Brecheisen et al. [29] studies how to effectively visualize how the stopping criteria of the FACT algorithm (Fiber Assignment by Continuous Tracking) can influence the fiber tracking results. However, this study primarily illustrates the quantification of the difference using a single algorithm and does not provide methods for interalgorithm comparisons. In addition, Brecheisen et al. use a technique in which seed points were placed manually by expert users. Such manual placement can influence the outcome of the fiber tracking algorithm and is somewhat time consuming.

In this chapter, we describe an interactive uncertainty and visualization toolkit. With our toolkit, users can interactively visualize uncertainty and differences between different fiber tracking algorithms. Users can interactively change the fiber tracking algorithm, change the tracking criteria, change how seed points are distributed, and visualize both global and local results. Furthermore, our toolkit provides the ability to track uncertainties within different anatomical regions, easily observe areas of high uncertainty, and interactively explore such high uncertainty regions locally. All of these properties together will give a user more freedom to interactively explore, quantify, and visualize uncertainties within DTI-MR data.

For this study, we use both synthetic DTI data and high-resolution DTI-MR data from a monkey brain. The synthetic DTI data allow us to compare our fiber tracking metrics and toolkit abilities to known, albeit simplified, data, while the monkey brain DTI data allow us to test the effectiveness and robustness of the toolkit with large-scale, high-resolution DTI-MR data.

We conclude that the three metrics defined in this chapter can effectively and robustly quantify the fiber bundle difference due to the effect of noise. Although further validation is needed, our toolkit may also be applied to quantify and interactively visualize the effects of additional artifacts, such as volume averaging.

This chapter is organized as follows. In Section 7.2, we give an overview of related research. In Section 7.3, we describe details about the DT-MRI monkey brain data and synthetic data used in our study. In Section 7.4, we define three fiber similarity measures. In Section 7.5, we present the design of our toolkit and discuss the interactive visualization of fiber track differences for both the synthetic and monkey data sets. In Section 7.6, we summarize our system and its potential use and discuss possible future directions.

7.2 Related Work

Several works were proposed to quantify the difference between fiber bundles mainly for fiber clustering and image registration purposes. Batchelor et al. [17] and Leemans et al. [100] make use of the curvatures and torsions of the fiber bundle to quantify the shape of the fiber tracts or perform rigid image registration. Gerig et al. [58] and Corouge et al. [38, 39] introduce a framework of computing the point-based and arc-length-based statistics along fiber bundles and defined three measure related to the Hausdorff distance. Similarly, O'Donnell et al. [111] proposed a comparison based on the common area of the fiber bundles, and the corresponding points are defined by the arc-length-based coordinate on the mean fiber of the fiber bundle. Using HARDI data, Kezele et al. [88] present a method to extract the white matter fiber tracts mean line by using constrained procrustes analysis. Goodlett et al. [62] put forward a set of volumetric and tract oriented measures for evaluating tract differences: Volumetric Overlap, Point Cloud Divergence, Ellipsoid Distance, and Functional Difference. Maddah et al. [104, 105] defined a Hausdorff similarity measure enhanced with Mahalanobis distance between fiber points and incorporated atlas information subsequently. Manifold learning [112, 156] is applied to embed the fiber bundles into Euclidean or topological spaces to perform clustering. The mean closest distance is also adopted as a similarity measure to perform the embedding, which is similar with the metric defined by Ding et al. [46]. The fiber distance measures, i.e., the distance between corresponding points or corresponding arc-length, distance along the mean fiber, mean closest point distance, etc., are the most popular measures used by the community. However, the distance measures can be easily affected undesirably by a reliance on predefined correspondences. They also fail to take into account the local directional information and the fiber probability information. In two recent publications by Wassermann et al. [155, 154], a Bayesian framework based on Gaussian Processes was proposed, which takes into account prior information about the fiber structure. Unfortunately, this method assumes that the distribution of the fiber point position is Gaussian, which may not always be true.

Although there have been some earlier papers on visualizing the uncertainty associated with vector fields [27, 153, 102, 115, 161] and scalar fields [64], there are very few works addressing the visualization of uncertainty or the accuracy of tensor fields and specifically of fiber tracking algorithms. A probable reason for the lack of papers on visualizing uncertainty of 3D tensor fields is the inherent geometric complexity of tensor fields, which is still an active visualization research area. As mentioned previously, the recent study by [29] provides a way to visualize the influence different criteria have on the fiber tracking results

of the FACT tracking algorithm. In this chapter, we study five different deterministic tractography algorithms: Streamline algorithm, Tensorline algorithm, Tensor Deflection algorithm, Guided algorithm, and Fast Marching algorithm [15, 158, 98, 33, 116], and one stochastic tractography tracking algorithm [56]. For the Streamline algorithm, Tensorline algorithm, Tensor Deflection algorithm, and Guided algorithm, both the interalgorithm and intra-algorithm fiber bundle differences can be visualized interactively on both synthetic DTI data and high-resolution Monkey brain DTI data using corresponding points distance and area between corresponding points metrics.

Concerned with the studies of the comparisons between different algorithms, a validation study, based on the Simultaneous Truth and Performance Level Estimation (STAPLE) algorithm, was done to compare four fiber tracking methods (Fast Marching, Guided Tracking, Streamline Tractography and Stochastic Tractography) by Pujol et al. [124]. However, they only focus on statical analysis and their results are limited. Taylor et al. [141] compared the Streamline method and Fast Marching method based on a synthetic phantom. In this study, they directly add Gaussian noise in the each component of the synthetic diffusion tensor, which is a questionable process due to the Rician distribution [65] of the noise in diffusion-weighted images. On the other hand, neither of these two studies try to visualize the difference in an interactive and effective way.

7.3 Materials and Methods

7.3.1 Data

7.3.1.1 Synthetic Data

The synthetic data used in this chapter were simulated by Numerical Fiber Generator (NFG) [36]. One B0 image ($b = 0s.mm^2$) and 20 diffusion-weighted images ($b = 3000s.mm^2$) were obtained. The image resolution is $0.1mm \times 0.1mm \times 0.1mm$ and the image matrix size is $20 \times 20 \times 20$ voxels.

7.3.1.2 High Resolution Monkey Brain Data

The monkey brain used in this study is the right hemisphere of a whole brain. Imaging experiments were conducted on a Bruker Biospec 7-T horizontal-bore system (Bruker Inc, Billerica, MA). For data acquisition, a standard 3D diffusion-weighted spin-echo sequence was used (TR 375 ms, TE 26 ms, field of view $70 \times 51 \times 51$mm, Matrix $233 \times 170 \times 170$ which yielded an isotropic resolution of 300 microns; b-value is 2,000 s/mm^2).

7.3.1.3 Adding noise

To test the robustness of our toolkit, different levels of artificial Rician noise were added to the synthetic and the monkey brain diffusion-weighted images. Six signal-to-noise (SNR) ratio levels of noise are 96, 48, 32, 24, 19, and 16, which correspond to about 2%, 4%, 6%, 8%, 10%, and 12% measured by the noise mean and divided by the signal mean. To guarantee the distribution of added noise is Rician, we proceed as follows: take the Fourier transform of the diffusion-weighted image, add Gaussian noise in both the real and imaginary part, take the magnitude of the Gaussian noise disturbed complex image, and implement the inverse Fourier transform of the magnitude image to obtain the noisy image. The same procedure was used for both synthetic data and monkey brain data. One issue that needs to be specified is that the smoothed monkey brain data were treated as the ground truth, and different levels of noise were added directly to it. This is because there is no ground truth available for real brain data and the main focus of this chapter is on how to quantify and visualize the uncertainties rather than the noise issue itself.

7.3.2 Fiber Tracking Algorithms and Tracking Parameters

In this study, we implement six algorithms: five deterministic ones, the Streamline, Tensorline, Tensor Deflection (Tend), Guided, and Fast Marching algorithm, and one probabilistic algorithm, Stochastic Tractography.

The Streamline algorithm starts from seed points and integrates along the the major eigenvector direction to form the fiber tracts. The Tensorline algorithm integrates along the following outgoing vector direction:

$$v_{\text{out}} = fe_1 + (1-f)\left((1-g)v_{\text{in}} + gD \cdot v_{\text{in}}\right) \tag{7.1}$$

which is the weighted sum of the major eigenvector direction of the current voxel e_1 and the previous voxel v_{in}, and the deflection term $D \cdot v_{\text{in}}$. Weinstein et al. [158] used a linear anisotropy measure as f, and named the technique the Tensorline algorithm. Lazar et al. [98] extended this idea to set f and g to any user-defined number between 0 and 1; this is the Tend algorithm. It is worth noting that when $f = 1$, both the Tensorline algorithm and the Tensor Deflection algorithms are exactly the same as the Streamline algorithm. The Guided tracking algorithm integrates along the major eigenvector direction while being guided by *a priori* information, which can be anatomical knowledge or fiber tracking results from some other algorithms. The Fast Marching algorithm is based on a fast marching level set method where a front interface propagates in directions normal to itself with a non-negative speed function. From this speed function, three-dimensional time

of arrival maps are generated, which produce the connection paths among brain regions. The Stochastic fiber tracking algorithm calculates the probabilities of connections based on a Bayesian framework. To facilitate the comparisons, we use the same start and end region for all of the six algorithms. We use linear anisotropy (CL) rather than fractional anisotropy (FA) as the anisotropy value for tracking. The reason for this choice is that the tensor shapes with high FA, i.e., disks, do not necessarily have a clear contrast between the major and secondary eigenvalue, in which case major eigenvector direction may easily change by 90 degrees based primarily on noise effects. The step size was chosen to be 0.05 mm for the synthetic data, and 0.15 mm for the monkey brain data, while the stopping criteria was CL=0.1 for both synthetic data and monkey brain data. For all of the six algorithms, only fiber tracts starting from the seed region and ending in the end region are selected for comparison.

7.4 Fiber Similarity Metrics

In this section, we define three distance measures between pairs of fibers A and B, as well as between fiber bundles $\mathrm{c}A = \{A_1, A_2, \ldots\}$ and $\mathrm{c}B = \{B_1, B_2, \ldots\}$. Each fiber is described by a sequence of points, that is fiber $A = \langle a_1, a_2, \ldots \rangle$. We can also represent a fiber A by a piecewise-linear curve defined by segments $a_i a_{i+1}$ between consecutive fiber points. More conveniently, we can just denote a set of voxels that a fiber goes through. For a fiber A, we denote this set of voxels as $\bar{A} = \{\bar{a}_1, \bar{a}_2, \ldots\}$ and for a fiber bundle $\mathrm{c}A$ it is denoted as $\mathrm{c}\bar{A} = \{\bar{a}_1, \bar{a}_2, \ldots\}$. Given a fiber bundle $\mathrm{c}A$, for each voxel $\bar{a}_h$, we can then determine the fraction of fibers that pass through that voxel (the probability), denoted as $P_{\bar{a}_h}$. Additionally, we can calculate the average tangent direction of the fibers that pass through a voxel $\bar{a}_h$, denoted as $T_{\bar{a}_h}$. These quantities will be useful in the distance measures we define for comparing fibers and fiber bundles.

Before we introduce the new measures, we first comment on commonly used distance measures in the literature. Given two fibers A and B, let the *pointwise-order distance* of the common area be defined

$$D_{\mathsf{po}}(A, B) = \sum_{i=1} \|a_i - b_i\| \tag{7.2}$$

Let B_ℓ denote the point on the piecewise-linear curve of fiber B a distance ℓ from the start by arclength, and let $\ell_A(a)$ be the distance from the start of fiber A to a point $a \in A$. Then, let the *corresponding arc-length distance* be defined

$$D_{\mathsf{cal}}(A, B) = \sum_{i=1} \|a_i - B_{\ell_A(a_i)}\| + \sum_{j=1} \|b_j - A_{\ell_B(b_j)}\| \tag{7.3}$$

Let $\phi_B(a)$ be the closest fiber point in B to point a. Then, let the *corresponding closest point distance* be defined

$$D_{\mathsf{ccp}}(A,B) = \sum_{i=1} \|a_i - \phi_B(a_i)\| + \sum_{j=1} \|b_j - \phi_A(b_j)\| \tag{7.4}$$

These measures are illustrated in Figure 7.1 of two fibers A and B. Although these distances may be easy to compute, they typically take the sum or the average of distances between points, which are overestimates or underestimates of the true distances. This is due either to poor predefined correspondences, poor discretization, or a complex local configuration of the fibers or fiber bundles.

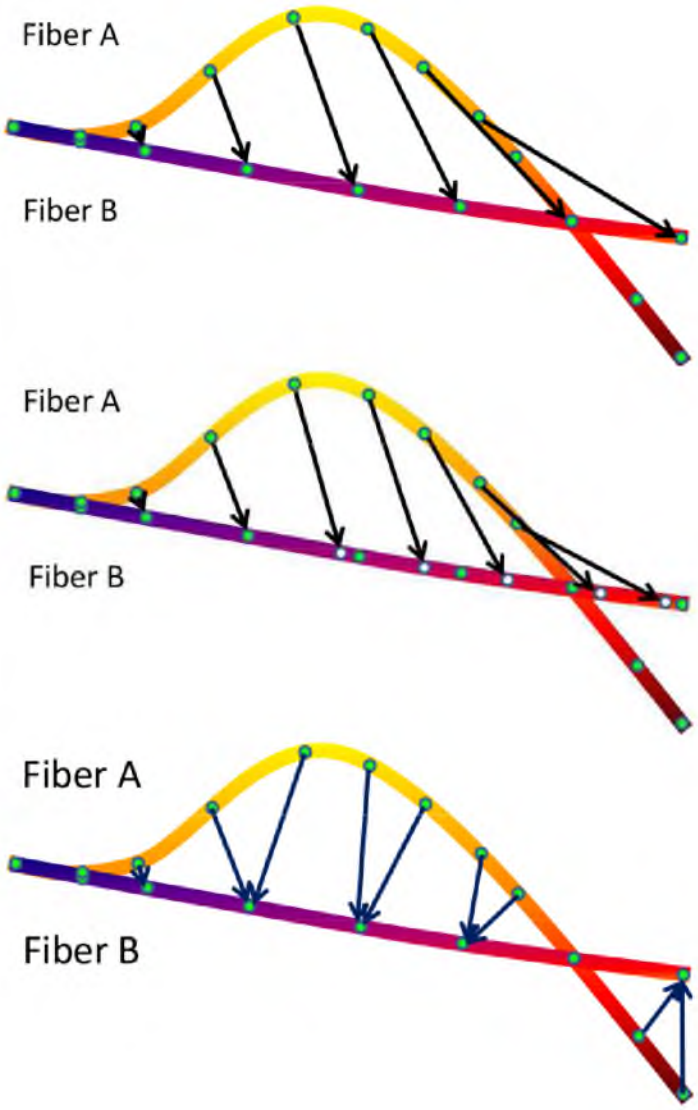

Figure 7.1: Different distances: (top) $D_{\mathsf{po}}(A,B)$, (middle) $D_{\mathsf{cal}}(A,B)$, (bottom) $D_{\mathsf{ccp}}(A,B)$.

For the crossing point of Fiber A and Fiber B in Figure 7.1, the local difference value assigned to this point for any Euclidean distance measure will be zero. Although the spatial locations of the crossing point are the same, the fiber directions at this point are different for Fiber A and Fiber B. As such, the local difference value at this point should not be zero. The area difference metric defined in Section 7.4.1 solves this dilemma. This local area difference metric can help to visualize the local fiber difference in a more robust way based on the spatial information. For the Earth Mover's Distance and the current distance, the predefined correspondences are not needed. Therefore, the problem of poor predefined correspondences, poor discretization, or a complex local configuration of the fibers or fiber bundles can be successfully avoided. Furthermore, when the local fiber probability or the local fiber directional information are taken into account, this will further reduce the bias by only considering the spatial location. Thus, these two global metrics are more applicable for the purpose of quantifying distances accurately.

7.4.1 The Area Between Corresponding Fibers or Corresponding Points

We propose a distance measure $D_{\mathsf{Area}}(A, B)$ that measures the distance between two fibers A and B by the area between them. Let $\mathsf{Area}(a, b, c)$ describe the area of the triangle between points a, b, and c. Let $\psi_B(a_i)$ and $\psi_A(b_j)$ describe the mappings to points in fiber B and A, respectively, defined by the discrete Frèchet correspondence [49]; Figure 7.2 shows how this correspondence looks like for a simple case of two fibers: the closest distance from each point to the other fiber that also preserves the ordering along the fibers. Formally

$$\begin{aligned} D_{\mathsf{Area}}(A, B) = &\sum_{i=1} \sum_{b_j, b_{j+1} \in \psi_B(a_i)} \mathsf{Area}(a_i, b_j, b_{j+1}) \\ &+ \sum_{j=1} \sum_{a_i, a_{i+1} \in \psi_A(b_j)} \mathsf{Area}(b_j, a_i, a_{i+1}) \end{aligned} \tag{7.5}$$

We can also assign a local distance measure at each point $a_i \in A$ as

$$\begin{aligned} D_{\mathsf{Area}}(a_i, B) = &\frac{1}{2}[\frac{1}{2}\mathsf{Area}(a_{i-1}, a_i, \psi_B^-(a_i)) \\ &+ \sum_{b_j, b_{j+1} \in \psi_B(a_i)} \mathsf{Area}(a_i, b_j, b_{j+1}) \\ &+ \frac{1}{2}\mathsf{Area}(a_i, a_{i+1}, \psi_B^+(a_i))], \end{aligned} \tag{7.6}$$

where $\psi_B^-(a_i)$ (resp. $\psi_B^+(a_i)$) is the min (resp. max) index point in $\psi_B(a_i)$. We use multiple terms for each point and divide by two so the local distance is symmetric (from

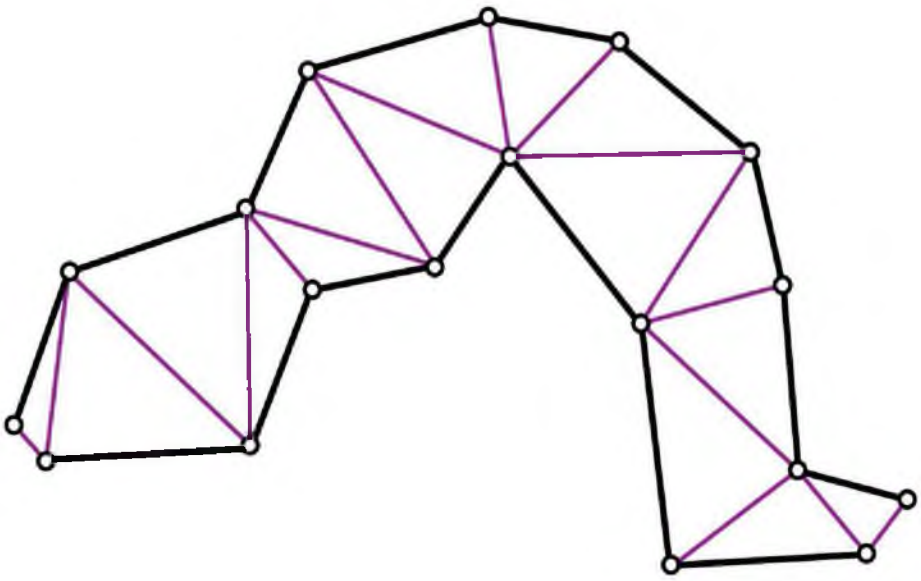

Figure 7.2: The discrete Frèchet correspondence between two fibers.

A to B or B to A) and the sum or the average of local distances is the global distance. Figure 7.3 shows how the local area differences are calculated. For the dark point belonging to the lower fiber, one half of the sum of the red and dark blue area will be assigned as the local area distance measure.

7.4.2 The Earth Mover's Distance

The Earth Mover's Distance, also called the Kantorovich-Wasserstein distance, can be visualized as finding the optimal way to move piles of "earth" or dirt to fill a series of holes, minimizing the total "work" or mass times distance [87]. Based on the voxelsize representation $\bar{cA}$ and $\bar{cB}$ of fiber bundles cA and cB, the Earth Mover's Distance between two fiber bundles is defined as

$$\begin{aligned} EMD(\bar{cA}, \bar{cB}) &= \frac{\sum_{i \in \bar{cA}} \sum_{j \in \bar{cB}} c_{ij} f_{ij}}{\sum_{i \in \bar{cA}} \sum_{j \in \bar{cB}} f_{ij}} \\ &= \frac{\sum_{i \in \bar{cA}} \sum_{j \in \bar{cB}} c_{ij} f_{ij}}{\sum_{j \in \bar{cB}} b_j}, \end{aligned} \tag{7.7}$$

where c_{ij} is the cost to move a unit of supply from $i \in \bar{cA}$ to $j \in \bar{cB}$, and f_{ij} is the flow that minimizes the overall cost

$$\sum_{i \in \bar{cA}} \sum_{j \in \bar{cB}} c_{ij} f_{ij}, \tag{7.8}$$

subject to the following constraints:

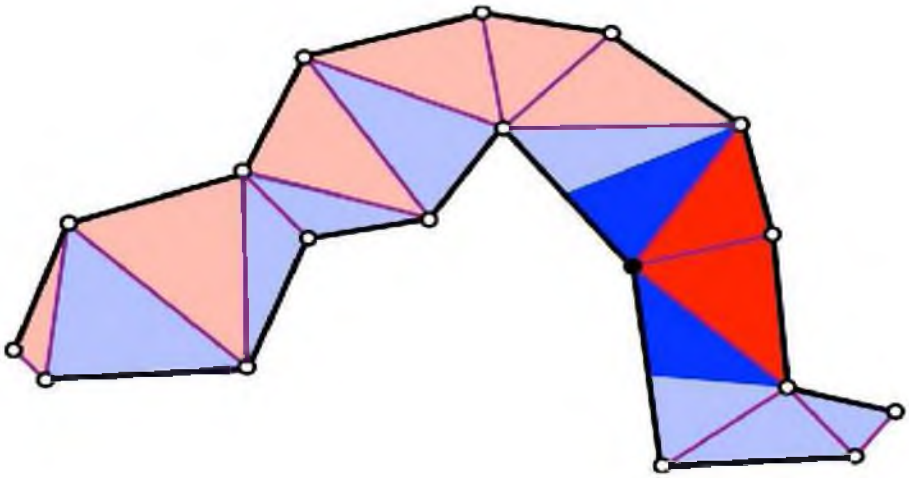

Figure 7.3: The local area distance based on discrete Frèchet correspondence between two fibers.

$$
\begin{aligned}
&f_{ij} \geq 0 \; i \in c\bar{A}, \; j \in c\bar{B}; \\
&\sum_{i \in c\bar{A}} f_{ij} = \bar{b_j} \; j \in c\bar{B}; \\
&\sum_{j \in c\bar{B}} f_{ij} \leq \bar{a_i} \; i \in c\bar{A},
\end{aligned}
\tag{7.9}
$$

where $\bar{a_i}$ is the total supply of supplier i and $\bar{b_j}$ is the total capacity of consumer j. In this case, they both are the probability values at the ith voxel of fiber bundle $c\bar{A}$ and jth voxel of fiber bundle $c\bar{B}$. The cost function c_{ij}, which can be any predefined distance measure in any dimension, is the Euclidean distance between the fiber voxels of two fiber bundles in this chapter. Therefore, the Earth Mover's Distance between two fiber bundles is the minimum effort to redistribute the probability of one fiber bundle to match the other. This measure not only takes into account the Euclidean distance but also considers the fiber probability difference as well.

7.4.3 The Current Distance

The current distance was proposed by Glanués and Vaillant [151] as a measure to compare a broad class of shapes (including point sets, curves, and surfaces) by how they interact with each other. Recently, Durrleman et al. [48] investigated medical application in more depth and showed that the current distance is increasing with decreasing signal-to-noise ratio of the image. The measure can be interpreted as implicitly lifting each shape to a single point in a high (often infinite) dimensional Euclidean space, specifically, a reproducing kernel Hilbert space, where the similarity can be measured as the Euclidean distance. As such, fiber bundles can be interpreted as a set of curves, and the high dimensional vectors corresponding to each curve can be summed to create a single point representing a fiber bundle. This provides a natural distance to compare fiber bundles. Furthermore, Joshi et al. [85] showed that we can approximate the current distance between shapes arbitrarily well by a fine enough discretization. Thus, for computational reasons, we approximate each fiber A by the set of voxels $\bar{A}$ it passes through. Then, the similarity between two fibers can be written as

$$
\kappa(A, B) = \sum_i \sum_j K(a_i, b_j)(T_{\bar{a}_i} \cdot T_{\bar{b}_j}),
\tag{7.10}
$$

where $K(a, b)$ is a kernel function (we use the Gaussian kernel with the bandwidth h the same as the voxel size) and $(T_{\bar{a}_i} \cdot T_{\bar{b}_j})$ is the dot product between two tangent vectors. Now the current distance is defined as

$$
CD(A, B) = \kappa(A, A) + \kappa(B, B) - 2\kappa(A, B).
\tag{7.11}
$$

When using a fiber bundle $\mathrm{c}A = \{A_1, A_2, \ldots, A_n\}$ instead of a single fiber A_i, we can compute the similarity between two fiber bundles as

$$\kappa(\mathrm{c}A, \mathrm{c}B) = \sum_{A_l \in \mathrm{c}A} \sum_{a_i \in A_l} \sum_{B_h \in \mathrm{c}B} \sum_{b_j \in B_h} K(a_i, b_j)(T_{\bar{a}_i} \cdot T_{\bar{b}_j}). \tag{7.12}$$

Because the similarity function κ is a summation over terms, we can accumulate the total number of fibers that pass through each voxel and take their average tangent vector in each voxel, and then we can treat each (now weighted) voxel as a single point of the fiber bundle. The self-similarity of a fiber $\kappa(A, A)$ or of a fiber bundle $\kappa(\mathrm{c}A, \mathrm{c}A)$ can be viewed as a norm of that fiber or fiber bundle, denoting how large that shape is in the high-dimensional vector space. Alternatively, the current distance between two fibers (or fiber bundles) can be seen as the difference in how the fibers act on the underlying space, measured by how they act on each other. This action is described by its local influence in the space by the kernel function K and in the direction it flows through the tangent vector. Thus the current distance measures the difference in how two fibers (or fiber bundles) flow through a given space.

7.5 Results and Discussion

7.5.1 Fiber Track Difference Quantification

Figure 7.4 shows the tracking results of the Streamline, Fast Marching, Guided, and the Stochastic tracking algorithm on synthetic data and on the monkey brain data. Since the Tensorline and the Tend method yield similar results to the Streamline algorithm, we only show the Streamline algorithm result. The Stochastic tracking result is embedded in each of the other three results as a semitransparency isosurface. The colormap shows the local fractional anisotropy (FA) value. The start seed points are shown by the smaller spheres while the ending region points are shown by the larger spheres.

Figure 7.5 shows the average closest distance (D_{ccp}) and average area between corresponding fibers of noise free volume and each level of noisy volume using four algorithms: Streamline, Tensorline, Guided, and Tend algorithm, whose correspondence between fibers or points are easily defined. For the synthetic data, the tracking results from each algorithm are compared with the ground truth, and for the monkey brain data, the tracking results of each algorithm under different noise levels are compared with its own tracking result on the smoothed data without artificial Rician noise. One can see that either the average distance or the average area difference increases with the increasing noise level. The performance of these four algorithms are very similar, except that the Guided tracking algorithm yields slightly different results from the other three methods.

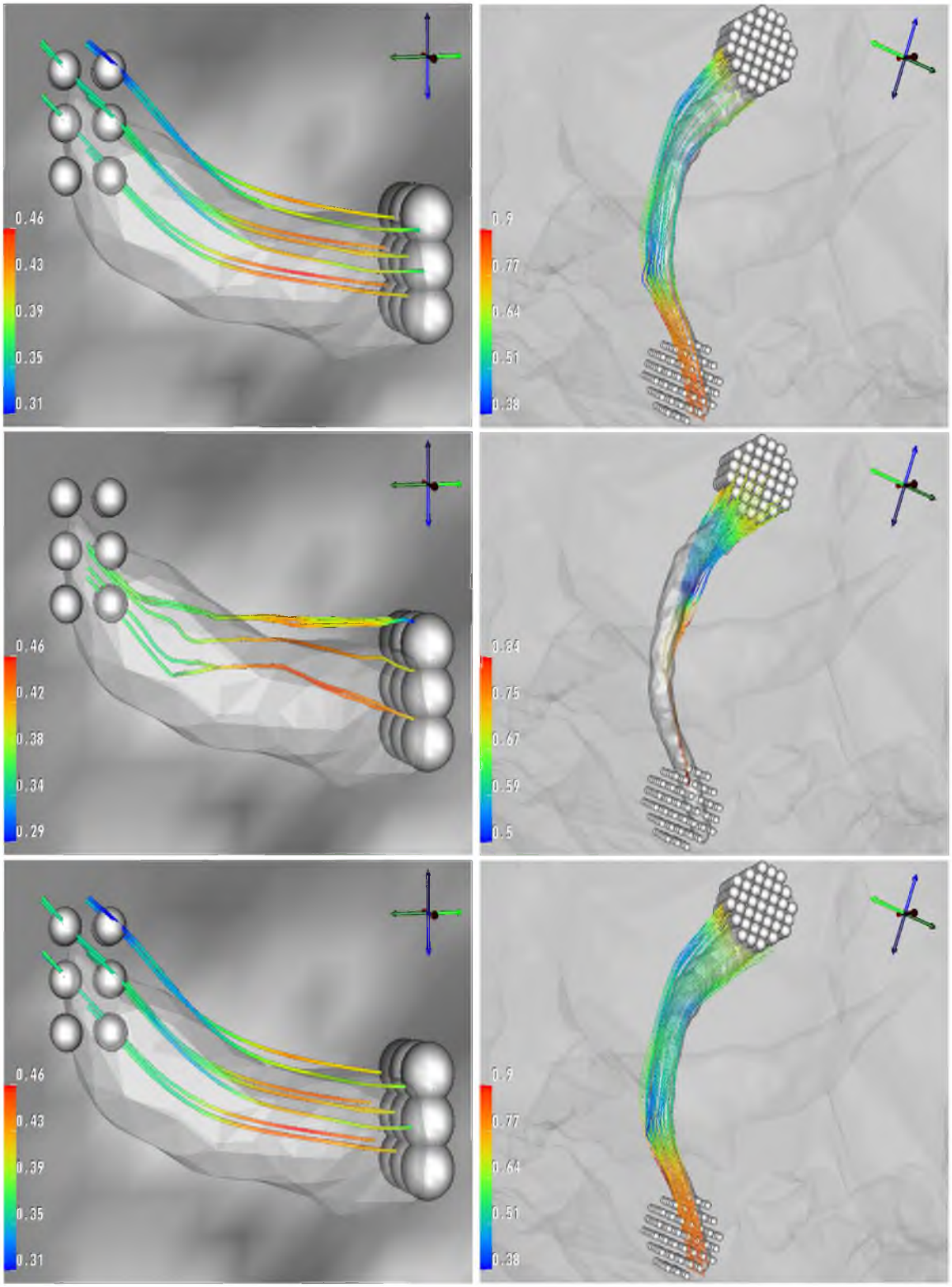

Figure 7.4: The results for synthetic data (left) and monkey brain (right) of four tracking algorithms: Streamline (top), Fast Marching, (middle), Guided tracking (bottom), and Stochastic tracking (embedded as isosurface). The larger spheres show the end points, and the smaller spheres show the starting points.

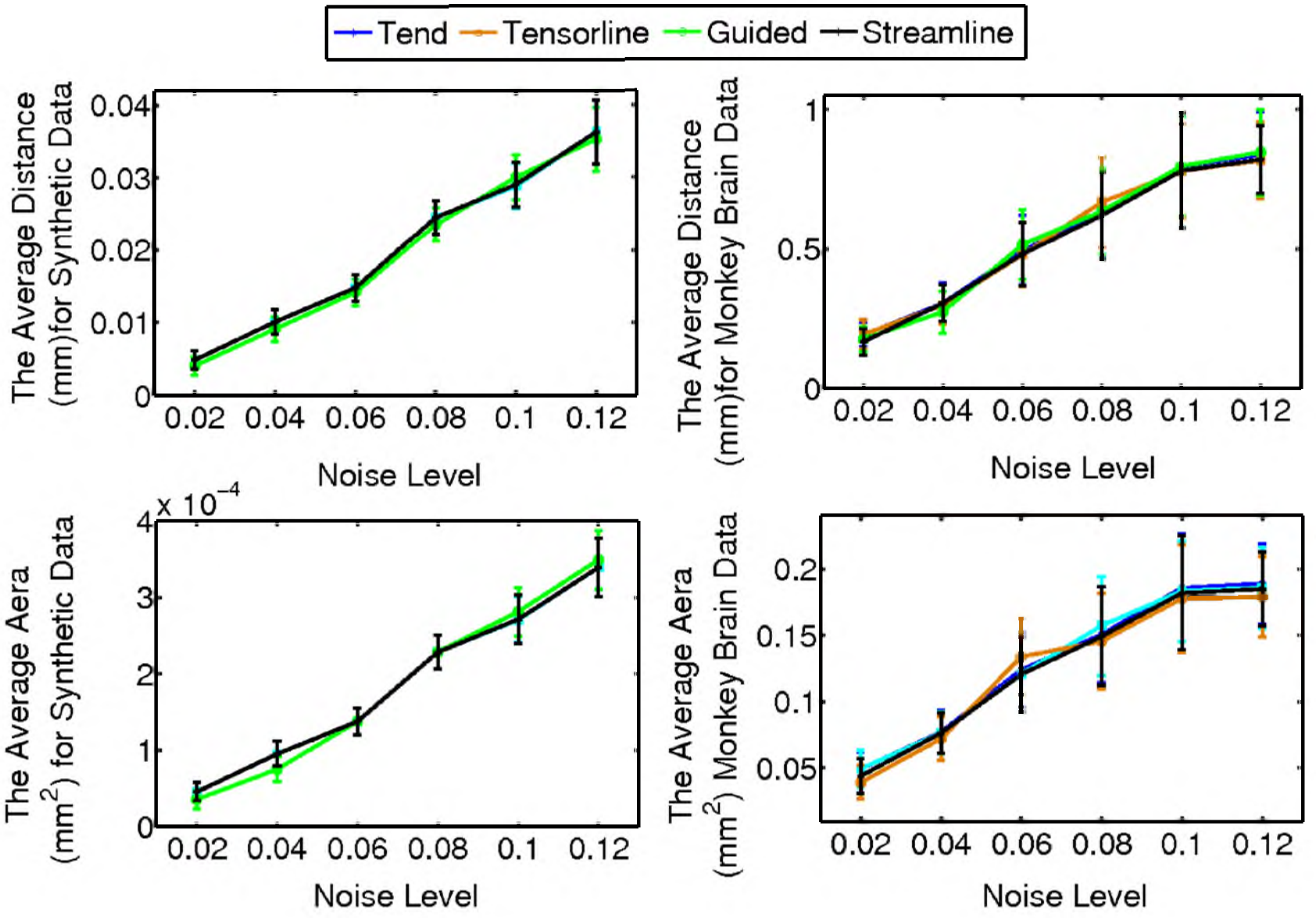

Figure 7.5: The average distance (top) and average area (bottom) between fiber tracking results of the noise free volume and each level of the noisy volume for synthetic data (left) and monkey brain data (right).

The fiber difference quantification using the current distance and the Earth Mover's Distance for both synthetic and monkey brain data are shown in Figure 7.6. The fiber tracks generated using all of the six tracking algorithms are compared with the ground truth or smoothed monkey brain data. We can see that the Stochastic tracking algorithm is very stable at different noise levels and produces the smallest difference for both measures on both data sets, while the performance of the Fast Marching method is not stable and tends to produce quite different results from the the ground truth or smoothed monkey brain data. These comparisons suggest that the Stochastic tracking algorithm is less sensitive to noise, since the noise effects are already accounted for during the fiber tracking process. Furthermore, this suggests that the Stochastic fiber tracking algorithm may be good at finding the major structure of the data set, even at a very low signal-to-noise ratio. The Earth Mover's Distance and current distance can effectively capture the level of uncertainty for most of the algorithms, and the distances tend to increase when the noise level increase.

Although further detailed validation is required, the three metrics put forward in this study show the potential for quantifying the difference between fibers. The area difference is good at local uncertainty visualization and quantification, which will be addressed in the next subsection; however, it needs predefined correspondence. Both the Earth Mover's Distance and the current distance are global measures, but do not need any correspondences. Therefore, the combination of these metrics can help to quantify the uncertainty or accuracy both locally and globally.

7.5.2 DT-MRI Uncertainty Visualization Toolkit

The interactive uncertainty visualization toolkit we designed to visualize the differences between different fiber tracking algorithms, noise levels, and fiber difference metrics was created using the SCIRun problem solving environment (http://www.sci.utah.edu/ software.html). After choosing two DT-MRI volumes to be compared, a user can select fiber tracking algorithms, and tracking parameters such as the stopping criteria, the interpolation method and the integration method, etc. The available tracking algorithms are the six algorithms discussed previously. We note that due to computational costs, the Fast Marching and Stochastic algorithms cannot be currently used in interactive mode. The interpolation methods in the toolkit are nearest neighbor, linear, B-spline, Catmull-Rom, and Gaussian interpolation. An Euler method, as well as fourth-order Runge-Kutta integration methods are used to generate the fiber tracks. The stopping criteria includes the threshold for the length of the fiber, the local anisotropy value, the local curvature, and the number of integration steps. The user can move a widget inside the DT-MRI volume, the position of

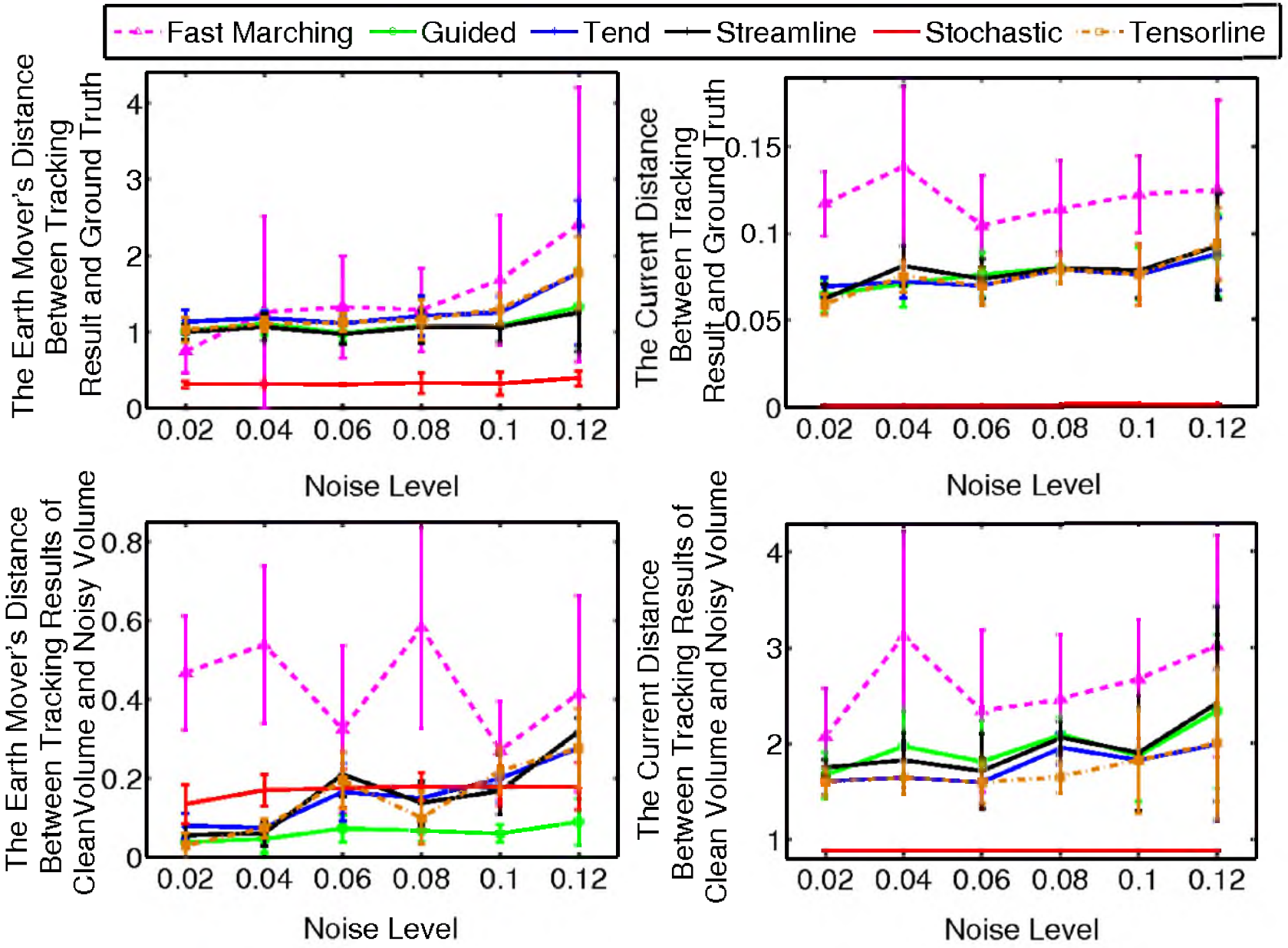

Figure 7.6: The fiber difference quantification using Earth Mover's Distance (left) and current distance (right) on synthetic data (top) and monkey brain data (bottom).

the seed points will be linearly interpolated along the widget, and the local area difference between two preselected volumes will be interactively visualized. Furthermore, the length of the widget, the shape of the widget, and the seed points density can also be changed interactively. Then, correspondence of fibers between any two volumes is defined by whether the fibers come from the same seed points. Figure 7.7 and Figure 7.8 illustrate the global and local visualization windows. The left-hand side shows the interactive uncertainty visualization of the synthetic data, the middle column shows the interactive uncertainty visualization of the monkey brain data, and the right column shows the zoom-in view of the monkey brain data. The fiber tracks are generated using the Streamline algorithm. The global and local difference histograms are shown through an attached UI interface, and the local difference histogram (in red) is updated interactively. Through this interactive UI, the user can easily compare the uncertainty or accuracy of the current fiber track with fiber tracks from different anatomical regions, which helps quickly locate areas with high uncertainty.

In general, the end points of the fibers have a larger uncertainty due to the accumulated tracking error. As shown in Figure 7.7 and Figure 7.8, these areas are highlighted and easily located by the average area metric rather than the average closest distance metric, especially within the monkey brain data. One can also notice that the area with high uncertainty is located to the right and towards the end of the tracking for the monkey brain. While this area is visible in the distance difference visualization, it is more clearly highlighted through the local area difference visualization upon closer inspection at the right column. Taken together, a user can interactively explore, quantify, and visualize uncertainties within DTI-MR data using our uncertainty visualization toolkit. We note that noise is only one of many potential DTMRI uncertainty sources. Imaging artifacts, partial voluming, or even different ber tracking parameters can also produce uncertainties. Although we only focus on the uncertainty associated with different levels of noise, the toolbox we developed in this study can be used as a tool to quantify and visualize any kind of uncertainty.

7.6 Conclusions

In this chapter, we put forward three metrics to quantify the difference between two fiber bundles. The quantification results on synthetic data and the monkey brain data show that the area between corresponding fibers can effectively capture the local or global uncertainty. The Earth Mover's Distance, which considers the local fiber probability, also shows good quantification of the fiber difference. The current distance metric, which considers the

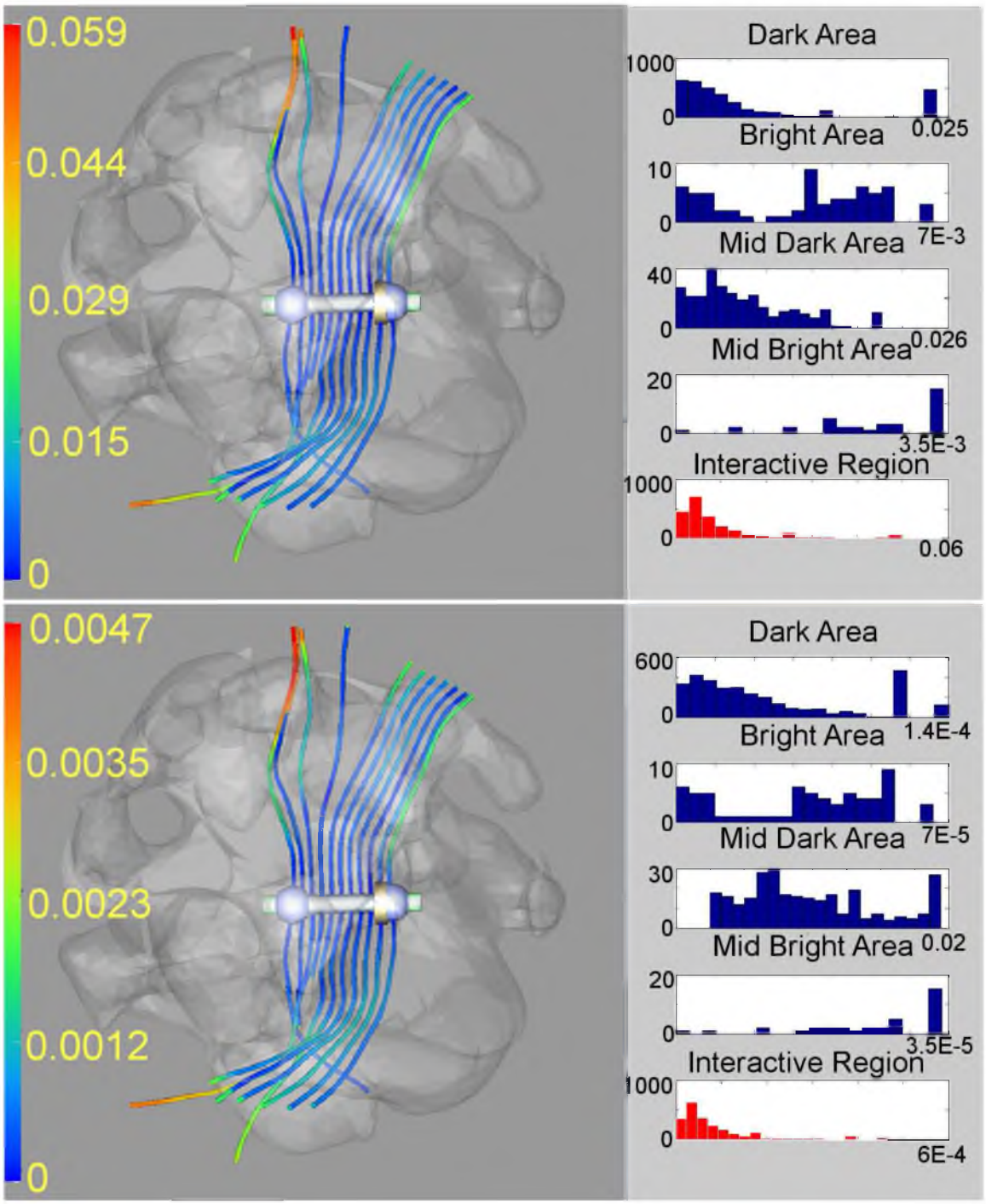

Figure 7.7: The interactive visualization of local closest distance difference (top) and local area difference (bottom) of the synthetic data.

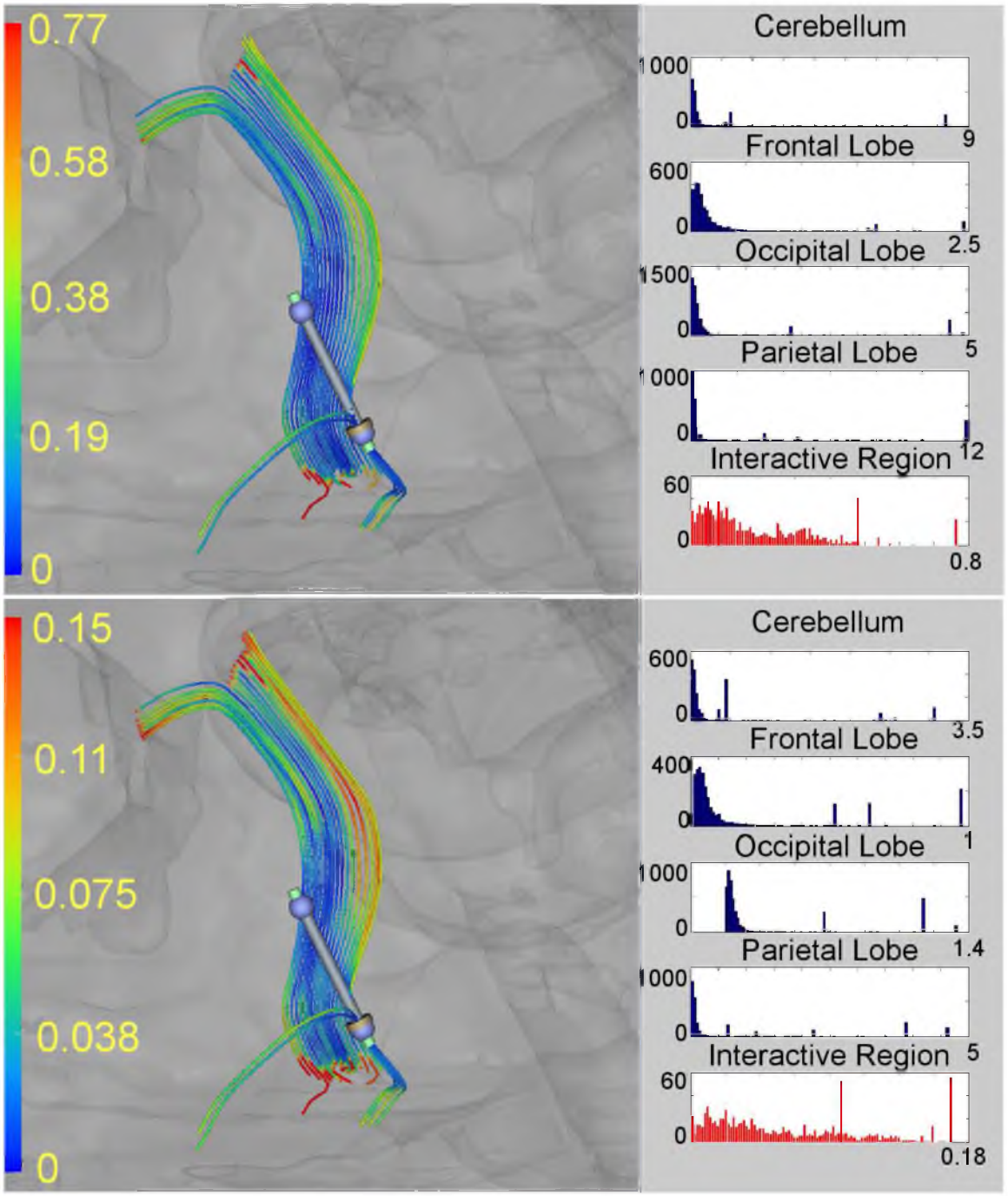

Figure 7.8: The interactive visualization of local closest distance difference (top) and local area difference (bottom) of monkey brain data.

local fiber probability and the local fiber directional information, illustrates the power of quantifying the global uncertainty. Based on all of these metrics, we illustrated an interactive uncertainty visualization toolkit within the SCIRun environment that includes six fiber tracking algorithms that were implemented and associated tracking parameter and noise level options. The location and the density of the seed points can be changed interactively, and most importantly, the uncertainties can be visualized interactively and quantitatively compared with the fiber tracks in different anatomical regions. Thus, our toolkit facilitates fiber tracking algorithm comparison, the quantification and visualization due to the influence of noise or other artifacts, and uncertainty localization.

The metrics we presented here can be easily extended to fiber clustering, and other fiber similarity quantification studies, such as the quantification of the variabilities of the fiber tracking results for different age groups, the comparisons between second-order tensor-based fiber tracking algorithms with q-ball, or higher-order tensor-based fiber tracking algorithms. Also, our interactive quantification and visualization toolkit may potentially be used as a tool for surgical planning, aiding the further improvements of validation of diffusion imaging techniques.

CHAPTER 8

INITIAL RESULTS ON PHANTOM FABRICATION FOR DTI

8.1 Introduction

Despite the successful applications of diffusion imaging technique in patients with schizophrenia [83], brain tumors [129], and Alzheimer's disease [140], it is still a challenging problem to validate fiber direction decomposition algorithms [44, 142, 150, 113, 78, 135] and fiber tracking algorithms [15, 158, 98, 116, 33, 56] due to the absence of a 'gold standard'. Although digital simulations can be implemented to evaluate these methods, these numerical phantoms, based on a number of assumptions, may not be good enough to represent all of the aspects of the real scenario, such as imaging artifacts, eddy current, etc. Physical phantoms, with known well-defined microscopic structure, may help to resolve this dilemma. Existing techniques use silk, hemp, linen, or rayon to generate a phantom, which is hard to reproduce [50]. This chapter reports fabrication of a magnetic resonance imaging (MRI) phantom created by stacking of multiple thin polydimethylsiloxane (PDMS) layers [132, 131]. And this chapter is a joint work with Dr. Bruce Gale's research group, Mechanical Engineering Department, University of Utah.

A proposed design for an MRI phantom is shown in Figure 8.1. Artificial fiber diffusion phantoms have been fabricated using hemp, linen, polyamide, polyester, polyethylene, and rayon [50]. However, it is important to develop artificial phantoms that can be reproduced in order to produce a particular MRI scan result which will help in efforts for the validation of MRI technology. The quality of a phantom is typically dependent on the anisotropy of water diffusion (restricted random Brownian motion of water molecules) and the amount of water in the phantom, which in turn determines the phantom design. Tournier et al. [144] showed a similar design; however, the space between the inner and outer diameters was too large, which limits the amount of water contained in the phantom. The size of the PDMS-based phantom developed in this work was 1.5 cm x 1.5 cm x 0.3 mm to obtain an image of about 15 x 15 voxels of 0.5 mm or 1 mm cubes.

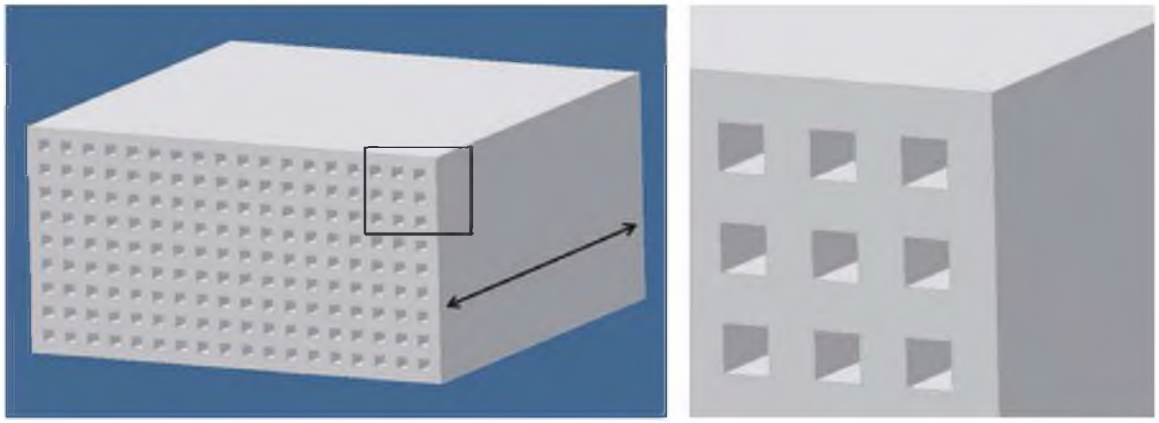

Figure 8.1: A 3D schematic of the envisioned multilayer phantom (not to scale); the targeted dimensions are height: 0.3 mm, width: 1.5 cm, length: 1.5 cm. Each layer is 10 μm thick with 5 μm x 5 μm channels. Spacing between channels (3.6 μm or 8.7 μm) and the orientation (curved channels or straight channels) is varied for each phantom. The major diffusional direction of water molecules is shown by the double-headed arrow. Right figure: A magnified view of the cross-sectional area marked by a black square in the left picture (small microchannels can be observed). With microfabrication techniques, we can reproduce such highly parallel, multilayered microchannels consistently.

PDMS is a popular material for biomedical applications because of its outstanding material properties and the simplicity with which it can be cast onto microstructured molds [106]. The geometry of the phantoms described in this chapter was determined by the requirement of MRI signal-to-noise ratio. During MRI scanning, high signal-to-noise ratios can be achieved if the phantoms with well-aligned microchannels can retain large amounts of water (i.e., a high ratio of combined microchannel volume/phantom volume) and high diffusion anisotropy. Consequently, each phantom layer necessitated a dense array of parallel microchannels and the layers needed to be as thin as could be handled easily and manufactured with high reproducibility. Also, during the MRI measurement interval (ms), the water molecule can diffuse a distance of $5 \sim 20$ microns. Based on these design criteria, the thickness of the PDMS layers was set to $10\mu m$. When the 30 layers are stacked, they are immersed in DI water and then sealed in a PDMS block before being used as a MRI phantom. By taking MR images of this phantom, researchers may be able to validate dMRI techniques.

8.2 MRI Imaging Details

Imaging experiments of the MRI phantom were conducted on a Bruker Biospec 7-T horizontal-bore system (Bruker Inc, Billerica, MA) controlled by Paravision 5.0 software. For data acquisition, a standard 3D diffusion-weighted spin-echo sequence was used (in-plane

resolution is 0.78125 x 0.78125 mm, and the slice thicknesses is 0.5 mm; diffusion-weighting b-value is 800 s/mm^2). For postprocessing, diffusion tensors were computed on a voxel-by-voxel basis via weighted nonlinear least squares fitting to extract the eigenvalues and its corresponding eigenvectors of the tensor matrix.

8.3 Results and Discussion

8.3.1 Device Testing

Figure 8.2 shows the fully fabricated MRI phantoms. The phantoms are immersed in a PDMS reservoir with DI water. The water infusion and air bubble withdrawal was done with 27 G noncoring needles attached to plastic syringes. Figure 8.3 clearly shows no delamination for a stack of 16 layers, an important achievement for successful phantom fabrication.

8.3.2 Diffusion Tensor Images

Figure 8.4 shows the visualization of the B0 image and the diffusion tensor image on a MRI scan of the phantom shown in Figure 8.2 left.

For the diffusion tensor image, the color was coded by the direction of the major eigenvector of each single tensor. If the major eigenvector is aligned with the x direction, the local tensor will be red. If the major eigenvector is aligned with the y direction, the local tensor will be green. If the major eigenvector is aligned with the z direction, the local tensor will be blue. The single tensor with an intermediate major eigenvector direction will be the interpolated color. From this figure, one can see clearly that the phantom was filled with water without any air bubbles (as the white area represents water and dark area represents

Figure 8.2: The pictures of two assembled MRI phantoms (left: with curved channels, right: with straight channels) along with a US quarter coin. Each phantom is placed in a square water reservoir formed by the PDMS cap and PDMS substrate. No air bubble can be seen in the phantom assembly.

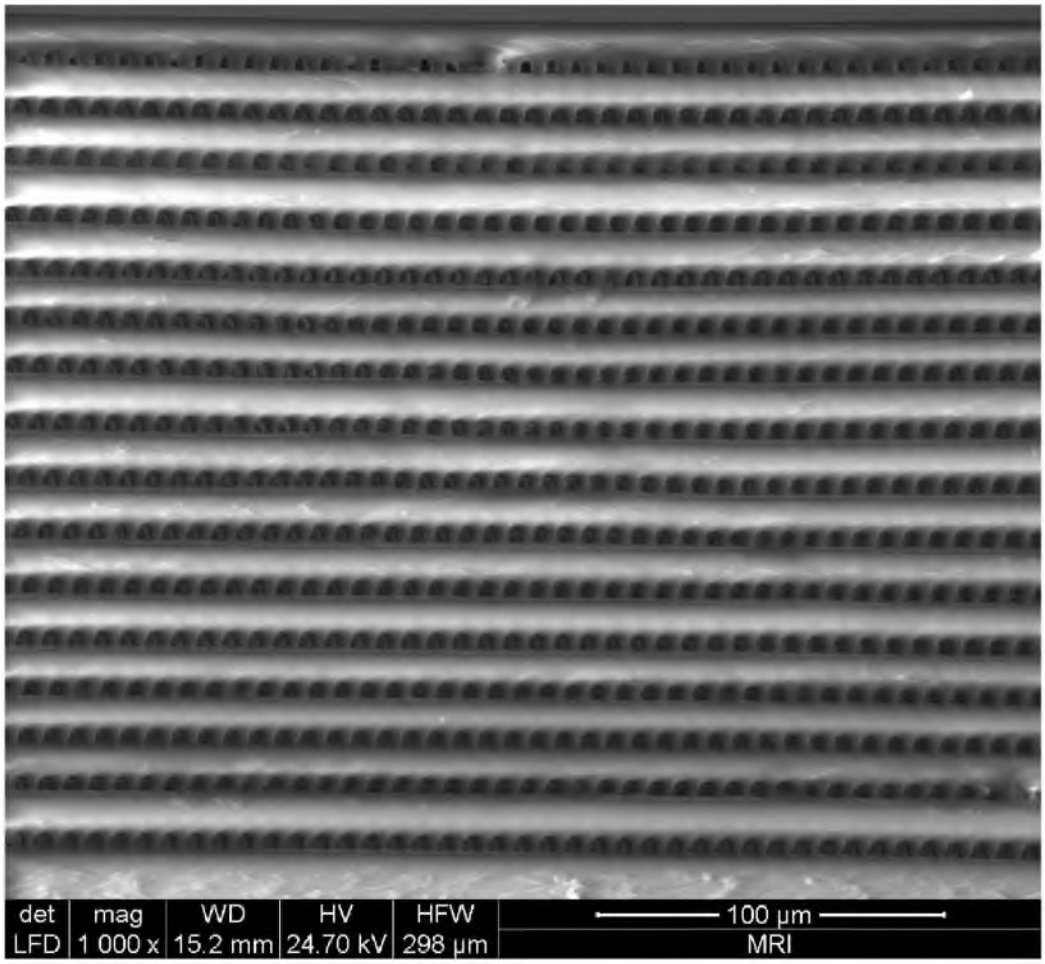

Figure 8.3: Image of a SEM scan of a 16-layer PDMS stack; the stack of layers after curing results in a monolithic structure with no visible interface separating the layers.

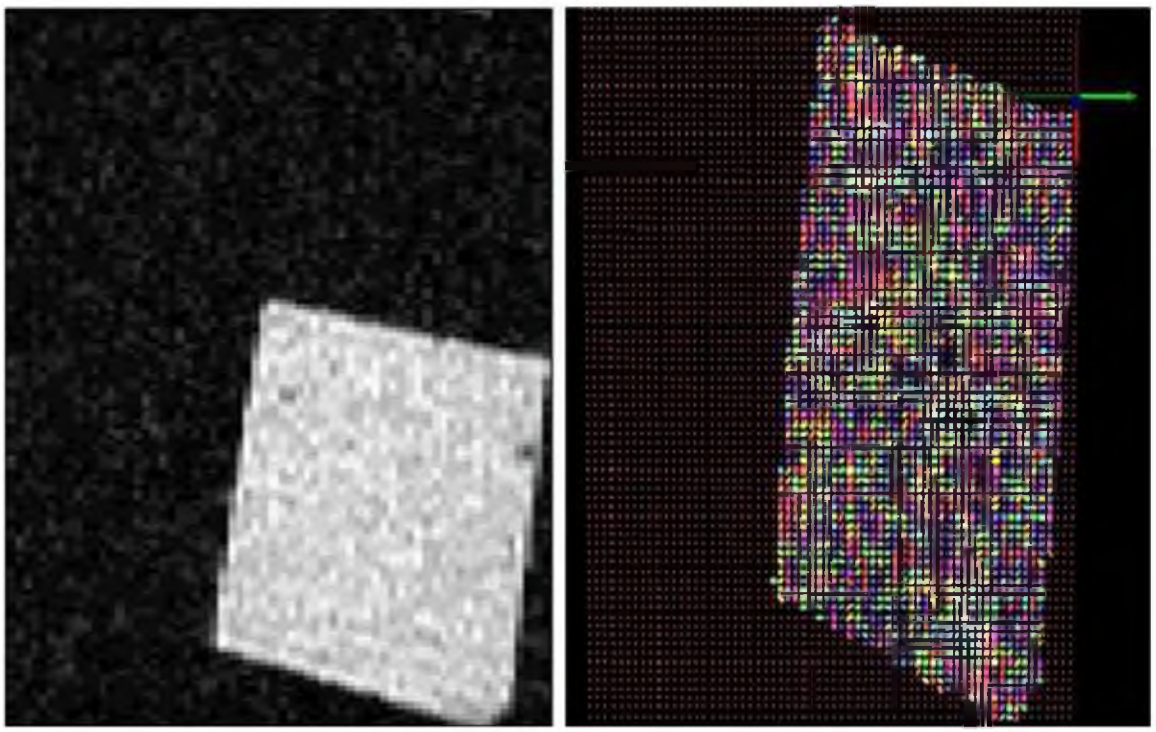

Figure 8.4: The B0 image (left-hand side) and the diffusion tensor image (right-hand side) of the phantom.

absence of water). The water molecule shows a certain degree of anisotropic diffusion. Due to the influence of the voxel size, imaging background noise, and possibly the misalignment between each stack, the anisotropy of each tensor is not as strong as expected. Also, the relative volume of water in the phantom may need to be increased to increase the signal available to the MRI instruments, which may improve the SNR of these diffusion tensor images.

8.4 Conclusions

A simple method of stacking patterned spin-coated $\sim 10\ \mu m$ thick PDMS layers with densely packed microstructures has been developed and demonstrated. The stacking of up to 30 such layers has been performed without the presence of any trapped air bubbles or wrinkles. The unique layer-stacking technique can be used to fabricate MRI diffusion phantoms as gold standards for MRI machines. The stacked layers were easy to handle once assembled and microchannels retained their cross-section, as evidenced by SEM scans.

Overall, we have presented a 30-layer MRI phantom fabricated with microfluidic laminates. A high signal-to-noise ratio during phantom scanning requires high water content inside the phantom channels, a significant challenge. Optimal dimensions and arrangements

for the MRI phantom still need to be developed to improve the function of the phantom, though the methods presented here provide sufficient function to fabricate a physical phantom that can generate better MRI signal, which will be used for dMRI validation and scanner calibration.

CHAPTER 9

CONCLUSIONS AND FUTURE WORK

9.1 Conclusions

In this dissertation, we have explored different aspects of diffusion MRI. The first part of the dissertation (Chapter 4 and Chapter 5) was devoted to developing reconstruction and decomposition techniques for high angular resolution diffusion imaging (HARDI). These techniques are the basis for the uncertainty analysis and visualization discussed in this dissertation. The techniques developed here rely upon higher-order tensor decompositions which enable accurate estimation of the fiber orientations and the volume fractions. In Chapter 4, we have discussed a reconstruction technique which is based on a two-step optimization process. First, an ODF is fitted to the data in each voxel. Then, a CP decomposition is applied to the ODF and decomposes it into a sum of rank-1 tensors which represent single white matter fibers. These rank-1 tensors provide information on the fiber orientations and the volume fractions. In Chapter 5, the ODF estimation and the fiber orientations extraction are combined into one optimization problem such that the fiber parameters are extracted directly from the data, allowing better estimation accuracy. Both approaches were tested on synthetic as well as *in vivo* data and show robust performance.

Various parameters influence the reconstruction accuracy and introduce uncertainty to the estimated ODFs. Therefore, the second part of this dissertation was devoted to analyzing and visualizing the uncertainty in HARDI introduced by different parameters such as the b-value and the SNR. In Chapter 6, the uncertainty is studied at the voxel level by using ensembles of ODFs. By applying volume rendering techniques to ensembles of 3D ODF glyphs, denoted *SIP functions* of *diffusion shapes*, we could elucidate the complex heteroscedastic structural variation in these objects. These variations correspond to the uncertainty which is quantified here by the *certain volume ratio* that measures the volume fraction of these shapes and is consistent across all noise levels.

In Chapter 7, the uncertainty is studied at the global level by integrating the fiber orientations to fiber tracts that present white matter pathways of the brain. The uncertainty

is quantified here by measuring variations between fiber tracts using different metrics such as the Earth Mover's Distance (EMD). An interactive fiber tracts comparison visualization toolkit is also developed here. It is based on three different metrics between fibers and tested on six widely-used fiber tracking algorithms.

Phantoms, and in particular physical phantoms, are essential for testing reconstruction techniques and quantifying uncertainty on known ground-truth. In Chapter 8, we described our research on building a physical phantom using multiple thin polydimethy lsiloxane (PDMS) layers with microchannels.

9.2 Future Work

Currently, diffusion MRI is mainly used as a powerful research modality for studying brain development and brain-related diseases [83, 129, 140]. In order to extend its application to clinical uses such as disease diagnostics and surgery planning, fast and accurate acquisition schemes and image reconstruction techniques have to be developed.

Compressed sensing techniques are widely used now to accelerate the measurement time by undersampling the Fourier coefficients in k-space or reducing the number of gradient orientations [109, 108]. The impact of these undersampling techniques on the accuracy of the reconstructed ODFs as well as the fiber orientations is still an open research problem which has to be explored. The uncertainty analysis and visualization techniques developed in this dissertation may be useful in studying this problem. In addition, to accelerate reconstruction algorithms, fast implementations using GPUs and parallel computing have to be considered [94, 107]

In Chapter 7, we presented an interactive fiber track comparison and visualization tool. There is room for further improvement. One possible future direction is the parameter free fiber tracking, which contains as few as possible parameters. And it may be possible to adopt some learning approaches to automatically learn the parameters needed for fiber tracking. The metrics defined in Chapter 7 can be extended to fiber clustering, and other fiber similarity quantification studies, such as the quantification of the variabilities of the fiber tracking results for different age groups, the comparisons between second-order tensor-based fiber tracking algorithms with q-ball, or higher-order tensor-based fiber tracking algorithms.

Fitting the right model to the data is essential for precise estimation of the fiber orientations and accurate tractography results. In Chapter 4 and Chapter 5, we described a heuristic selection criterion which is based on the volume fractions (fiber weight). However, the question of what is the best model for selecting the number of fiber compartments in each voxel is an open problem. Recent methods rely on Support Vector Machine (SVM)

[133] as well as multidimensional scalar measures [122]. However, these approaches are based on local diffusion properties and do not take into account spatial information which may improve the results.

There are various sources of uncertainty in DTI/HARDI processing, such as noise, imaging artifacts, partial voluming, eddy currents, b-value, and reconstruction modality. In this dissertation, I mainly focused on the noise and the b-value impacts. This work may be extended to include other sources of uncertainty.

REFERENCES

[1] Abramowitz, M., and Stegun, I. A. *Handbook of Mathematical Functions* (1972).

[2] Aganj, I., Lenglet, C., and Sapiro, G. ODF maxima extraction in spherical harmonic representation via analytical search space reduction. In *MICCAI'10* (2010), vol. 6361 of *LNCS*, pp. 84–91.

[3] Alexander, D. C. Maximum entropy spherical deconvolution for diffusion MRI. In *IPMI'05* (2005), vol. 3565 of *LNCS*, pp. 76–87.

[4] Alexander, D. C., Barker, G. J., and Arridge, S. R. Detection and modeling of non-gaussian apparent diffusion coefficient profiles in human brain data. *Magnetic Resonance in Medicine 48*, 2 (2002), 331–340.

[5] Anderson, A. W. Measurement of fiber orientation distributions using high angular resolution diffusion imaging. *Magnetic Resonance in Medicine 54*, 5 (2005), 1194–1206.

[6] Andrews, G. E., Askey, R., and Roy, R. *Special Functions* (1999).

[7] Assemlal, H. E., Tschumperléa, D., and Brun, L. Efficient and robust computation of PDF features from diffusion MR signal. *Medical Image Analysis 13* (2009), 715–729.

[8] Assemlal, H.-E., Tschumperl, D., Brun, L., and Siddiqi, K. Recent advances in diffusion mri modeling: Angular and radial reconstruction. *Medical Image Analysis 15*, 4 (2011), 369–396.

[9] Atkinson, K. Numerical integration on the sphere. *J. Austral. Math. Soc. 23* (1982), 332–347.

[10] Barmpoutis, A., Hwang, M. S., Howland, D., Forder, J. R., and Vemuri, B. C. Regularized positive-definite fourth-order tensor field estimation from DW-MRI. *NeuroImage 45*, 1 (2009), 153–162.

[11] Barmpoutis, A., Jian, B., and Vemuri, B. C. Adaptive kernels for multi-fiber reconstruction. In *IPMI'09* (2009), vol. 5636 of *LNCS*, pp. 338–349.

[12] Barmpoutis, A., and Vemuri, B. C. A unified framework for estimating diffusion tensors of any order with symmetric positive-definite constraints. In *ISBI* (2010), pp. 1385–1388.

[13] Basser, P., Mattiello, J., and Lebihan, D. Estimation of the effective self-diffusion tensor from the NMR spin echo. *Journal of Magnetic Resonance, Series B 103* (1994), 247–254.

[14] Basser, P., and Pajevic, S. Spectral decomposition of a 4th-order covariance tensor: Applications to diffusion tensor MRI. *Signal Processing 87* (2007), 220–236.

[15] Basser, P., Pajevic, S., Pierpaoli, C., Duda, J., and Aldroubi, A. In vivo fiber tractography using DT-MRI data. *Magnetic Resonance in Medicine 44*, 4 (2000), 625–632.

[16] Basu, S., Fletcher, P. T., and Whitaker, R. Rician noise removal in diffusion tensor MRI. In *MICCAI* (2006), LNCS, pp. 117–125.

[17] Batchelor, P., Calamante, F., Tournier, J.-D., Atkinson, D., Hill, D. L. G., and Connelly, A. Quantification of the shape of fiber tracts. *Magnetic Resonance in Medicine 55 Pt 3* (2006), 894–903.

[18] Beaulieu, C. The basis of anisotropic water diffusion in the nervous system - a technical review. *NMR in Biomedicine 15*, 7-8 (2002), 435–455.

[19] Behrens, T., Berg, H. J., Jbabdi, S., Rushworth, M., and Woolrich, M. Probabilistic diffusion tractography with multiple fibre orientations: What can we gain? *NeuroImage 34*, 1 (2007), 144 – 155.

[20] Behrens, T. E. J., Woolrich, M. W., Jenkinson, M., Johansen-Berg, H., Nunes, R. G., Clare, S., Matthews, P. M., Brady, J. M., and Smith, S. M. Characterization and propagation of uncertainty in diffusion-weighted mr imaging. *Magnetic Resonance in Medicine 50*, 5 (2003), 1077–1088.

[21] Bello, L., Gambini, A., Castellano, A., Carrabba, G., Acerbi, F., Fava, E., Giussani, C., Cadioli, M., Blasi, V., Casarotti, A., Papagno, C., Gupta, A. K., Gaini, S., Scotti, G., and Falini, A. Motor and language dti fiber tracking combined with intraoperative subcortical mapping for surgical removal of gliomas. *NeuroImage 39*, 1 (2008), 369–382.

[22] Berman, J., Chung, S., Mukherjee, P., Hess, C., Han, E., and Henry, R. Probabilistic streamline q-ball tractography using the residual bootstrap. *NeuroImage 35* (2008), 215–222.

[23] Berman, J. I., Berger, M. S., Chung, S., Nagarajan, S. S., and Henry, R. G. Accuracy of diffusion tensor magnetic resonance imaging tractography assessed using intraoperative subcortical stimulation mapping and magnetic source imaging. *Journal of Neurosurgery 107* (2007), 488–494.

[24] Berman, J. I., Mukherjee, P., Partridge, S. C., Miller, S. P., Ferriero, D. M., Barkovich, A. J., Vigneron, D. B., and Henry, R. G. Quantitative diffusion tensor mri fiber tractography of sensorimotor white matter development in premature infants. *NeuroImage 27*, 4 (2005), 862–871.

[25] Bloembergen, N., Purcell, E. M., and Pound, R. V. Relaxation effects in nuclear magnetic resonance absorption. *Phys. Rev. 73* (Apr 1948), 679–712.

[26] Bloy, L., and Verma, R. On computing the underlying fiber directions from the diffusion orientation distribution function. In *MICCAI'08* (2008), vol. 5241 of *LNCS*, pp. 1–8.

[27] Botchen, R., Weiskopf, D., and Ertl, T. Texture-based visualization of uncertainty in flow fields. *IEEE Visualization Conference* (2005), 647 – 654.

[28] Brachat, J., Comon, P., Mourrain, B., and Tsigaridas, E. P. Symmetric tensor decomposition. *Linear Algebra and Its Applications 433*, 11-12 (2010), 1851–1872.

[29] Brecheisen, R., Vilanova, A., Platel, B., and Romeny, B. T. H. Parameter sensitivity visualization for dti fiber tracking. *IEEE Transactions on Visualization and Computer Graphics 15*, 6 (2009), 1441–1448.

[30] Bro, R., and Kiers, H. A. L. A new efficient method for determining the number of components in parafac models. *J. of Chemometrics 17* (2003), 274–286.

[31] Carr, H. Y., and Purcell, E. M. Effects of diffusion on free precession in nuclear magnetic resonance experiments. *Phys. Rev. 94* (May 1954), 630–638.

[32] Chen, Y., Guo, W., Zeng, Q., Yan, X., Huang, F., Zhang, H., He, G., Vemuri, B., and Liu, Y. Estimation, smoothing, and characterization of apparent diffusion coefficient profiles from high angular resolution dwi. vol. 1, pp. I588–I593.

[33] Cheng, P., Magnotta, V., Wu, D., Nopoulos, P., Moser, D., Paulsen, J., Jorge, R., and Andreasen, N. Evaluation of the gtract diffusion tensor tractography algorithm: A validation and reliability study. *NeuroImage 31*, 3 (2006), 1075–1085.

[34] Cho, K.-H., Yeh, C. H., Tournier, J. D., Chao, Y. P., Chen, J. H., and Lin, C. P. Evaluation of the accuracy and angular resolution of q-ball imaging. *NeuroImage 42*, 1 (2008), 262–271.

[35] Chung, S., Lu, Y., and Henry, R. G. Comparison of bootstrap approaches for estimation of uncertainties of DTI parameters. *NeuroImage 33* (2006), 531–541.

[36] Close, T., Tournier, J. D., Calamante, F., Johnston, L., Mareels, I., and Connelly, A. A software tool to generate simulated white matter structures for the assessment of fibre-tracking algorithms. *NeuroImage 47*, 4 (2009), 1288–1300.

[37] Comon, P., Luciani, X., and de Almeida, A. L. F. Tensor decompositions, alternating least squares and other tales. *J. of Chemometrics 23* (2009), 393–405.

[38] Corouge, I., Fletcher, P. T., Joshi, S., Gouttard, S., and Gerig, G. Fiber tract-oriented statistics for quantitative diffusion tensor MRI analysis. In *Proceedings Medical Image Computing and Computer Aided Intervention (MICCAI)* (Palm Springs, California, 2005), pp. 131–139.

[39] Corouge, I., Gouttard, S., and Gerig, G. A statistical shape model of individual fiber tracts extracted from diffusion tensor MRI. In *Proceedings Medical Image Computing and Computer Aided Intervention (MICCAI)* (Rennes Saint Malo, France, 2004), pp. 671–679.

[40] Dell'Acqua, F., Rizzo, G., Scifo, P., Clarke, R. A., Scotti, G., and Fazio, F. A model-based deconvolution approach to solve fiber crossing in diffusion-weighted mr imaging. *IEEE Transactions on Biomedical Engineering 54*, 3 (2007), 462–472.

[41] Demiralp, C., and Laidlaw, D. Tract-based probability densities of diffusivity measures in DT-MRI. In *MICCAI* (Beijing, China, 2010), pp. 542–549.

[42] Descoteaux, M. *High angular resolution diffusion MRI: from local estimation to segmentation and tractography.* Phd thesis, University of Nice Sophia Antipolis, 2008.

[43] Descoteaux, M., Angelino, E., Fitzgibbons, S., and Deriche, R. Apparent diffusion coefficients from high angular resolution diffusion imaging: Estimation and applications. *Magnetic Resonance in Medicine 56*, 2 (2006), 395–410.

[44] Descoteaux, M., Angelino, E., Fitzgibbons, S., and Deriche, R. Regularized, fast, and robust analytical q-ball imaging. *Magnetic Resonance in Medicine 58*, 3 (2007), 497–510.

[45] Descoteaux, M., Deriche, R., Bihan, D. L., Mangin, J.-F., and Poupon, C. Diffusion propagator imaging: using laplace's equation and multiple shell acquisitions to reconstruct the diffusion propagator. *IPMI 21* (2009), 1–13.

[46] Ding, Z., Core, J. C., and Anderson, A. W. Classification and quantification of neuronal fiber pathways using diffusion tensor MRI. *Magnetic Resonance in Medicine 49 Pt 4* (2003), 716–721.

[47] Dubois, J., Hertz-Pannier, L., Cointepas, G. D.-L. Y., and Bihan, D. L. Assessment of the early organization and maturation of infants' cerebral white matter fiber bundles: A feasibility study using quantitative diffusion tensor imaging and tractography. *NeuroImage 30*, 4 (2006), 1121–1132.

[48] Durrleman, S. *Statistical models of currents for measuring the variability of anatomical curves, surfaces and their evolution.* Thĕse de sciences (phd thesis), Universitĕ de Nice-Sophia Antipolis, March 2010.

[49] Eiter, T., and Mannila, H. Computing discrete Frèchet distance. Tech. Rep. CD-TR94/64, Christian Doppler Laboratory for Expert Systems, TU Vienna, Austria, 1994.

[50] Fieremans, E., Deene, Y. D., Delputte, S., zdemir, M. S., Achten, E., and Lemahieu, I. The design of anisotropic diffusion phantoms for the validation of diffusion weighted magnetic resonance imaging. *Physics in Medicine and Biology 53*, 19 (2008), 5405–5419.

[51] Fillard, P., Pennec, X., Arsigny, V., and Ayache, N. Clinical dt-mri estimation, smoothing, and fiber tracking with log-euclidean metrics. *IEEE Transactions on Medical Imaging 26*, 11 (2007), 1472–1482.

[52] Fonteijn, H., Verstraten, F., and Norris, D. Probabilistic inference on q-ball imaging data. *IEEE Trans. Med. Imaging 26* (2007), 1515–1524.

[53] Frank, L. Anisotropy in high angular resolution diffusion-weighted MRI. *Magn. Reson. Med. 45* (2001), 935–939.

[54] Frank, L. R. Characterization of anisotropy in high angular resolution diffusion-weighted mri. *Magnetic Resonance in Medicine 47*, 6 (2002), 1083–1099.

[55] Freidlin, R. Z., zarslan, E., Komlosh, M. E., Chang, L.-C., Koay, C. G., Jones, D. K., and Basser, P. J. Parsimonious model selection for tissue segmentation and classification applications: A study using simulated and experimental dti data. *IEEE Transactions on Medical Imaging 26*, 11 (2007), 1576–1584.

[56] Friman, O., Farnebäck, G., and Westin, C. A bayesian approach for stochastic white matter tractography. *IEEE Transactions on Medical Imaging 25*, 8 (2006), 965–978.

[57] Friman, O., and Westin, C. F. Uncertainty in white matter fiber tractography. In *MICCAI* (2005), pp. 107–114.

[58] Gerig, G., Gouttard, S., and Corouge, I. Analysis of brain white matter via fiber tract modeling. vol. 26 VI, pp. 4421–4424.

[59] Ghosh, A., Wassermann, D., and Deriche, R. A polynomial approach for maxima extraction and its application to tractography in hardi. In *IPMI'11* (2011), vol. 6801 of *LNCS*, pp. 723–734.

[60] Glenn, O. A., Henry, R. G., amd Patrick C. Chang, J. I. B., Miller, S. P., Vigneron, D. B., and Barkovich, A. J. Dti-based three-dimensional tractography detects differences in the pyramidal tracts of infants and children with congenital hemiparesis. *Journal of Magnetic Resonance Imaging 18*, 6 (2003), 641–648.

[61] Gonzalez, J. E. I., Thompson, P. M., Zhao, A., and Tu, Z. Modeling diffusion-weighted MRI as a spatially variant gaussian mixture: application to image denoising. *Medical Physics 38* (2011), 4350–4364.

[62] Goodlett, C. Computation of statistics for populations of diffusion tensor images. *Computation of Statistics for Populations of Diffusion Tensor Images* (2009).

[63] Grant, M., and Boyd, S. CVX: Matlab software for disciplined convex programming, version 1.21. `http://cvxr.com/cvx`, Oct. 2010.

[64] Grigoryan, G., and Rheingans, P. Point-based probabilistic surfaces to show surface uncertainty. *IEEE Transactions on Visualization and Computer Graphics 10*, 5 (2004), 564–573.

[65] Gudbjartsson, H., and Patz, S. The Rician distribution of noisy MRI data. *Magnetic Resonance in Medicine 34*, 6 (1995), 910–914.

[66] Haacke, E. M., Brown, R. W., Thompson, M. R., and Venkatesan, R. *magnetic resonance imaging-physical principles and sequence design.* John Wiley and Sons, 1999.

[67] Hagen, E. V. D., and Henkelman, R. Orientational diffusion reflects fiber structure within a voxel. *Magnetic Resonance in Medicine 48*, 3 (2002), 454–459.

[68] Hahn, E. L. Spin echoes. *Phys. Rev. 80* (Nov 1950), 580–594.

[69] Hahn, H. K., amd C. Nimsky, J. K., Rexilius, J., and Peitgen, H. Uncertainty in diffusion tensor based fibre tracking. *Medical Technologies in Neurosurgery 98* (2006), 33–41.

[70] Haroon, H., Morris, D., Embleton, K., Alexander, D., and Parker, G. Using the model-based residual bootstrap to quantify uncertainty in fiber orientations from q-ball analysis. *IEEE Trans. Med. Imaging. 28* (2009), 535–550.

[71] Håstad, J. Tensor rank is NP-complete. *J. Algorithms 11* (1990), 644–654.

[72] Hess, C. P., Mukherjee, P., Han, E. T., Xu, D., and Vigneron, D. B. Q-ball reconstruction of multimodal fiber orientations using the spherical harmonic basis. *Magnetic Resonance in Medicine 56*, 1 (2006), 104–117.

[73] Hlawitschka, M. *Efficient Visualization of Tensor Fields with Application to Magnetic Resonance Data*. PhD thesis, Leipzig University, 2008.

[74] Hlawitschka, M., and Scheuermann, G. Hot-lines: Tracking lines in higher order tensor fields. *Proceedings of the IEEE Visualization Conference* (2005), 27–34.

[75] Hosey, T., Williams, G., and Ansorge, R. Inference of multiple fiber orientations in high angular resolution diffusion imaging. *Magn Reson Med 54* (2005), 1480–1489.

[76] Irfanoglu, M., Koay, C. G., Pajevic, S., Machiraju, R., and Basser, P. Diffusion tensor field registration in the presence of uncertainty. *MICCAI 12* (2009), 181–189.

[77] Jian, B., Vemuri, B. C., and Özarslan, E. A mixture of wisharts (mow) model for multifiber reconstruction. *Visualization and Processing of Tensor Fields 1* (2009), 39–56.

[78] Jiao, F., Gur, Y., Johnson, C. R., and Joshi, S. Detection of crossing white matter fibers with high-order tensors and rank-k decompositions. In *IPMI* (2011), vol. 6801 of *LNCS*, pp. 538–549.

[79] Jiao, F., Phillips, J. M., Stinstra, J., Kruger, J., Kommaraju, R. V., Hsu, E., Korenberg, J., and Johnson, C. R. Metrics for uncertainty analysis and visualization of diffusion tensor images. In *MIAR* (Bejing, China, 2010), pp. 179–190.

[80] Johnson, C. R. Top scientific visualization research problems. *IEEE Transactions on Computer Graphics and Applications 24* (Aug, 2004), 13–17.

[81] Jones, D. Determining and visualizing uncertainty in estimates of fiber orientation from diffusion tensor MRI. *Magnetic Resonance in Medicine 49*, 1 (2003), 7–12.

[82] Jones, D. K. Tractography gone wild: Probabilistic fibre tracking using the wild bootstrap with diffusion tensor MRI. *IEEE Trans. Med. Imaging 27*, 9 (2008), 1268–1274.

[83] Jones, D. K., Catani, M., Pierpaoli, C., Reeves, S., Shergill, S., O'Sullivan, M., Golesworthy, P., Horsfield, P. M. M., Simmons, A., Williams, S., and Howard, R. Age effects on diffusion tensor magnetic resonance imaging tractography measures of frontal cortex connections in schizophrenia. *Human Brain Mapping 27*, 3 (2006), 230–238.

[84] Jones, D. K., and Pierpaoli, C. Confidence mapping in diffusion tensor magnetic resonance imaging tractography using a bootstrap approach. *Magn. Reson. Med. 53* (2005), 1143–1149.

[85] Joshi, S., Kommaraju, R. V., Phillips, J. M., and Venkatasubramanian, S. Comparing distributions and shapes using the kernel distance. pp. 47–56.

[86] Kaden, E., Knsche, T., and Anwander, A. Parametric spherical deconvolution: Inferring anatomical connectivity using diffusion mr imaging. *NeuroImage 37*, 2 (2007), 474–488.

[87] Kantorovich, L. On a problem of monge. *Uspekhi Mat. Nauk. 3*, 2 (1948), 225–226.

[88] Kezele, I., Poupon, C., Perrin, M., Cointepas, Y., Kouby, V. E., Poupon, F., and Mangin, J.-F. Mean q-ball strings obtained by constrained procrustes analysis with point sliding. In *Proceedings Medical Image Computing and Computer Aided Intervention (MICCAI)* (New York, 2008), pp. 1034–1041.

[89] Kiers, H. A. L. Towards a standardized notation and terminology in multiway analysis. *J. of Chemometrics 14* (2000), 105–122.

[90] Kim, D.-J., Kim, I.-Y., Jeong, S.-O., , and Park, H.-J. Evaluation of Bayesian tensor estimation using tensor coherence. *Physics in Medicine and Biology 54* (2009), 3785–3802.

[91] Kindlmann, G. Superquadric tensor glyphs. In *Proceedings of IEEE TVCG/EG Symposium on Visualization* (May 2004), pp. 147–154.

[92] Kolda, T. G., and Bader, B. W. Tensor decompositions and applications. *SIAM Review 51* (2009), 455–500.

[93] Kolda, T. G., and Mayo, J. R. Shifted power method for computing tensor eigenpairs. arXiv:1007.1267v2 [math.NA], Feb 2011.

[94] Kondratieva, P., Krger, J., and Westermann, R. The application of gpu particle tracing to diffusion tensor field visualization. pp. 73–78.

[95] Laidlaw, D., Ahrens, E., Kremers, D., Avalos, M., Readhead, C., and Jacobs, R. Visualizing diffusion tensor images of the mouse spinal cord. In *IEEE Visualization* (October 1998), pp. 127–134.

[96] Lathauwer, L. D., Moor, B. D., , and Vandewalle, J. On the best rank-1 and rank-$(r_1, r_2, \ldots, r_n)$ approximation of higher-order tensors. *SIAM Journal on Matrix Analysis and Applications 21* (2000), 1324–1342.

[97] Laun, F. B., Schad, L. R., Klein, J., and Stieltjes, B. How background noise shifts eigenvectors and increase eigenvalues in DTI. *Magn. Reson. Mater. Phy. 22* (2009), 151–158.

[98] Lazar, M., Weinstein, D. M., Tsuruda, J. S., Hasan, K., Arfanakis, K., Meyerand, M. E., Badie, B., Rowley, H., Haughton, V., Field, A., and Alexander, A. White matter tractography using diffusion tensor deflection. *Human Brain Mapping 18*, 4 (2003), 306–321.

[99] Lazara, M., and Alexandera, A. L. Bootstrap white matter tractography (boot-trac). *NeuroImage 24* (2005), 524–532.

[100] Leemans, A., Sijbers, J., Backer, S. D., Vandervliet, E., and Parizel, P. Multiscale white matter fiber tract coregistration: A new feature-based approach to align diffusion tensor data. *Magnetic Resonance in Medicine 55*, 6 (2006), 1414–1423.

[101] Liang, Z., and Lauterbur, P. C. *Principles of Magnetic Resonance Imaging.* IEEE press, 1999.

[102] Lodha, S. K., Pang, A., Sheehan, R. E., and Wittenbrink, C. M. Uflow: Visualizing uncertainty in fluid flow. pp. 249–254.

[103] Löffler, M., and Phillips, J. M. Shape fitting of point sets with probability distributions. In *Proceedings of 17th Annual European Symposium on Algorithms* (2009).

[104] Maddah, M., Grimson, W., Warfield, S. K., and Wells, W. M. A unified framework for clustering and quantitative analysis of white matter fiber tracts. *Medical Image Analysis 12*, 2 (2008), 191–202.

[105] Maddah, M., Zöllei, L., Grimson, W. E. L., Westin, C.-F., and Wells, W. M. A mathematical framework for incorporating anatomical knowledge in DT-MRI analysis. In *Biomedical Imaging: From Nano to Macro, 2008. ISBI 2008. 5th IEEE International Symposium on Biomedical Imaging* (Paris, France, 2008), ISBI 2008, pp. 105–108.

[106] McDonald, J.C., W. G. Poly(dimethylsiloxane) as a material for fabricating microfluidic devices. *Accounts of Chemical Research 35*, 7 (2002), 491–499.

[107] McGraw, T., and Nadar, M. Stochastic dt-mri connectivity mapping on the gpu. *IEEE Transactions on Visualization and Computer Graphics 13*, 6 (2007), 1504–1511.

[108] Menzel, M. I., Tan, E. T., Khare, K., Sperl, J. I., King, K. F., Tao, X., Hardy, C. J., and Marinelli, L. Accelerated diffusion spectrum imaging in the human brain using compressed sensing. *Magn. Reson. Med.* (2011), 1901–1903.

[109] Michailovich, O., R. Y. D. S. Spatially regularized compressed sensing for high angular resolution diffusion imaging. *IEEE Transactions on Medical Imaging 30*, 5 (2011), 1100–1115.

[110] Moseley, M. E., Cohen, Y., Kucharczyk, J., Mintorovitch, J., Asgari, H. S., Wendland, M. F., Tsuruda, J., and Norman, D. Diffusion-weighted mr imaging of anisotropic water diffusion in cat central nervous system. *Radiology 176*, 2 (1990), 439–445.

[111] O'Donnell, L., Westin, C., and Golby, A. Tract-based morphometry for white matter group analysis. *NeuroImage 45 Pt 3* (2009), 832–844.

[112] O'Donnell, L. J., and Westin, C.-F. Automatic tractography segmentation using a high-dimensional white matter atlas. *IEEE Transactions on Medical Imaging 26 Pt 11* (2007), 1562–1575.

[113] Özarslan, E., Shepherd, T. M., Vemuri, B. C., Blackband, S. J., and Mareci, T. H. Resolution of complex tissue microarchitecture using the diffusion orientation transform (DOT). *NeuroImage 31*, 3 (2006), 1086–1103.

[114] Pajevic, S., and Basser, P. Parametric and non-parametric statistical analysis of DT-MRI data. *J. Magn. Reson. 161* (2003), 1–14.

[115] Pang, A., Wittenbrink, C., and Lodha, S. Approaches to uncertainty visualization. *Visual Computer 13*, 8 (1997), 370–390.

[116] Parker, G., Wheeler-Kingshott, C., and Barker, G. Estimating distributed anatomical connectivity using fast marching methods and diffusion tensor imaging. *IEEE Transactions on Medical Imaging 21*, 5 (2002), 505–512.

[117] Partridge, S. C., Mukherjee, P., Berman, J. I., Henry, R. G., Miller, S. P., Lu, Y., Glenn, O. A., Ferriero, D. M., Barkovich, A. J., and Vigneron, D. B. Tractography-based of quantitation of diffusion tensor imaging parameters in white matter tracts of preterm newborns. *Journal of Magnetic Resonance Imaging 22*, 4 (2005), 467–474.

[118] Peled, S., Friman, O., Jolesz, F., and Westin, C. Geometrically constrained two-tensor model for crossing tracts in dwi. *Magnetic Resonance Imaging 24*, 9 (2006), 1263–1270.

[119] Perrin, M., Poupon, C., Cointepas, Y., Rieul, B., Golestani, N., Pallier, C., Rivière, D., Constantinesco, A., Bihan, D. L., and Mangin, J. Fiber tracking in q-ball fields using regularized particle trajectories. 52–63.

[120] Pierpaoli, C., and Basser, P. Toward a quantitative assessment of diffusion anisotropy. *Magnetic Resonance in Medicine 36* (1996), 893–906.

[121] Poupon, C., Rieul, B., Kezele, I., Perrin, M., F, F. P., and Mangin, J. New diffusion phantoms dedicated to the study and validation of high-angular-resolution diffusion imaging HARDI models. *Magn Reson Med 60*, 6 (2008), 1276–1283.

[122] Prckovska, V. High angular resolution diffusion imaging processing and visualization. *High Angular Resolution Diffusion Imaging Processing and Visualization* (2010).

[123] Prckovska, V., Roebroeck, A. F., Pullens, W., Vilanova, A., and Romeny, B. M. T. H. Optimal acquisition schemes in high angular resolution diffusion weighted imaging. *LNCS 5242*, vol. 2 (2008), 9–17.

[124] Pujol, S., Magnotta, V., Siebenthal, J. D., Kubicki, M., Hayes, K., Westin, C., Lemaire, J., Kikinis, R., Gollub, R., and 3rd., W. W. Towards validation of dti tractography: Statistical analysis of the differences observed among tractography algorithms.

[125] Qi, L., Yu, G., and Wu, E. Higher order positive semidefinite diffusion tensor imaging. *SIAM J. Imaging Sci. 3* (2010), 416–433.

[126] Ramirez-Manzanares, A., Rivera, M., Vemuri, B. C., Carney, P., and Mareei, T. Diffusion basis functions decomposition for estimating white matter intravoxel fiber geometry. *IEEE Transactions on Medical Imaging 26*, 8 (2007), 1091–1102.

[127] Rhyne, T.-M. Exploring visualization theory. *IEEE Computer Graphics and Applications 31*, 3 (2011), 6–7.

[128] Risholm, P., Pieper, S., Samset, E., and 3rd., W. M. W. Summarizing and visualizing uncertainty in non-rigid registration. In *MICCAI* (Beijing, China, 2010), pp. 554–561.

[129] Roberts, T. P., Liu, F., Kassner, A., Mori, S., and Guha, A. Fiber density index correlates with reduced fractional anisotropy in white matter of patients with glioblastoma. *American Journal of Neuroradiology 26*, 9 (2005), 2183–2186.

[130] Salvador, R., Pea, A., Menon, D. K., Carpenter, T. A., Pickard, J. D., and Bullmore, E. T. Formal characterization and extension of the linearized diffusion tensor model. *Human Brain Mapping 24*, 2 (2005), 144–155.

[131] Samuel, R., Sant, H. J., Jiao, F., Johnson, C. R., and Gale, B. K. Fabrication of a mri standardization device from stacking highly patterned thin pdms layers. *MicroTAS* (2010), 1901–1903.

[132] Samuel, R., Sant, H. J., Jiao, F., Johnson, C. R., and Gale, B. K. Microfluidic laminate-based phantom for diffusion tensor-magnetic resonance imaging. *Journal of Micromechanics and Microengineering 21*, 9 (2011), 095027.

[133] Schnell, S., Saur, D., Kreher, B., Hennig, J., Burkhardt, H., and Kiselev, V. Fully automated classification of hardi in vivo data using a support vector machine. *NeuroImage 46*, 3 (2009), 642–651.

[134] Schultz, T., and Kindlmann, G. A maximum enhancing higher-order tensor glyph. *Computer Graphics Forum 29*, 3 (2010), 1143–1152.

[135] Schultz, T., and Seidel, H.-P. Estimating crossing fibers: A tensor decomposition approach. *IEEE Transactions on Visualization and Computer Graphics 14*, 6 (2008), 1635–1642.

[136] Schultz, T., Westin, C.-F., and Kindlmann, G. Multi-diffusion-tensor fitting via spherical deconvolution: A unifying framework. In *MICCAI* (2010), T. Jiang, N. Navab, J. Pluim, and M. Viergever, Eds., vol. 6361 of *LNCS*, pp. 673–680.

[137] Schwartzman, A. Random ellipsoids and false discovery rates: Statistics for diffusion tensor imaging data. PhD dissertation.

[138] Stegeman, A., and Comon, P. Subtracting a best rank-1 approximation may increase tensor rank. *Linear Algebra and its Applications 433* (2010), 1276–1300.

[139] Sullivan, E. V., Adalsteinsson, E., and Pfefferbaum, A. Selective age-related degradation of anterior callosal fiber bundles quantified in vivo with fiber tracking. *Cerebral Cortex 16*, 7 (2006), 1030–1039.

[140] Taoka, T., Iwasaki, S., Sakamoto, M., Nakagawa, H., Fukusumi, A., Myochin, K., Hirohashi, S., Hoshida, T., and Kichikawa, K. Diffusion anisotropy and diffusivity of white matter tracts within the temporal stem in alzheimer disease: Evaluation of the "tract of interest" by diffusion tensor tractography. *American Journal of Neuroradiology 27*, 5 (2006), 1040–1045.

[141] Taylor, A. J. Diffusion tensor imaging: Evaluation of tractography algorithm performance using ground truth phantoms. *Diffusion Tensor Imaging: Evaluation of Tractography Algorithm Performance Using Ground Truth Phantoms* (2005). Master Thesis.

[142] Tournier, J.-D., Calamante, F., and Connelly, A. Robust determination of the fibre orientation distribution in diffusion MRI: Non-negativity constrained super-resolved spherical deconvolution. *NeuroImage 35*, 4 (2007), 1459–1472.

[143] Tournier, J.-D., Calamante, F., Gadian, D. G., and Connelly, A. Direct estimation of the fiber orientation density function from diffusion-weighted MRI data using spherical deconvolution. *NeuroImage 23*, 3 (2004), 1176–1185.

[144] Tournier, J. D., Yeh, C.-H., Calamante, F., Cho, K.-H., Connelly, A., and Lin, C.-P. Resolving crossing fibres using constrained spherical deconvolution: Validation using diffusion-weighted imaging phantom data. *NeuroImage 42*, 2 (2008), 617–625.

[145] Trefethen, L. N., and Trummer, M. R. An instability phenomenon in sprectral methods. *SIAM Journal of Numerical Analysis 24*, 5 (1987), 1008–1023.

[146] Tristan-Vega, A., Westin, C.-F., and Aja-Fernandez, S. Estimation of fiber orientation probability density functions in high angular resolution diffusion imaging. *NeuroImage 47*, 2 (2009), 638–650.

[147] Tuch, D. *Diffusion MRI of Complex Tissue Structure* (January 2002). Ph.D. Thesis.

[148] Tuch, D., Weisskoff, R., Belliveau, J. W., and Wedeen, V. J. *In: Proceedings of the ISMRM* (1999), 321.

[149] Tuch, D. S. Q-ball imaging. *Magnetic Resonance in Medicine 52* (2004), 1358–1372.

[150] Tuch, D. S., Reese, T. G., Wiegell, M. R., Makris, N., Belliveau, J. W., and Wedeen, V. J. High angular resolution diffusion imaging reveals intravoxel white matter fiber heterogeneity. *Magn. Res. Med. 48*, 4 (2002), 577–582.

[151] Vaillant, M., and Glaunès, J. Surface matching via currents. In *Proc. Information processing in medical imaging* (January 2005), vol. 19, pp. 381–92.

[152] Vapnik, V., and Chervonenkis, A. On the uniform convergence of relative frequencies of events to their probabilities. *The. of Prob. App. 16* (1971), 264–280.

[153] Verma., V., and Pang, A. Comparative flow visualization. *IEEE Transactions on Visualization and Computer Graphics 10*, 6 (2004), 609–624.

[154] Wassermann, D., Bloy, L., Verma, R., and Deriche, R. Bayesian framework for white matter fibers similarity measure. pp. 815–818.

[155] Wassermann, D., Bloy, L., Verma, R., and Deriche, R. A gaussian process based framework for white matter fiber tracts and bundles, applications to fiber clustering. In *Proceedings Medical Image Computing and Computer Aided Intervention (MICCAI Workshop)* (London, 2009), pp. 200–214.

[156] Wassermann, D., and Deriche, R. Simultaneous manifold learning and clustering: Grouping white matter fiber tracts using a volumetric white matter atlas. In *Proceedings Medical Image Computing and Computer Aided Intervention (MICCAI Workshop)* (New York, 2008).

[157] Wedeen, V. J., Hagmann, P., Tseng, W.-Y. I., Reese, T. G., and Weisskoff, R. M. Mapping complex tissue architecture with diffusion spectrum magnetic resonance imaging. *Magnetic Resonance in Medicine 54*, 6 (2005), 1377–1386.

[158] Weinstein, D., Kindlmann, G., and Lundberg, E. Tensorlines: Advection-diffusion based propagation through diffusion tensor fields. pp. 249–253.

[159] Weldeselassie, Y., Barmpoutis, A., and Atkins, M. S. Symmetric positive-definite cartesian tensor orientation distribution functions (CT-ODF). In *MICCAI* (Beijing, China, 2010), pp. 582–589.

[160] Whitcher, B., Tuch, D. S., and Wang, L. The wild bootstrap to quantify variability in diffusion tensor MRI. In *13th Annual Meeting of ISMRM* (Miami, 2005), p. 1333.

[161] Wittenbrink, C. M., Pang, A., and Lodha, S. Glyphs for visualizing uncertainty in vector fields. *IEEE Transactions on Visualization and Computer Graphics 2*, 3 (1996), 266–279.

[162] Xie, Y., Vemuri, B. C., and Ho, J. Statistical analysis of tensor fields. vol. 6361 of *LNCS*, pp. 682–689.

[163] Zalesky, A. DT-MRI fiber tracking: a shortest paths approach. *IEEE Trans Med Imaging 27* (2008), 1458–1471.

[164] Zhan, L., Leow, A. D., Jahanshad, N., Chiang, M. C., Barysheva, M., Lee, A. D., Toga, A., McMahon, K., de Zubicaray, G., Wright, M., and Thompson, P. M. How does angular resolution affect diffusion imaging measures. *NeuroImage 49* (2010), 1357–1371.

[165] zarslan, E., and Mareci, T. H. Generalized diffusion tensor imaging and analytical relationships between diffusion tensor imaging and high angular resolution diffusion imaging. *Magnetic Resonance in Medicine 50*, 5 (2003), 955–965.

[166] zarslan, E., Shepherd, T. M., Vemuri, B. C., Blackband, S. J., and Mareci, T. H. Resolution of complex tissue microarchitecture using the diffusion orientation transform (dot). *NeuroImage 31*, 3 (2006), 1086–1103.

[167] zarslan, E., Vemuri, B. C., and Mareci, T. H. Generalized scalar measures for diffusion mri using trace, variance, and entropy. *Magnetic Resonance in Medicine 53*, 4 (2005), 866–876.